Development of a fast precision high voltage divider for electron-ion collision spectroscopy at CRYRING@ESR

MASTER THESIS
submitted in partial fulfillment of the requirements
of the degree of
MASTER OF SCIENCE

University of Münster
Faculty of Mathematics and Natural Science
Institute for Nuclear Physics

by
TIMO DIRKES

Münster, December 2020

Declaration

I herewith declare that I have composed the present thesis myself and without use of any other than the cited sources and aids. Sentences or parts of sentences quoted literally are marked as such; other references with regard to the statement and scope are indicated by full details of the publications concerned. The thesis in the same or similar form has not been submitted to any examination body and has not been published. This thesis was not yet, even in part, used in another examination or as a course performance. Furthermore I declare that the submitted written (bound) copies of the present thesis and the version submitted on a data carrier are consistent with each other in contents.

I agree to have my thesis checked in order to rule out potential similarities with other works and to have my thesis stored in a database for this purpose.

Münster, 08.12.2020 

Place, Date Signature

Dean: **Prof. Dr. M. Rohlfing**

First examiner: **Prof. Dr. C. Weinheimer**

Second examiner: **Dr. V. Hannen**

Contents

Chapter 1

Introduction

The urge for a rational understanding regarding the structure and functioning of the material world has preoccupied man since the age of Archaic Greece. Scholars and philosophers of that time, today referred to as pre-Socratic philosophers, refused to accept various supernatural, mythological or religious explanations for the phenomenal world and suggested it could be explained in its entirety by natural causes. This was the beginning of the era of natural philosophy (from Latin *philosophia naturalis*), the precursor of natural science. In the course of this, atomism was born, the idea of a physical world composed of indivisible constituents, the so-called atoms (from Ancient Greek *átomos*; the indivisible). This theory consolidated until modernity and finally had been proven directly by means of Albert Einstein's explanation of the Brownian motion [Ein05] for the first time in 1905 and quantitatively confirmed in the following years by the experiments of Jean Baptiste Perrin. However, scattering experiments by Ernest Rutherford [Rut11] showed that these atomic particles can also be subdivided into constituents, the previously discovered electron [Tho97] and the atomic nucleus which later lost its status as indivisible as well. Throughout the 20th century, driven by the technical achievements in accelerator physics and the developments in quantum physics, scientists all around the globe succeeded in discovering not only the electron, but also further indivisible building blocks of nature. These are nowadays classified as quarks, leptons and bosons in the Standard Model of particle physics. Since its latest important confirmation, accomplished in 2012 by the experimental discovery of the Higgs boson [A+12] with the ATLAS[1] detector at the LHC[2] at CERN[3] in Switzerland, the Standard

[1] A Toroidal LHC ApparatuS

[2] Large Hadron Collider

[3] European Organization for Nuclear Research (from French *Conseil Européen pour la Eecherche Nucléaire*)

Model still holds in describing all known elementary particles as well as three of the four known fundamental forces (the electromagnetic, weak nuclear, and strong nuclear force, and not including the gravitational force) within the framework of quantum field theory.

Despite this enormous progress in the recent past of scientific research, there are still numerous questions concerning the atomic structure with regard to the Standard Model. The hydrogen atom, for example, as the most fundamental atom, suffers from a lacking understanding of its proton charge radius [P+10] when describing the bound electron shell. Regarding more complex systems, in addition to the nuclear size, many other nuclear, relativistic and QED effects have an impact on the electronic structure. A unique way to investigate these fundamental processes and symmetries of bound states are DR[4]-assisted laser spectroscopy experiments of dipole-forbidden transitions in highly charged heavy ions (HCIs). These few-electron systems in strong electromagnetic fields allow to determine transition energies with very high precision due to the strong attenuation of external EM-field disturbances. Hence, e.g. strong-field QED contributions with respect to the QED predicted effect of vacuum polarization and self energy can be examined. Such state-of-the-art spectroscopy research methods on HCIs are performed in storage ring facilities where ion beams are produced by energetic collisions or high-energy photon absorption in heavy ion particle accelerators or electron beam ion traps. A future worldwide leading facility for HCI research will be the international particle accelerator complex FAIR[5] (former GSI[6] Helmholtz Centre for Heavy Ion Research) in Darmstadt which is currently under construction.

One of the first commissioned components of FAIR is the low-energy heavy ion storage ring CRYRING@ESR, complementing the pre-existing GSI storage ring ESR[7] in operation with its adjacent energy regime. It allows electron-ion collision spectroscopy experiments with high luminosity by use of its high-performance electron cooler achieving a low-momentum spread of the stored ion beam. The electron cooler superimposes the ion beam with a quasi-monoenergetic cold electron beam forcing momentum transfer by Coulomb interactions until thermodynamic equilibrium is reached. The ion velocity is then determined by the acceleration voltage of the electron cooler by which the electrons are emitted. Thus, a precise knowledge of the acceleration voltage is essential for high-resolution spectroscopy with a relative uncertainty in the 10 ppm[8] range [A+15]. Since commercially available high voltage dividers do not offer the required precision and stability, an ultra-stable precision 35 kV HV divider, referred to as G35, was constructed at the Institute for Nuclear Physics of the University of Münster [Win20]. Similar devices are the 35 kV [TTW09] and 65 kV [B+13] HV dividers, constructed in cooperation with the PTB[9], for usage at the KATRIN[10] experiment. The G35 HV divider features an ultra-stable resistance divider chain optimized for high-precision measurements of static

[4] Dielectronic Recombination
[5] Facility for Antiproton and Ion Research
[6] Gesellschaft für SchwerIonenforschung
[7] Experimental Storage Ring
[8] parts per million, 10^{-6}
[9] Physikalisch-Technische Bundesanstalt
[10] KArlsruhe TRItium Neutrino

electron cooler acceleration voltages. In DR-assisted laser spectroscopy experiments, the electron cooler also acts as an electron target apart from its cooling purpose. Thereby, collision energy scanning is conducted where variable electron energies relative to the ion beam are introduced. This is realized via ramping the acceleration voltage to a variable offset potential for short time intervals of a few milliseconds. Hence, the divided voltage, provided by the G35, has to settle in an appropriate timing window to allow accurate measurements of the applied HV. As further investigations had been conducted, it turned out that it is not possible to measure the acceleration voltage within short time slices with the desired accuracy due to emerging voltage load characteristics of the divider setup [Rot19].

Therefore, within this work, an additional HV divider was designed and commissioned, complementing the pre-existing divider setup. With its all-pass characteristics, realized by frequency compensation, it offers fast voltage division that enables precise measurements of short-lasting electron cooler potentials. **Chapter 2** provides a detailed description of the technique of DR spectroscopy and highlights the limitations of the existing HV measurement setup including the G35 HV divider with regard to those measurements. Consequently, theoretical aspects of voltage divider compensation, exploited to minimize frequency-dependence, are outlined in **Chapter 3**. The electrical and mechanical design are described together with simulating the transmission behaviour of the novel divider setup in **Chapter 4**. In **Chapter 5**, the final construction, based on the aforementioned design, is described along with the divider calibration results regarding its transient response behaviour and long-term stability. **Chapter 6** gives a summary and outlook on upcoming activities.

Chapter 2

Electron-ion collision spectroscopy at CRYRING@ESR

A broad range of physics topics including atomic, nuclear and plasma physics motivate experiments which take advantage of induced reactions of multiply charged ions with electrons. Depending on the impact energy, different types of reactions can be stimulated. These comprise non-resonant radiative processes and resonant dielectronic processes mediated by electron capture or impact ionization. Those processes reveal deep insights into the atomic structure of the ions and can enable tests of QED, relativistic or nuclear effects. Especially the cross section of the resonant process of dielectronic recombination (DR) features pronounced energy-sharp resonant structures that can be examined in assistance to high-resolution laser spectroscopy. Since DR is a primary spectroscopy tool applied at cooler storage rings like CRYRING@ESR, the fundamentals discussed in this section concentrate on this special atomic process. Cooler storage rings can store molecular or atomic ion beams prepared in external sources for several seconds up to minutes. To reduce the spatial and velocity spread of the stored ions, phase-space cooling is applied. There are various cooling technologies that can be implemented in a storage ring setup, i.e. stochastic cooling for relativistic energies or electron cooling applicable for all energy ranges where the ion beam can be merged with an equal velocity electron beam. Electron cooling is the method of choice for energy-dependent collision spectroscopy implemented at CRYRING@ESR and will be discussed in detail in the following.

2.1. Overview

CRYRING@ESR is a cooler storage ring formerly stationed at MSL[1] at the University of Stockholm. In 2009, after almost 20 years of use in Sweden with numerous achievements in atomic and molecular physics research, it was relocated to the GSI Helmholtz Centre for Heavy Ion Research as part of the Swedish in-kind contribution to FAIR. Now, CRYRING@ESR is the first new storage ring installation of the particle accelerator complex that has been commissioned in September 2017. It is designed for experiments with low-energy ($300\,\mathrm{keV/u} \lesssim E/m \lesssim 15\,\mathrm{MeV/u}$) exotic ion beams. The ions are produced in the upstream accelerator chain of the existing GSI installations, injected from the storage ring ESR, for the collaborations SPARC[2], FLAIR[3] and NuSTAR[4]. Apart from this, it also serves as beam delivery system for further experiments at HITRAP[5] and USR[6] as well as for prototyping new FAIR slow control technologies.

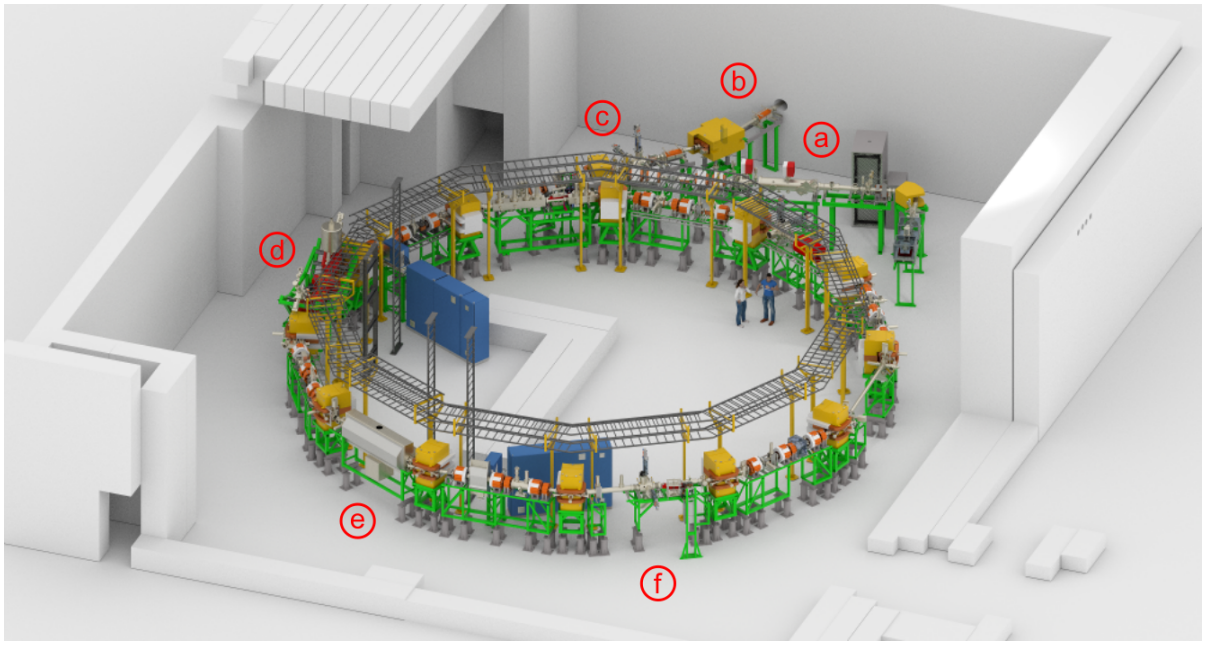

Figure 2.1.: 3D model of the CRYRING@ESR cooler storage ring configuration with local injector (a), transfer beamline from ESR (b), injection septum (c), electron cooler (d), RF cavity (e) and extraction septum (f) [Gei20].

Figure 2.1 displays the current setup of CRYRING@ESR. The storage ring has a circumference of about 54 m and $< 10^{-11}$ mbar vacuum pressure. The ion beam guidance is achieved by means of twelve 30° magnetic dipoles and further magnetic quadrupoles and sextupoles in six of the twelve orbital sections between the magnetic dipoles. The

[1] Manne Siegbahn Laboratory
[2] Support Program for Advancing Research and Collaboration
[3] Facility for Low-energy Antiproton and Ion Research
[4] Nuclear STructure, Astrophysics and Reactions
[5] Heavy Ion TRAP
[6] Ultra-low energy Storage Ring

remaining sections contain components for beam injection and extraction, a radio frequency (RF) cavity for beam acceleration and deceleration as well as a high-performance electron cooler. The latter is mainly used for phase-space cooling of the ion beam and moreover to serve as a cold free-electron target in electron-ion collision spectroscopy experiments. Five more sections are intended for experimental installations of atomic and nuclear physics experiments. Furthermore, CRYRING@ESR features a local injector consisting of a local ion source and a 300 keV/u radio frequency quadrupole (RFQ) linear accelerator which allows an operation independent of the other GSI/FAIR accelerator facilities.

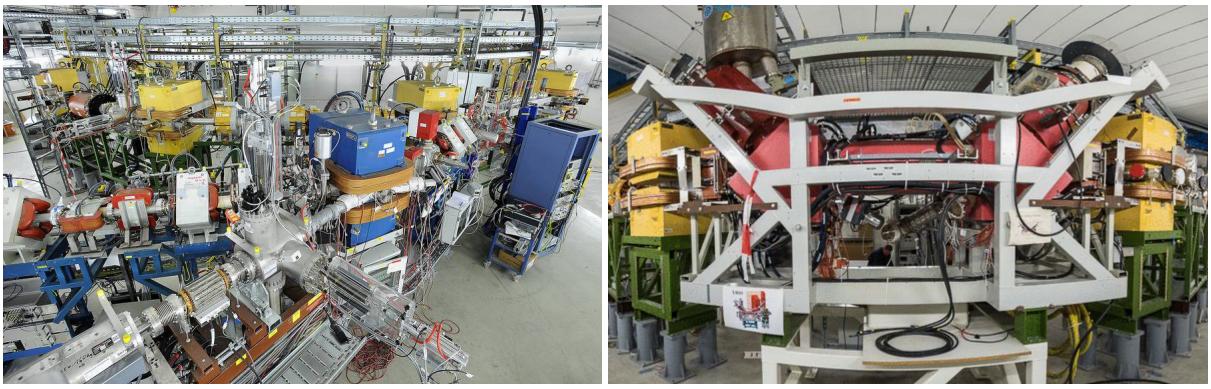

(a) Side view from injection septum [Ott16] **(b)** Electron cooler [Mer20]

Figure 2.2.: CRYRING@ESR cooler storage ring installation at GSI/FAIR with its injection septum (a) for local and ESR transfer injection and the dedicated high-performance electron cooler (b) surrounded by two magnetic dipoles.

2.2. Electron cooling

Ion beams injected into a storage ring initially suffer from high emittance, i.e. a broad distribution of particle coordinates in position-and-momentum phase-space, due to thermal motion. This results in decreasing likelihoods of particle interactions in collision experiments and thus lower luminosity. To shrink the emittance without removing ions from the beam, it is necessary to compress the occupied phase-space (equivalent to reducing the temperature) of the stored ions. A method of doing so, which is also applied at CRYRING@ESR, is electron cooling using the installed high-performance electron cooler. It superimposes the ion beam with a quasi-monoenergetic cold beam of electrons having the same velocity as the ions. Consequently, the ions undergo Rutherford scattering by Coulomb interactions with the electrons causing momentum (thermal energy) exchange until thermodynamic equilibrium is reached. This requires electrons having much lower kinetic energies than the ions. Another use case for the electron cooler is serving as an electron target in high resolution electron-ion collision spectroscopy experiments where the resonant process of dielectronic recombination is utilized (DR collision spectroscopy, see Section 2.3 and 2.4).

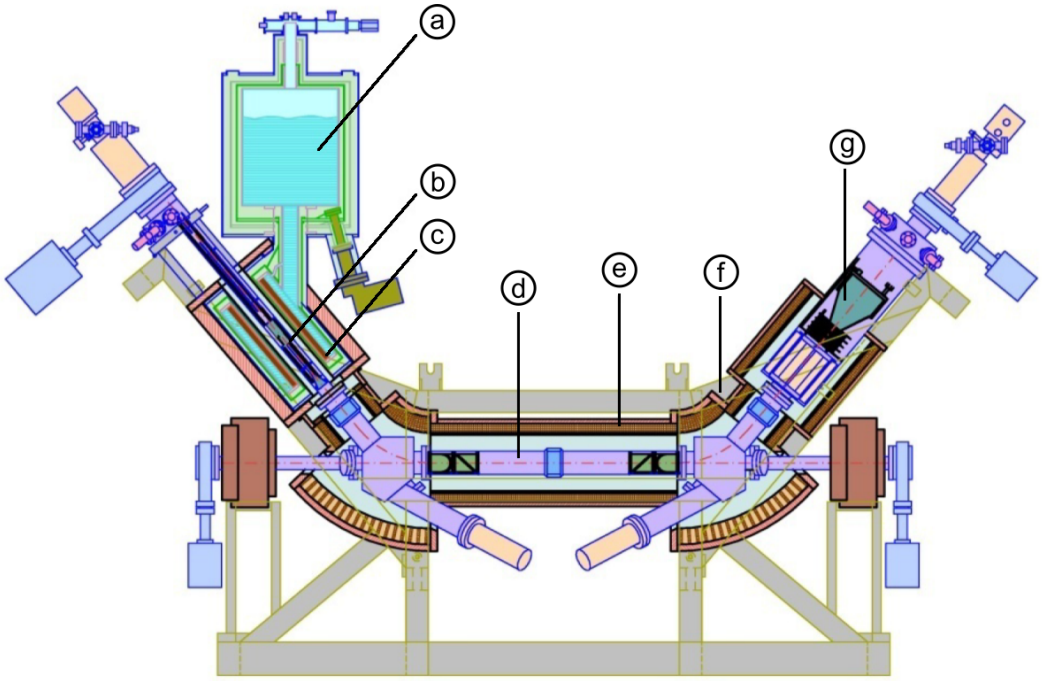

Figure 2.3.: Schematic cross-section of the CRYRING@ESR electron cooler with liquid-helium reservoir (a), electron gun (b), superconducting gun solenoid (c), drift tube (d), normal-conducting magnet winding (e), toroid magnet (f) and electron collector (g) [A+15].

The electron cooler setup at CRYRING@ESR is illustrated in Figure 2.3. Electrons are produced at a BaO-plated tungsten cathode, the so-called electron gun, of 900 °C ($k_B T_{Cath} \approx 100\,\text{meV}$) temperature and about 4 mm diameter via thermionic emission. The electrons are then accelerated by an electrostatic field to the Faraday cup (i.e. electron collector) functioning as an anode with an electron current of up to 150 mA during operation. The e^--gun is enclosed by a superconducting solenoid coil leading to a vacuum chamber in which the ions are guided. The electron beam is bent in and along the ion beam by surrounding normal-conducting toroid magnets. Additionally, a solenoid magnetic field guides the particles through the grounded drift tubes acting as interaction section. Furthermore, the guiding magnetic field suppresses the blow-up of the electron beam due to the repulsive Coulomb force which creates a space charge potential. The electron beam is decoupled in its longitudinal and transverse degree of freedom, so that the energy distribution of the electrons can be approximated by means of an anisotropic flattened double Maxwellian distribution [D+94]:

$$f(v_r, \vec{v}) = \sqrt{\frac{m_e}{2\pi k_B T_\parallel}} \exp\left(-\frac{m_e (v_\parallel - v_0)^2}{2 k_B T_\parallel}\right) \times \frac{m_e}{2\pi k_B T_\perp} \exp\left(-\frac{m_e v_\perp^2}{2 k_B T_\perp}\right). \tag{2.1}$$

It depends on the average velocity v_r between the electrons and the ions. $k_B T_\perp$ and $k_B T_\parallel$ are the transverse respectively longitudinal thermal energy spreads of the electron beam with transverse velocity $v_\perp$ and longitudinal velocity $v_\parallel$. The transverse degree of freedom surpasses the longitudinal by a few orders of magnitude as a result of adiabatic acceleration, so that it holds $k_B T_\parallel \ll k_B T_\perp$.

The energy spread $\Delta E_r(\mathrm{FWHM})$ can be described by [Mü08]

$$\Delta E_r(\mathrm{FWHM}) = \sqrt{[\ln(2) k_B T_\perp]^2 + 16 \ln(2) k_B T_\parallel E_r}. \tag{2.2}$$

Regarding cooling optimization, the transverse energy spread of the emitted electrons from the cathode material is reduced by adiabatic transverse expansion between the gun and the drift tube as illustrated in Figure 2.4.

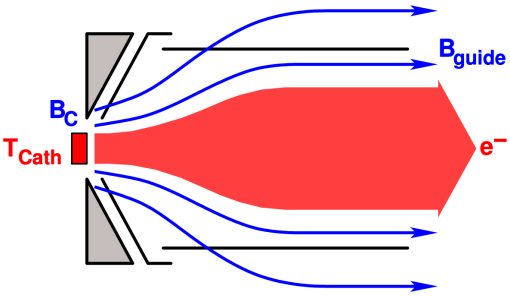

Figure 2.4: A magnetized electron beam passing from a region with a high magnetic field B_C into a low-field region B_{guide} experiences transverse expansion [Les07].

Thereby, the electron beam passes through a region of decreasing axial magnetic field with expansion ratio

$$\xi = \frac{B_C}{B_{guide}}. \tag{2.3}$$

It changes adiabatically with respect to the electron cyclotron motion, so that the ratio of the longitudinal magnetic field strength and the transverse energy of the electrons is invariant. The transverse degree of freedom then equals the cathode emission energy multiplied by the inverse expansion ratio:

$$k_B T_\perp = \xi^{-1} k_B T_{Cath}. \tag{2.4}$$

This allows a temperature reduction of a factor up to $\xi^{-1} = 100$ (3 T to 0.03 T) [Dan93]. Hence, typical values for the electron beam thermal energies are $k_B T_\perp = 1.0 - 1.5\,\mathrm{meV}$ and $k_B T_\parallel = 0.05 - 0.2\,\mathrm{meV}$ [A+15]. More concepts for electron temperature optimization of both transverse and longitudinal direction are referenced in [D+11].

2.3. Dielectronic recombination (DR)

A scattering process involving an electron projectile and an ion target, where the ion remains in its original state, can be described as elastic scattering:

$$e^- + X^{q+} \rightarrow X^{q+} + e^-. \tag{2.5}$$

As in electron cooler storage rings employed, the ion beam only gains or loses kinetic energy from the deflected electron passing its Coulomb field (see Figure 2.5a). An alternative scattering process is dielectronic recombination (usually abbreviated by DR), explained in the following.

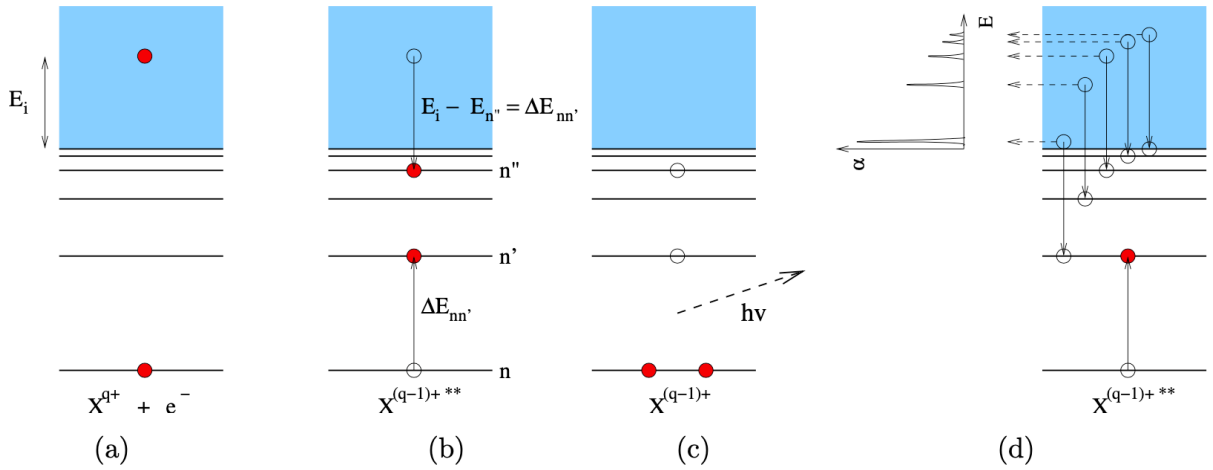

Figure 2.5.: Principle of the dielectronic recombination process from its initial state (a) to dielectronic capture (b) and further relaxation by photon emission (c) forming a Rydberg series of resonances (d) [Les07].

At first, the initially free electron is captured into a subshell of the ion, while exciting a core electron by the transferred energy into a higher level, forming a doubly excited intermediate ion state $X^{(q-1)+**}$ (see Figure 2.5b). This so-called dielectronic capture is a resonant process. It can only occur if the energy gained from the capture of the free electron matches the excitation energy of the core electron $E_i - E_{n'} = \Delta E_{nn'} = E_n - E_{n'}$ with E_i being the initial kinetic energy of the free electron and E_n, $E_{n'}$ and $E_{n''}$ being the level energies of the involved electronic states. In other words, this process can be seen as time-reversed autoionization, or rather time-reversed Auger effect. Secondly, this doubly excited intermediate ion relaxes with a certain probability by photon emission (see Figure 2.5c):

$$e^- + X^{q+} \rightarrow X^{(q-1)+**} \rightarrow X^{(q-1)+} + h\nu. \tag{2.6}$$

Depending on the collision energy, the process may populate various states of the ion forming a Rydberg series of resonances (see Figure 2.5d). Its averaged energy-dependent cross-section can be determined by multiplying the cross-section for dielectronic capture [Mü08]

$$\sigma_d^{\mathrm{DC}} = 7.88 \times 10^{-31}\,\mathrm{cm^2 eV^2 s} \frac{1}{E_e} \frac{g_d}{2g_i} \frac{A_a(d \rightarrow i) \cdot \Gamma_d}{(E_e - E(|d\rangle) + E(|i\rangle))^2 + \Gamma_d^2/4}, \tag{2.7}$$

where E_e is the electron energy, $E(|i\rangle)$ and $E(|d\rangle)$ are the energy levels and g_i and g_d the statistical weights of the initial state $|i\rangle$ and the doubly excited state $|d\rangle$, with the fluorescence yield

$$\omega_r = \hbar \frac{\sum_f A_r(d \rightarrow f)}{\Gamma_d} \tag{2.8}$$

of $|d\rangle$ with its full width

$$\Gamma_d = \hbar \left[\sum_{k'} A_a(d \rightarrow k') + \sum_{f'} A_r(d \rightarrow f') \right]. \tag{2.9}$$

A_a and A_r denote the rate for autoionization respectively radiative transition from one initial state to another final state. ω_r sums up all radiative transition rates below the first ionization limit of the $X^{(q-1)+}$ ion state. Γ_d sums up all autoionization and radiative transition rates reachable from $|d\rangle$. Bringing together Equation 2.7 and Equation 2.8 one gets the dielectronic recombination cross-section

$$\sigma_d^{\mathrm{DR}} = A_{\mathrm{DR}} \frac{\Gamma_d}{2\pi} \frac{1}{(E_e - E(|d\rangle) + E(|i\rangle))^2 + \Gamma_d^2/4} \tag{2.10}$$

with

$$A_{\mathrm{DR}} = 4.95 \times 10^{-30}\,\mathrm{cm^2 eV^2 s} \frac{1}{E_e} \frac{g_d}{2g_i} \frac{A_a(d \to i) \sum_f A_r(d \to f)}{\sum_{k'} A_a(d \to k') + \sum_{f'} A_r(d \to f')} \tag{2.11}$$

being the dielectronic recombination rate. The resonant process of DR competes with another non-resonant process of radiative recombination (RR):

$$e^- + X^{q+} \to X^{(q-1)+} + h\nu \tag{2.12}$$

where the incident electron is captured into a bound subshell of the ion and the excess energy is carried away by photon emission leading into very high Rydberg states. The RR process is of interest especially for DR spectroscopy since it causes a continuous background alongside the DR peaks in the resonance spectrum.

2.4. Experimental framework

In DR collision spectroscopy at CRYRING@ESR, the electron cooler, shown in Section 2.2, is utilized as a target of free electrons. The technique can be treated as Auger spectroscopy, where an emitted electron yields the relevant structure information, in inverse kinematics. I.e. the absorbed electron forming a doubly excited intermediate ion state, is measured. An experimental background is given by radiative electron capture processes from ions of residual gas molecules. By co-propagating electron beam and ion beam at sharply higher energy as the bound target electrons of the gas molecules in a merged-beam collision configuration, the cross-section of the electron capture process can be reduced along with ultrahigh vacuum conditions. Apart from this, the technique of merged-beams features special kinematics, as outlined in Subsection 2.4.2, achieving high sensitivity at small relative energies.

Former experiments at cooler storage rings established the spectroscopy technique. These include measurements of isotope shifts with Pb^{53+} ions at CRYRING[7] [S+05] at its previous location at MSL in Stockholm, Nd^{57+} ions at the ESR [B+08] at GSI in Darmstadt or hyperfine-split dielectronic resonances in lithium-like Sc^{18+} ions at the TSR[8] [L+08] at the Max Planck Institute for Nuclear Physics in Heidelberg.

[7] The term CRYRING instead of CRYRING@ESR is used for its former configuration located at MSL in Stockholm.

[8] Test Storage Ring

2.4.1. Determining the recombination rate coefficient

In electron-ion merged-beam setups, the resonant DR spectrum is measured as merged-beams recombination rate coefficient (MBRRC) [A+15]

$$\alpha(v_r) = v_r \int \sigma_d^{\mathrm{DR}} \cdot f(v_r, \vec{v}) d\vec{v} = v_r \langle \sigma_d^{\mathrm{DR}} \rangle. \tag{2.13}$$

It convolutes $v_r \cdot \sigma_d^{\mathrm{DR}}$ (see Equation 2.10) with the anisotropic flattened double Maxwellian distribution $f(v_r, \vec{v})$ from Equation 2.1 where v_r denotes the relative velocity between ions and electrons in the center-of-mass (CM) frame. $\vec{v}$ represents the electron beam velocity with its transverse and longitudinal component $v_\perp$ and $v_\parallel$. On an absolute scale, expressed in terms of specific measured values of the CRYRING@ESR setup, the MBRRC can be readily derived from [BK12]

$$\alpha(v_r) = R \frac{e q_{\mathrm{Ion}} c \beta_{\mathrm{Ion}}}{(1 - \beta_{\mathrm{Ion}} \beta_e) I_{\mathrm{Ion}} n_e L \eta}. \tag{2.14}$$

R denotes the detection count rate of recombined ions $X^{(q-1)+}$, η the detection efficiency, I_{Ion} the ion current and n_e the electron density of the beam produced by the electron gun. L is the overlap length of electron and ion beam. $\beta_{\mathrm{Ion},e} = (1 - 1/\gamma^2_{\mathrm{Ion},e})^{1/2}$ represents the ion respectively electron beam velocity given in units of the speed-of-light c. The initial ion charge state is given by q_{Ion} and the electron charge by e.

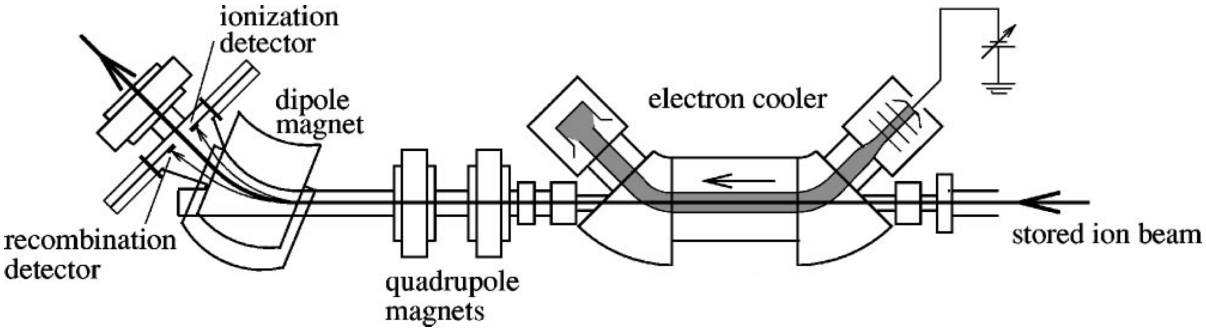

Figure 2.6.: Simplified sketch of the experimental arrangement for electron-ion merged-beam collision measurements such as DR and electron impact ionization (EII) at heavy-ion storage ring configurations like CRYRING@ESR [T+02].

After passing the drift tube of the electron cooler, ions may differ in their charge state in comparison to the initial ion beam due to charge-exchanging scattering processes with the electron beam. These ions are then deflected by the downstream dipole magnet with magnetic field strength B behind the electron cooler into altered trajectories of different ion species (see Figure 2.6) with orbital radii

$$r_k = \frac{m_k v_{\mathrm{Ion}}}{q_k B} \tag{2.15}$$

where q_k denotes the ion charge, m_k the ion mass and v_{Ion} ion beam velocity. This allows a separate detection of the final states with altering charge q_p and mass m_p from

the initial charge state (q_i, m_i) via single-particle detectors located behind the dipole section. Proceeding from Equation 2.15, the orbital radius r_p of an altered ion state, and thus the position of the corresponding detector segment, can be calculated from the product of the inverted charge-to-mass ratio

$$\kappa = \frac{(q_p/m_p)}{(q_i/m_i)} \tag{2.16}$$

and the initial orbital radius r_i of the parent ion beam:

$$r_p = \kappa^{-1} r_i. \tag{2.17}$$

For detecting ions in low-charge states ($q_p < 20$) a non-hygroscopic scintillation detector is implemented (see Figure 2.7) at CRYRING@ESR. It consists of a YAP:Ce[9] scintillator crystal together with a wave guide forming the detector head. A Hamamatsu R8619 photomultiplier tube (PMT) records the emitted photons produced by the incident ion. It is usable in UHV conditions and further features a high photon yield of 10.000 photons per MeV deposited energy emitted at $330 - 380\,\text{nm}$ wavelength and a fast decay time of 25 ns compared to YAG:Ce[10] (70 ns) and NaI:Tl[11] (230 ns). Through mounting on a 700 mm travel length translation stage, the detector provides access to various beam trajectories. For the detection of ion species in higher charge states ($q_p > 20$), another detector, based on a channel electron multiplier (CEM), is used.

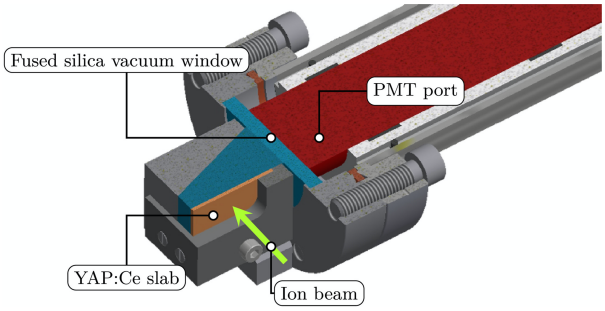

Figure 2.7: CAD model of the scintillation detector design with YAP:Ce slab target for incoming ions, PMT attached to a UV-transparent vacuum window and the wave guide [H+19].

The DR collision spectroscopy measurement is performed by detuning the potential difference between the electron gun and the drift tube (i.e. interaction region) for short-time intervals (e.g. 10 ms) by varying amounts. Thus, various relative electron-ion collision energies can be realized. Simultaneously, the rate $\alpha(v_r)$ of recombined ions (see Equation 2.14) at certain trajectories can be detected. As an example, the low-energy DR resonance spectrum of F^{6+} ions measured at the TSR electron cooler in Heidelberg is depicted in Figure 2.8. The term *Classical measurement scheme* indicates the scanning method of varying the electron gun potential in conjunction with grounded drift tubes[12]. A deeper physical view of the scanning process via varying the collision energy through cooler potential alternation is covered in the subsequent Subsection 2.4.2.

[9] Cerium doped yttrium aluminium perovskite
[10] Cerium doped yttrium aluminium garnet
[11] Thallium doped sodium iodide
[12] An alternative method would be the variation of the drift tube potential while emitting electrons with static energy from the electron gun.

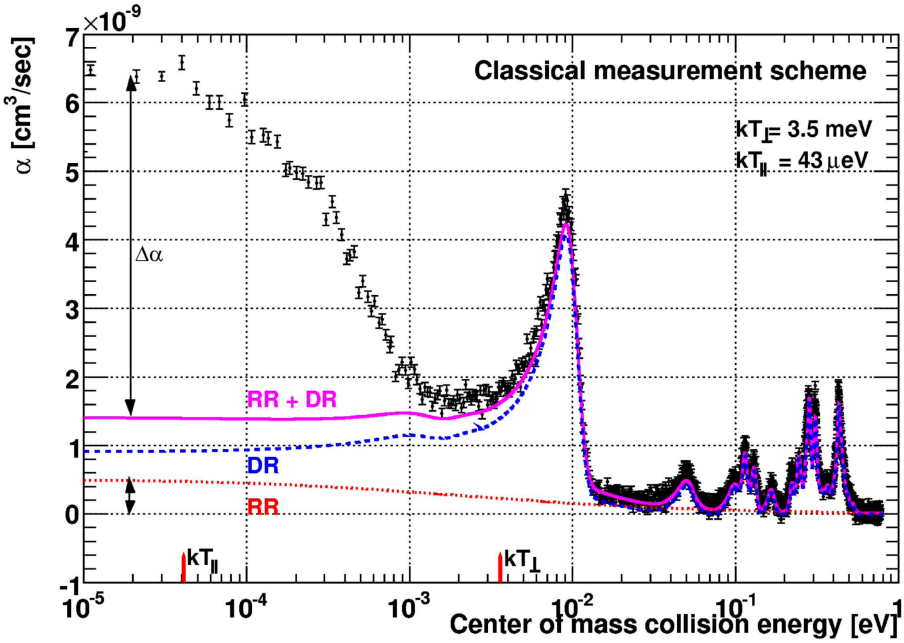

Figure 2.8.: Low-energy DR resonance spectrum of $e^- + F^{6+}$ as measured with the TSR electron cooler in Heidelberg. It shows the influence of non-resonant RR channels on the DR resonance spectrum. $\Delta\alpha = 5.1 \times 10^{-9}\,\mathrm{cm}^3/\mathrm{s}$ denotes the observed excess rate by electron capture at small relative energy. The variation of collision energy in CM-frame was performed via electron gun potential alternation [Les07].

2.4.2. Collision energy scanning

To successively measure the MBRRC at various collision energies, the electron cooler potential U_{cool} needs to be precisely detuned to ascending measurement potentials U_{meas} (see Figure 2.9a). Therefore, an isolated fast HV amplifier will be used to introduce detuning offsets up to $U_{det} = \pm 2\,\mathrm{kV}$ for short-time intervals between which a cooling voltage U_{cool} is applied. This procedure of intermediate cooling maintains the cooling force acting on the ion beam. Thus, the beam quality is preserved while generating periodically relative velocities between the ions and the merged electrons. A collision energy scan consists of a sequence of several hundreds to thousands of measurement steps. Each step is characterized by its individual detuning potential followed by a cooling step both lasting about 10 ms. The electron kinetic energy in the laboratory frame equals

$$E_{lab} = e(U_{meas} + U_{sc}) = e(U_{cool} + U_{det} + U_{sc}) \tag{2.18}$$

with U_{sc} being the space charge potential of the electron beam. Hence, the relativistic Lorentz factor γ_e of the electrons with rest mass m_e can be calculated under consideration of Equation 2.18 as

$$\gamma_e = 1 + \frac{E_{lab}}{m_e c^2} = 1 + \frac{e(U_{cool} + U_{det} + U_{sc})}{m_e c^2}. \tag{2.19}$$

If no detuning voltage is applied ($U_{det} = 0$), the relativistic γ_e-factor equals the relativistic Lorentz factor γ_{Ion} of the ions due to the cooling process. By applying a measurement potential U_{meas} with $U_{det} \neq 0$ for a short period of time in the order of milliseconds, γ_e is varied while γ_{Ion} stays constant. This leads to a relative energy difference E_r between electrons and ions. Knowing γ_e and γ_{Ion}, this relative energy can be determined by [Mü08]

$$E_r = m_{\mathrm{Ion}}c^2(1 + m_e/m_{\mathrm{Ion}}) \left[\sqrt{1 + \frac{2m_e/m_{\mathrm{Ion}}}{(1 + m_e/m_{\mathrm{Ion}})^2}(G - 1)} - 1 \right] \tag{2.20}$$

in the center-of-mass (CM) frame with

$$G = \gamma_{\mathrm{Ion}}\gamma_e - \sqrt{(\gamma_{\mathrm{Ion}}^2 - 1)(\gamma_e^2 - 1)}\cos\theta. \tag{2.21}$$

θ denotes the laboratory angle between electron and ion beams. Subtracting the rest energies $m_{\mathrm{Ion},e}c^2$ from the relative energy E_r leads to the relative electron-ion collision energy

$$E_{col} = E_r - m_{\mathrm{Ion}}c^2 - m_e c^2 \tag{2.22}$$

in the CM-frame. It depends on the relativistic Lorentz factors γ_e (see Equation 2.19) and $\gamma_{\mathrm{Ion}} = \gamma_e(U_{det} = 0)$. Consequently, E_{col} also depends on the detuning potential U_{det} and the cooling potential U_{cool}. The relation between E_{col} and the detuning voltage U_{det} in merged-beam kinematics follows an asymmetric parabola as shown in Figure 2.9b. This allows high experimental sensitivity in collision energy scanning especially for high ion energies. Maximizing the ion energy increases the beam lifetimes in the cooler storage ring together with the reduction of the excess rate $\Delta\alpha$ by electron capture from residual gas molecules.

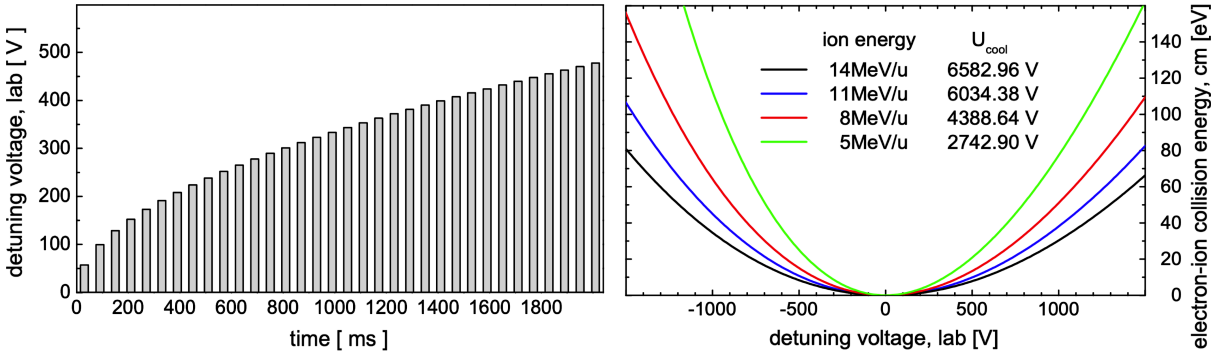

(a) Energy scanning with intermediate cooling **(b)** Visualization of merged-beam kinematics

Figure 2.9.: Fundamentals of collision energy scanning. The detuning energy steps are equidistant in the CM-frame and last about 10 ms as well as the interlaced cooling steps (a). High experimental sensitivity through varying the detuning potential U_{det} is reachable at low relative collision energies in the CM-frame and is improvable through increasing the ion energy (b) [A+15].

2.5. Preliminary HV measurement setup

The importance of precisely measuring the cooler voltage became especially clear during a storage ring beam time at ESR in 2011 performing the LIBELLE[13] experiment [L+14] where the observation of the ground-state hyperfine transition in a laser spectroscopy measurement with lithium-like bismuth was observed for the first time. However, it suffered from the limitation of accuracy of the transition energy in the ion's rest frame due to insufficient knowledge of their velocity. In a second LIBELLE beam time in 2014, the cooler voltage was measured using a dedicated precision voltage divider from PTB[14] Braunschweig. This improved the accuracy to the 10 ppm range and prompted the development of the G35 HV divider. It was constructed at the Institute for Nuclear Physics of the University of Münster similar to the KATRIN precision HV dividers K35 and K65 with a voltage operation range up to 35 kV. Under control of further systematic uncertainties, e.g. space charge effects, it allows an experimental accuracy in the low-ppm range for DC voltages using an 8.5-digits Keysight 3458A DMM [Key20a]. Hence, the device is suitable for a considerable part of the intended experiments at ESR and CRYRING@ESR. Moreover, a novel absolute calibration method has been developed enabling the standalone calibration of the divider setup. It allows the utilization of commercial measurement equipment instead of regular calibration at metrology institutes [Res19].

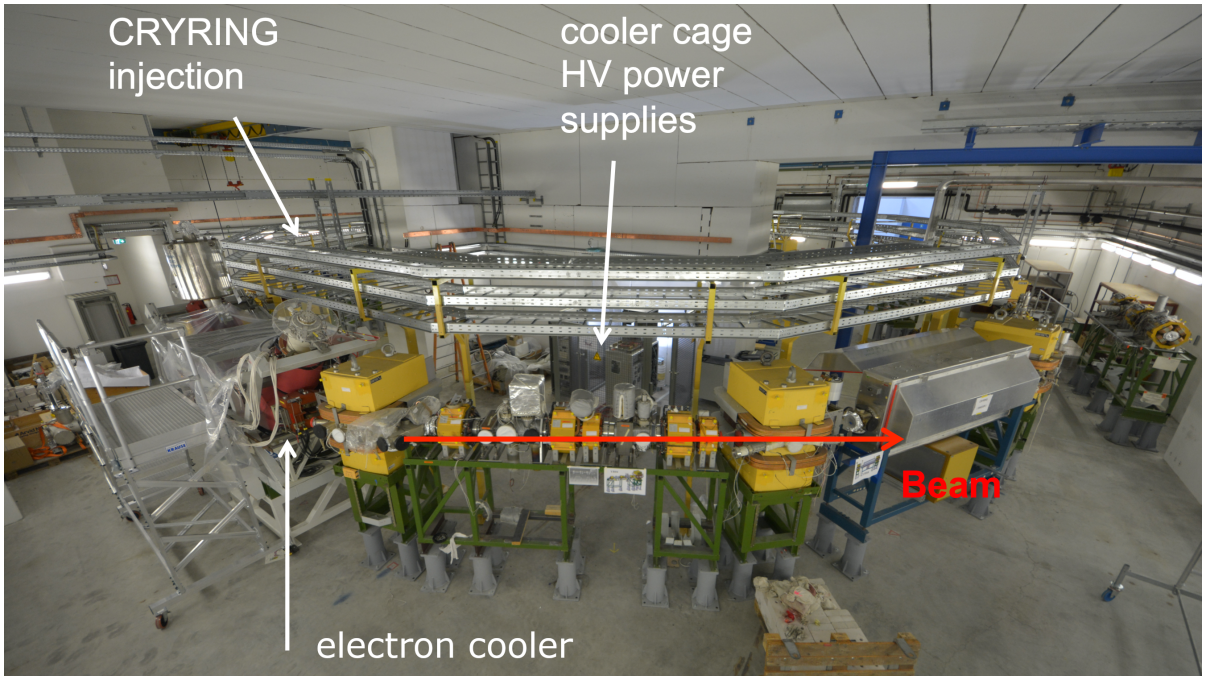

Figure 2.10.: Side view of the CRYRING@ESR from the detection section corresponding to collision experiments at the electron cooler. The HV power supplies together with the HV measurement setup is shielded inside a high potential cage within the storage ring configuration [Roß15].

[13] LIthium like Bismuth Experiment with Laser Light at the ESR
[14] Physikalisch-Technische Bundesantstalt

2.5.1. Divider concept

Since direct ppm-precise HV measurements are unfeasible, the method of indirect measurement utilizing HV dividers is applied. Thereby, the high voltage is scaled down into the range of typically 10 V and subsequently measured by a calibrated high-precision digital voltmeter. In general, the DVM calibration is performed with a 10 V standard reference source (e.g. Fluke 732A [Flu20a]) traceable to a natural standard at metrology institutes like PTB or NIST[15].

A voltage divider is an electrical circuit consisting of multiple resistors and or reactances which cause an input voltage U_{in} to drop in a certain relation over two impedances $\underline{Z}_{\mathrm{HV}} = R_{\mathrm{HV}} + X_{\mathrm{HV}}$ and $\underline{Z}_{\mathrm{LV}} = R_{\mathrm{LV}} + X_{\mathrm{LV}}$ as illustrated in Figure 2.11.

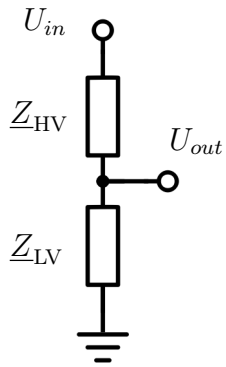

Figure 2.11: Electrical circuit of a simple voltage divider as serial connection of (ohmic) resistors $R_{\mathrm{HV,LV}} = \mathrm{Re}\{\underline{Z}_{\mathrm{HV,LV}}\}$ and or reactances $X_{\mathrm{HV,LV}} = \mathrm{Im}\{\underline{Z}_{\mathrm{HV,LV}}\}$ realized by capacitors or inductors. A voltage drop $U_{out} = U_{in}/M$ occurs at the tap over $\underline{Z}_{\mathrm{LV}}$ according to Equation 2.23 in dependence of the so-called scale factor M [Dir17].

The output voltage U_{out} over $\underline{Z}_{\mathrm{LV}}$ is proportional to the input voltage U_{in}. The relation is defined by the characteristic scale factor M of the divider circuit as

$$M := \frac{U_{in}}{U_{out}} = \frac{\underline{Z}_{\mathrm{HV}} + \underline{Z}_{\mathrm{LV}}}{\underline{Z}_{\mathrm{LV}}} = \frac{\underline{Z}_{\mathrm{HV}}}{\underline{Z}_{\mathrm{LV}}} + 1. \tag{2.23}$$

If $\mathrm{Im}\{\underline{Z}_{\mathrm{HV,LV}}\} \neq 0$, the scale factor is frequency-dependent:

$$M = M(s) \tag{2.24}$$

with $s = i\omega$ being the complex frequency. Usually, voltage dividers are either designed as purely ohmic (see Figure 2.12a) or purely (damped) capacitive (see Figure 2.12b). So, the areas of application are restricted to either DC or AC/step voltages. However, it is also possible to implement ohmic-capacitive dividers (see Figure 2.12c) consisting of one port devices of parallel resistor and capacitor connections serving both DC and AC/step division. This divider type has certain properties in circuit electronics. It allows a frequency independent scale factor M despite $\mathrm{Im}\{\underline{Z}_{\mathrm{HV,LV}}\} \neq 0$ which is relevant for the further course of this work (see Chapter 3). Especially on high voltage side (HV), the circuitry of the divider impedances $\underline{Z}_{\mathrm{HV,LV}}$ is often implemented via a serial connection of several impedances $\underline{Z}_i$. This aims at relieving the impedance components with regard to their dielectric strength. On low voltage side (LV), the realization of multiple components in series constituting $\underline{Z}_{\mathrm{LV}}$ enables numerous scale factors M_k according to Equation 2.23.

[15] National Institute of Standards and Technology

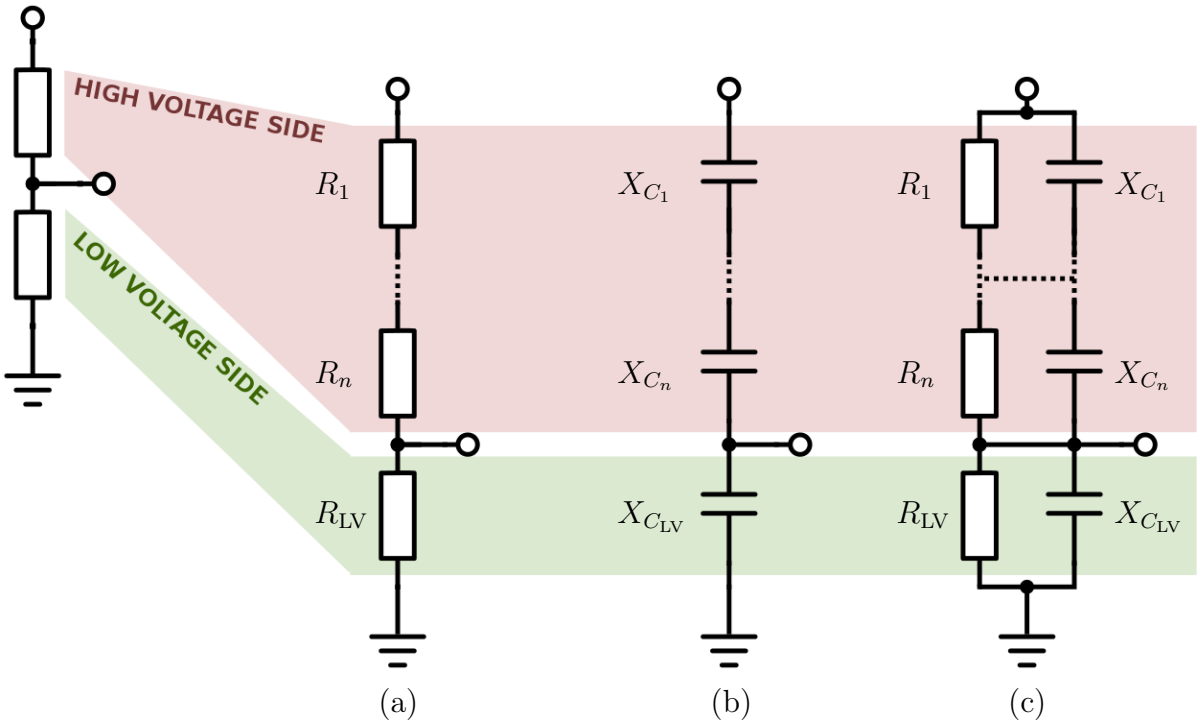

Figure 2.12.: Circuit diagrams of the following voltage divider types: Purely ohmic divider (a), purely capacitive divider (b) and ohmic-capacitive divider (c). Resistance $R_{\mathrm{HV}} = \Sigma_{i=1}^{n} R_i$ of the ohmic divider, reactance $X_{C_{\mathrm{HV}}} = \Sigma_{i=1}^{n} X_{C_i} = \Sigma_{i=1}^{n} s^{-1} C_i^{-1}$ of the capacitive divider as well as impedance $\underline{Z}_{\mathrm{HV}} = \Sigma_{i=1}^{n} \underline{Z}_i = \Sigma_{i=1}^{n} R_i X_{C_i} / (R_i + X_{C_i}) = \Sigma_{i=1}^{n} R_i s^{-1} C_i^{-1} / (R_i + s^{-1} C_i^{-1})$ of the ohmic-capacitive divider on HV side are, according to their common design, composed of a serial connection of n partial resistances, reactances or impedances. R_{LV}, $X_{C_{\mathrm{LV}}}$ respectively $\underline{Z}_{\mathrm{LV}} = R_{\mathrm{LV}} X_{C_{\mathrm{LV}}} / (R_{\mathrm{LV}} + X_{C_{\mathrm{LV}}}) = R_{\mathrm{LV}} s^{-1} C_{\mathrm{LV}}^{-1} / (R_{\mathrm{LV}} + s^{-1} C_{\mathrm{LV}}^{-1})$ acts as tapping resistor, reactance respectively impedance on LV side [Dir17].

In case of an ohmic divider with $\mathrm{Re}\{\underline{Z}_{\mathrm{HV,LV}}\} \neq 0$, the individual resistances R may change due to dissipated power P caused by Joule heating:

$$P \propto I^2 \cdot R = \frac{U^2}{R}. \tag{2.25}$$

P depends on the squared electrical current I^2 or applied voltage U^2. Hence, the resistances R_i and R_{LV} and so the scale factor M of the ohmic divider setup are additionally dependent on the input voltage U_{in}:

$$M = M(U_{in}). \tag{2.26}$$

In order to minimize this effect, the current flow through the divider needs to be reduced to less than 1 mA by use of high-ohmic resistors in the range of MΩ or higher. Moreover, long-term stability of the scale factor is necessary for HV measurements in the (sub-) ppm range. It can be obtained by availing high-quality resistors with a low TCR[16] and

[16] Temperature Coefficient of Resistance

operating the divider setup within a thermal stabilized closed environment. The TCR indicates the thermal behaviour of the resistors and is expressed as the absolute change of resistance with temperature $\delta R/\delta T$ or as the relative change $(\delta R/\delta T)/R$. These aspects are likewise considered in the design of the KATRIN HV dividers K35 and K65 and the novel G35 dedicated for usage at ESR and CRYRING@ESR (see Subsection 2.5.2).

2.5.2. The DC precision HV divider (G35)

This subsection gives an overview of the DC precision HV divider referred to as G35. Further information on operation instructions and specifications of the components installed can be found in [Win20] and may be comparable to both KATRIN HV dividers K35 and K65.

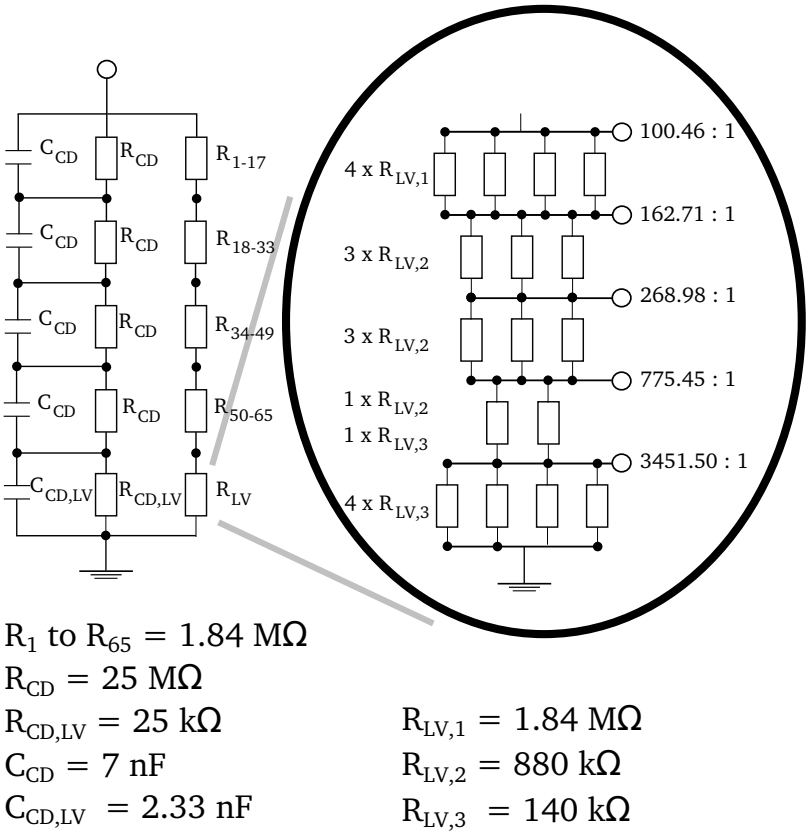

Figure 2.13.: Circuit diagram of the G35. The primary chain consists of 65 precision resistors connected in series each with $R_i = 1.84\,\mathrm{M\Omega}$ realizing the HV side. Further 16 structurally identical resistors with resistances of $R_{\mathrm{LV},1} = 1.84\,\mathrm{M\Omega}$, $R_{\mathrm{LV},2} = 880\,\mathrm{k\Omega}$ and $R_{\mathrm{LV},3} = 140\,\mathrm{k\Omega}$ constitute the tapping level or LV side with multiple scale factors M_k. The secondary divider chain is realized as an ohmic-capacitive divider with impedances $\underline{Z}_{\mathrm{CD}}$ and $\underline{Z}_{\mathrm{CD,LV}}$ functioning as high-pass filter. Therefore, it serves as precision resistor protection against HV transients. [Win20].

As illustrated in Figure 2.13, the G35 consists of two independent divider chains. A primary purely ohmic divider chain provides multiple measurement taps with scale factors M_k to be able to cover different input voltage operation ranges. A secondary ohmic-capacitive control divider chain in parallel to the primary divider chain acts as low-pass filter for protection of sensitive divider components in case of HV transients. The total primary divider resistance on HV side is realized by 65 hermetically sealed VHA518-11 precision resistors [Vis20b] manufactured by Vishay with a resistance of 1.84 MΩ each. The LV side consists of a serial connection of parallel connected identical VHA518-11 precision resistors with diverging resistance values of 140 kΩ, 880 kΩ and 1.84 MΩ. These bulk-metal foil resistors feature high long-term stability. A low TCR < 2 ppm is achieved due to the disparate thermal expansion coefficients of the ceramic substrate of the resistor chips and the meander-type film on it as shown in Figure 2.14. At temperature fluctuations, the metal film experiences mechanical deformation designed to counteract the temperature dependence of the electrical resistance of the metal. In sum, the primary divider chain consists of 81 precision resistors, including 65 for the HV side and 16 for the LV side, with a total resistance of about 120.8 MΩ.

Figure 2.14: Inside view of a Vishay VHA518-11 resistor. It consists of several resistor chips made out of a ceramic substrate with a meander-type metal film on it. The chips are mounted inside a tinned brass cylinder filled with oil for better heat distribution [A+15].

The mechanical setup of the HV divider system is depicted in Figure 3.3a. The divider is subdivided into five storeys. In each storey 17 or 16 of the resistors on HV side (level 1 to 4) and LV side (level 5) of the primary divider chain are aligned partially in a helix structure. The individual precision resistors are solderlessly connected to stainless steel connections which are mounted on POM[17] rods (in contrast to PTFE[18] rods used for the K35 and K65). The storeys are enclosed and separated by a total of six copper electrodes supported by POM rods. These shield the precision resistors from the ground potential of the stainless steel vessel covering the system (see Figure 3.3b). Further, they provide a uniform electrical field across the resistors of each level. The five partial chains of the primary divider are connected via copper electrode feed-throughs made of POM insulators. Consequently, an electrically isolated interconnection of the chains from the electrode potentials is obtained.

To avoid leakage currents, the electrode potentials are regulated to equal the potentials of the primary divider chain. This regulation takes place at the respective feed-through via the secondary ohmic-capacitive control divider. It consists of eight highly-resistive 50 MΩ Caddock MX450 power film resistors [Cad20b], whereby two resistors in parallel

[17] Polyoxymethylene; also known as acetal, polyacetal or polyformaldehyde
[18] Polytetrafluoroethylene

(a) Uncovered mechanical setup of the G35 HV divider staged on a stainless steel bottom plate.

(b) G35 HV divider with stainless steel vessel and thermal insulation material coverage and periphery on movable KANYA profile.

Figure 2.15.: Photographs of the commissioned G35 DC precision HV divider without (a) and with (b) coverage after GSI/FAIR delivery in 2019. The periphery in the lower area of the KANYA aluminium extrusion includes slow control and climate control systems which ensure thermal stabilization and a Keysight 3458A DMM with 8.5-digits precision underneath [Win20].

are shorted in each storey between the levels 1 to 4 with the copper electrodes. This results in roughly equivalent ohmic resistances between the copper electrodes and the partial chains of the primary divider. The two lowest copper electrodes, enclosing level 5 (tapping level), are each connected via two serial connected one port devices of parallel 10 kΩ and 50 kΩ Caddock MS260 power film resistors [Cad20a]. The secondary divider chain enables control measurements of the applied HV with an accuracy in the 100 ppm range. It features an independent measurement tap of scale factor $M_{\mathrm{sec}} \approx 4001$. In addition, a total of 13 Vishay MKT 1816-225/117-2 HV capacitors [Vis20a] with dielectric strength of 10 kV and capacitance of about 2.33 nF complement the secondary divider chain. In each case, three capacitors are connected and shorted in parallel between and with the copper electrodes of levels 1 to 4 realizing a parallel capacitance of approximately 7 nF. In level 5, another single capacitor is connected in parallel to the secondary tapping resistance.

The entire divider setup is staged on a stainless steel bottom plate which is mounted on a movable KANYA aluminium extrusion[19] as shown in Figure 2.15. Moreover, it is thermally insulated and stabilized at 15.0(1) °C inside the enclosing stainless steel vessel filled with dry nitrogen to prevent corona discharges. The temperature regulation is realized by a PID slow control and climate control system via 4 Pt100 sensors with $\Delta T \leq 0.05\,°C$ located in a periphery below the vessel. Further, it contains an 8.5-digits Keysight 3458A DMM (more in Subsection 2.5.3) for (sub-)ppm voltage measurements at the different measurement taps. The corresponding connections are integrated in a tap flange below the vessel base via LEMO connectors[20] (see Figure 2.16a). The input voltage from the electron cooler HV is supplied by a Heinzinger HVS65 plug [Hei20] (see Figure 2.16b) designed for voltages up to 65 kV installed on the top lid of the enclosure.

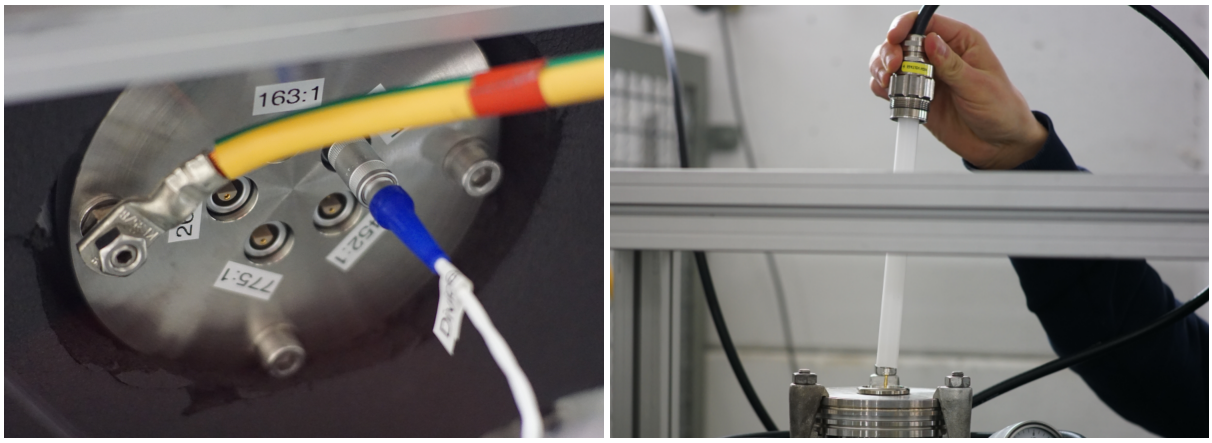

(a) Tap flange with LEMO connectors and grounding point

(b) Heinzinger HVS65 plug connection for secure HV supply

Figure 2.16.: Photographs of the G35 output tap flange (a) and the HV input socket (b) for the electron cooler HV supply. The LEMO output cable attached to the tap flange is connected to the Keysight 3458A DMM. The HVS65 plug is wired via RG11 coaxial cable from the electron cooler HV supply [Win20].

The measurement taps M_k, provided by the primary ohmic divider chain, offer the opportunity to determine the input high voltage U_{in} indirectly via measuring the output voltage U_{out} at the respective tap as introduced in Subsection 2.5.1. A major key to precision measurements besides utilizing proper measurement equipment is the precise knowledge of the scale factor M applied for voltage division. Therefore, the G35 HV divider needs to be calibrated on a regular basis. The latest calibration of the divider made use of fully traceable 1 kV calibration [Res19] using a calibrated Fluke 752A reference divider [Flu20b] on 10th of October 2018 [Win20]. The corresponding calibrated scale factors M_k along with their voltage operation ranges are shown in Table 2.1. To consider voltage dependency of the scale factors as discussed in Subsection 2.5.1, an

[19] Aluminium profile modular assembly system provided by KANYA AG
[20] Precision coaxial push-pull connectors manufactured by LEMO®

Table 2.1.: 1 kV calibration results of the G35 scale factors M_k for 15.0(1) °C divider temperature with corresponding voltage operation ranges. The calibration was performed on 10th of October 2018 [Win20].

	scale factor M_k at 15.0(1) °C / 1 kV	voltage operation ranges
M_{100}	100.46470(3) : 1	100 V – 1205 V
M_{163}	162.71444(16) : 1	1206 V – 1952 V
M_{269}	268.98943(19) : 1	1952 V – 3227 V
M_{775}	775.48495(38) : 1	3228 V – 9305 V
M_{3452}	3451.6866(23) : 1	9305 V – 35 000 V

absolute high voltage calibration method has been developed. It is suited for voltages up to 35 kV [R+19] using a dedicated calibration setup for standalone calibration independent of metrology institutes. The latest calibration measurement of the G35 with this novel method was conducted in July 2018. In the future, it will be performed on a yearly basis in addition to the 1 kV calibration leading to a more accurate scale factor characterization. The voltage dependent scale factor can be determined by [R+19]

$$M_k(U_{in}) = \underbrace{\frac{1}{a + b \cdot U_{in}[\mathrm{kV}] + c \cdot (U_{in}[\mathrm{kV}])^2 + d \cdot (U_{in}[\mathrm{kV}])^3}}_{M_{100}(U_{in})} \cdot M_{k,\mathrm{factor}} \tag{2.27}$$

with the latest absolute calibration[21] values shown in Table 2.2. For illustration purposes, the M_{100} scale factor, in dependence of the absolute input voltage U_{in}, is plotted along with statistical and systematic uncertainty band in Figure 2.17.

Table 2.2.: Absolute calibration results of the G35 voltage dependent scale factors derived from Equation 2.27 at 15.0(1) °C divider temperature conducted in July 2018 [Win20].

coefficient	value	uncertainty
a	$9.953\,744\,61 \times 10^{-3}$	2.42×10^{-9}
b	3.42×10^{-10}	4.70×10^{-10}
c	-7.6×10^{-12}	2.45×10^{-11}
d	7.20×10^{-3}	3.61×10^{-13}
$M_{100,\mathrm{factor}}$	1	–
$M_{163,\mathrm{factor}}$	1.6196176	1.5×10^{-6}
$M_{269,\mathrm{factor}}$	2.6774509	1.6×10^{-6}
$M_{775,\mathrm{factor}}$	7.7189804	2.7×10^{-6}
$M_{3452,\mathrm{factor}}$	34.357179	2.0×10^{-5}

[21] a has been taken from the more recent 1 kV calibration performed on the 10th of October 2018

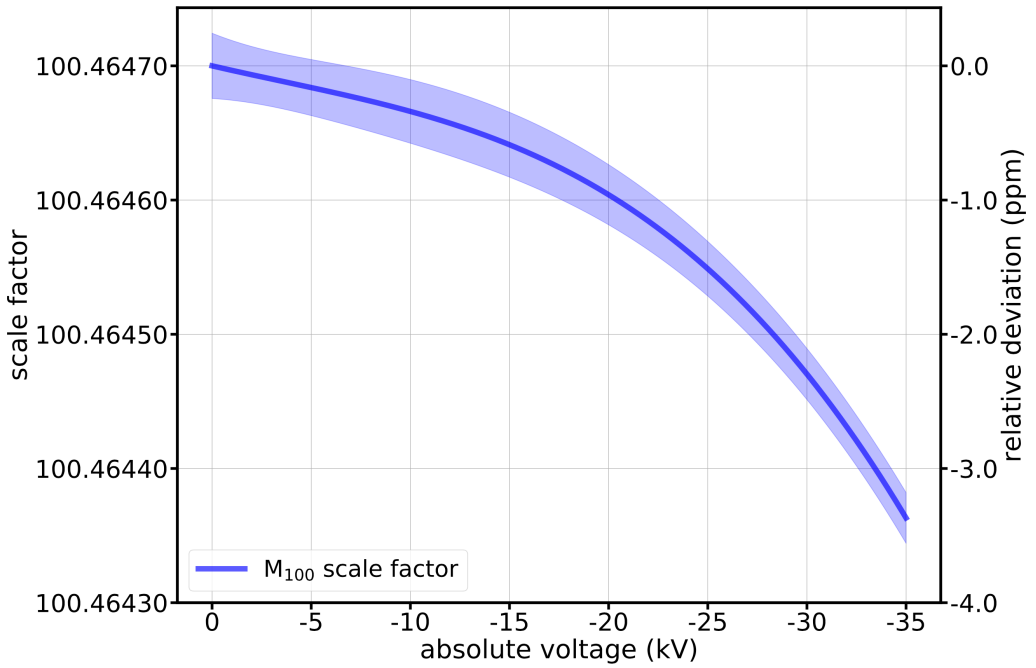

Figure 2.17.: Voltage dependency of the G35 M_{100} (100.46 : 1) scale factor with relative deviation to the scale factor value $M_0 = 1/a$ without voltage load. It has been derived from the obtained calibration coefficients listed in Table 2.2 via Equation 2.27 in a voltage range from 0 to −35 kV. The error bar includes statistical and systematic uncertainties [Win20].

2.5.3. Data acquisition

The measurement of the G35 HV divider output for both divider chains is conducted in different ways. For the secondary chain with M_{sec}, the voltage output is read out constantly during operation via a NI 9221 module. The module is connected to a CompactRIO real-time controller and monitored through a control software interface for diagnostic purposes [Win20].

Precision measurements of the primary divider chain are performed by means of a high-precision Keysight 3458A digital multimeter [Key20a], complementing the divider setup as an integral component. The voltage signal is transferred from one of the five measurement taps connected to the respective adaptor, integrated into the tap flange, to the measurement device. The DMM offers various settings for voltage measurements. These include resolutions from 4.5 to 8.5 digits for different ranges or manual NPLC[22] operation modes from 0.0001 to 1000 related to the integration time or readings per second. Table 2.3 gives an overview of the available NPLC modes with respect to their measurement accuracy. Furthermore, the device features an A-Zero mode, where a decoupled offset measurement is performed between two measurement steps. The offset is subtracted from the previous value, whereby the readings per second are reduced.

[22] Number of Power-Line-Cycles

Table 2.3.: NPLC operation modes of the Keysight 3458A DMM with respect to the measurement precision in digits and readings per second without and with A-Zero mode enabled. For integration times greater than 10 PLCs, the DMM averages the number of readings made using 10 PLCs of integration time [Key20a].

NPLC	digits	readings/sec	
		A-Zero off	A-Zero on
0.0001	4.5	83300	3440.3
0.0006	5.5	41650	2624
0.01	6.5	4415	774.7
0.1	6.5	493	204
1	7.5	50	24.5
10	8.5	5	2.5
100	8.5	0.5	0.25
1000	8.5	0.05	0.025

To perform reproducible voltage measurements with high-precision digital voltmeters, such as the Keysight 3458A DMM, these devices have to be calibrated before operation. This prevents measurement uncertainties caused by a changing reference voltage of the DMM or drifts due to thermal fluctuations and aging effects. Therefore, an offset measurement with shorted DMM inputs on the same potential has to be performed in the voltage operation range to be calibrated. This needs to be done over a certain period of time to estimate a mean offset U_{offset}. Subsequently, a gain correction factor U_{gain} can be determined by measuring a 10 V standard reference source over a time period leading to a mean gain measurement value U_{mean} via

$$U_{\text{gain}} = \frac{U_{\text{ref.}}}{U_{\text{mean}} - U_{\text{offset}}}. \tag{2.28}$$

$U_{\text{ref.}}$ denotes the calibrated voltage value of the standard reference source. Following measurements U_{meas} can then be re-calibrated (U_{real}) by knowledge of U_{gain} derived from Equation 2.28 via

$$U_{\text{real}} = (U_{\text{meas}} - U_{\text{offset}}) \cdot U_{\text{gain}}. \tag{2.29}$$

2.6. Necessity of a novel fast precision HV divider

The G35 is an HV divider designed for static (DC) measurements of the electron cooler potential difference with very high precision. In order to obtain the desired accuracy in experiments with fast changing cooler voltages as in the case of energy scanning (see Subsection 2.4.2), fast transient behaviour is a crucial factor for the divider setup. The

generalized divider transient response of a step voltage input $u_{in}(t) = U_{in}\theta(t - t_0)$[23] can be represented as

$$u_{out}(t) = U_{in}\left(Ae^{-(t-t_0)/\tau} + \frac{1}{M}\right) \tag{2.30}$$

with A and τ being initially unknown constants. M denotes the scale factor of the divider system. The time-dependent (exponential) deformation of the divided HV input voltage U_{in} is characterized by

$$\lim_{t\to\infty} u_{out}(t) = \frac{U_{in}}{M} = U_{out} \tag{2.31}$$

and has to be negligible in comparison to the measurement period. The G35 does not meet the requirement due to various capacitance influences induced by the control divider chain and interfering stray capacities of the experimental setup. This leads to a frequency-dependence of the scale factor $M(s)$.

Further investigations on frequency compensating the G35 HV divider setup were carried out by [Dir17] and [Rot19]. The method of optimizing the transient behaviour of a voltage divider system has been proposed based on the all-pass filter principle. This is realized via an adjusted capacitor chain in parallel to the ohmic divider chain (see Figure 2.12c). A detailed discussion takes place in the following Chapter 3. The results of the work of [Rot19] have shown the inability of applying frequency compensation on the existing divider setup. A desired transient response $u_{out}(t)$ relative to DC value (U_{out}) deviation

$$\left|\frac{U_{out} - u_{out}(t)}{U_{out}}\right| \sim 10\,\text{ppm} \tag{2.32}$$

with $t < 10\,\text{ms}$ is not achievable due to a lack of stability of an implemented compensation in the current working system. It was concluded that comparatively high-capacitive capacitors for stray capacity suppression with ultra-high accuracy of $\Delta C = 2.5 \times 10^{-5}$ are needed in principle.

However, this is not reachable with commercially available components, so instead a complementing fast frequency compensated add-on divider with a compact design for stray capacity reduction was proposed. Therefore, the intended divider accuracy has been downsized to 10 ppm. This downsizing is acceptable since the DMM only offers a maximum of 6.5-digits precision for a necessary integration time $< 10\,\text{ms}$ ($0.01\,\text{PLC} \mathrel{\widehat{=}} 0.2\,\text{ms}$ integration time, see Table 2.3). Also, the requirements of long-term stability can be relaxed compared to the main G35 HV divider. Rather, the G35 allows to recalibrate the complementing add-on divider before and after each measurement period. The simulations of the first proposed draft of the electrical design forecasted a capacity accuracy of about $\Delta C = 5 - 10\,\%$. This permits a far more precise compensation of the low-capacity divider system in comparison to the high-capacitive G35 HV divider implementation examined in previous work.

[23] Here, $\theta(t)$ represents the Heaviside step function also known as unit step function with $\frac{d}{dt}\theta(t) = \delta(t)$ (Dirac delta function)

Chapter 3

Theoretical aspects of voltage divider compensation

The key to divide time-dependent step voltage signals, without deformation through transient behaviour of a voltage divider, lies in frequency compensating the divider system. As introduced in Subsection 2.5.1, a voltage divider is characterized by its scale factor M, also often referred to as its inverse so-called transfer function (or attenuation)

$$H(s) := \frac{1}{M(s)} = \frac{\underline{Z}_{\mathrm{LV}}}{\underline{Z}_{\mathrm{HV}} + \underline{Z}_{\mathrm{LV}}}. \tag{3.1}$$

H is independent of frequency for $\mathrm{Im}\{\underline{Z}_{\mathrm{HV}}\} = \mathrm{Im}\{\underline{Z}_{\mathrm{LV}}\} = 0$ representing an ideal ohmic voltage divider with attenuation $A_R := H = R_{LV}/(R_{HV} + R_{LV})$. However, in practice, the behaviour of the circuit can be affected significantly by stray capacities or inner capacities of electrical devices or components connected to the (ohmic) divider circuit.

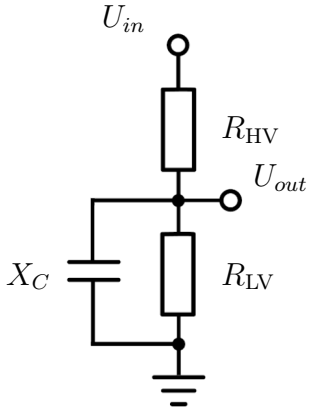

Figure 3.1: Electrical circuit of a simple ohmic voltage divider with stray capacity C in parallel to the divider resistance R_{LV} forming a frequency-dependent impedance $\underline{Z}_{\mathrm{LV}}(s) = R_{\mathrm{LV}} + jX_C = R_{\mathrm{LV}} + s^{-1}C^{-1}$ on low voltage side. The circuit acts as a low-pass filter with frequency-dependent transfer function $H = H(s)$ respectively scale factor $M = M(s)$.

In case of a stray capacitiy C in parallel to R_{LV} as illustrated in Figure 3.1, the divider acts as low pass filter. It attenuates higher frequencies more than lower frequencies and hence integrates the input signal. The output signal is exponentially deformed over time leading to deviations between the divider output signal and the corresponding ideal ohmic voltage divider response as aforesaid. In order to impedate the output divergence caused by a stray capacity C, the divider circuit has to be compensated regarding its frequency-dependence. This can be done by implementing another capacitor with a certain capacitance C' in parallel to R_{HV} as depicted in Figure 3.2. Further, the circuit needs to fulfil the all-pass condition which will be briefly derived from the general divider circuit's transfer function H in the following Section 3.1. In addition, the transient response of the voltage divider circuit is derived from Kirchhoff's circuit laws. It is discussed further in its time behaviour in consequence of frequency compensation in Section 3.2.

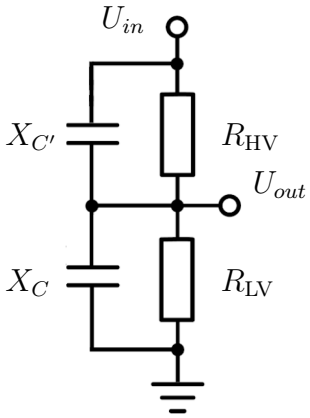

Figure 3.2: Electrical circuit of a simple ohmic voltage divider with stray capacity C in parallel to the divider resistance R_{LV} and a compensation capacitor C' in parallel to R_{HV}. Together they make up an ohmic-capacitive divider to manipulate the frequency-dependence of the divider circuit's transfer function $H = H(s)$ respectively scale factor $M = M(s)$.

3.1. Frequency domain analysis

The transfer function $H(s)$ of the ohmic-capacitive divider circuit, shown in Figure 3.2, can be computed from Equation 3.1 to

$$H(s) = \frac{U_{out}}{U_{in}} = \frac{\underline{Z}_{\mathrm{LV}}}{\underline{Z}_{\mathrm{HV}} + \underline{Z}_{\mathrm{LV}}} = \left(\frac{\underline{Z}_{\mathrm{HV}}}{\underline{Z}_{\mathrm{LV}}} + 1\right)^{-1} = \left(\frac{R_{\mathrm{HV}}}{R_{\mathrm{LV}}} \cdot \underbrace{\frac{1 + sR_{\mathrm{LV}}C}{1 + sR_{\mathrm{HV}}C'}}_{\text{freq.-dependent term}} + 1\right)^{-1}. \quad (3.2)$$

$\underline{Z}_{\mathrm{HV}} = R_{\mathrm{HV}}/(1 + sR_{\mathrm{HV}}C')$ denotes the impedance of $R_{\mathrm{HV}} \,||\, C'$. $\underline{Z}_{\mathrm{LV}} = R_{\mathrm{LV}}/(1 + sR_{\mathrm{LV}}C)$ represents the impedance of $R_{\mathrm{LV}} \,||\, C$. Both are specified by a characteristic time constant

$$\tau_i = R_i C_i. \quad (3.3)$$

The expression of Equation 3.2 is frequency-independent (compensated) if the time constants of the $R \,||\, C$ parts of the divider circuit are equal:

$$\tau_{\mathrm{HV}} = \tau_{\mathrm{LV}} \Leftrightarrow R_{\mathrm{HV}}C' = R_{\mathrm{LV}}C. \quad (3.4)$$

This relation is called all-pass compensation condition. Consequently the transfer function becomes:

$$H(s) = \frac{R_{\mathrm{LV}}}{R_{\mathrm{HV}} + R_{\mathrm{LV}}} = \frac{C'}{C + C'}. \tag{3.5}$$

Otherwise ($\tau_{\mathrm{HV}} \neq \tau_{\mathrm{LV}}$) the absolute transfer function of the circuit is given by [BV16]

$$|H(\omega)| = A_R \sqrt{\frac{1 + \omega^2 R_{\mathrm{HV}}^2 C'^2}{1 + \omega^2 \left(\frac{R_{\mathrm{HV}} R_{\mathrm{LV}}}{R_{\mathrm{HV}} + R_{\mathrm{LV}}}\right)^2 (C + C')^2}} \tag{3.6}$$

with a phase

$$\tan(\phi) = \frac{s R_{\mathrm{HV}} (C' R_{\mathrm{HV}} - C R_{\mathrm{LV}})}{R_{\mathrm{HV}} + R_{\mathrm{LV}} + s^2 C'(C' + C) R_{\mathrm{HV}}^2 R_{\mathrm{LV}}}. \tag{3.7}$$

The uncompensated voltage divider exhibits either of two cases:

- $\tau_{\mathrm{HV}} > \tau_{\mathrm{LV}}$ ($\Leftrightarrow R_{\mathrm{HV}} C' > R_{\mathrm{LV}} C$); the divider is undercompensated and serves as a differentiating (first-order) high-pass filter attenuating lower frequencies more than higher frequencies.
- $\tau_{\mathrm{HV}} < \tau_{\mathrm{LV}}$ ($\Leftrightarrow R_{\mathrm{HV}} C' < R_{\mathrm{LV}} C$); the divider is overcompensated and serves as an integrating (first-order) low-pass filter attenuating higher frequencies more than lower frequencies.

3.2. Time domain analysis

The signal transmission behaviour with its characteristic transfer function H has impact on translating time-dependent voltage signals such as AC or step voltages. In the following $u_{in}(t) = U_{in}\theta(t)$ and $S_{\mathrm{VD}}\{u_{in}(t)\} \to u_{out}(t)$ denote the idealized voltage step input and its response from an ohmic-capacitive voltage divider system S_{VD} as shown in Figure 3.2. Hence, the following equation states using Kirchhoff's first law[1]:

$$\begin{aligned} &\frac{u_{in} - u_{out}}{R_{\mathrm{HV}}} + C' \frac{d(u_{in} - u_{out})}{dt} = \frac{u_{out}}{R_{\mathrm{LV}}} + C \frac{du_{out}}{dt} \\ \Leftrightarrow\ &(C + C') \frac{du_{out}}{dt} + \left(\frac{1}{R_{\mathrm{HV}}} + \frac{1}{R_{\mathrm{LV}}}\right) u_{out} = \frac{u_{in}}{R_{\mathrm{HV}}} + C' \cdot \underbrace{\frac{du_{in}}{dt}}_{=0 \text{ for } t \neq 0} \end{aligned} \tag{3.8}$$

The rearrangement of Equation 3.8 reveals its first-order ODE[2] nature. Its solution can be immediately obtained assuming instantaneous capacitive charge with $u_{out}(0) = U_{in} C'/(C' + C)$ as [BV16]

$$u_{out}(t) = U_{in} \left[\left(\frac{C'}{C + C'} - \frac{R_{\mathrm{LV}}}{R_{\mathrm{HV}} + R_{\mathrm{LV}}} \right) e^{-t/\hat{R}\hat{C}} + \frac{R_{\mathrm{LV}}}{R_{\mathrm{HV}} + R_{\mathrm{LV}}} \right] \tag{3.9}$$

[1] Assuming an infinite current flow at time $t = 0$, i.e. neglecting a finite resistance of the voltage supply

[2] Ordinary Differential Equation

where $\hat{C} = C + C'$ and $\hat{R} = 1/R_{\mathrm{HV}} + 1/R_{\mathrm{LV}}$. The output signal $u_{out}(t)$ takes the form introduced in Equation 2.30. The relative deviation to DC ($U_{out} = U_{in}/M$) vanishes for $R_{\mathrm{HV}}C' = R_{\mathrm{LV}}C$ (compare all-pass compensation condition, see Equation 3.4). The behaviour of the transient response differs for an overcompensated ($R_{\mathrm{HV}}C' > R_{\mathrm{LV}}C$) and undercompensated ($R_{\mathrm{HV}}C' < R_{\mathrm{LV}}C$) divider as illustrated in Figure 3.3.

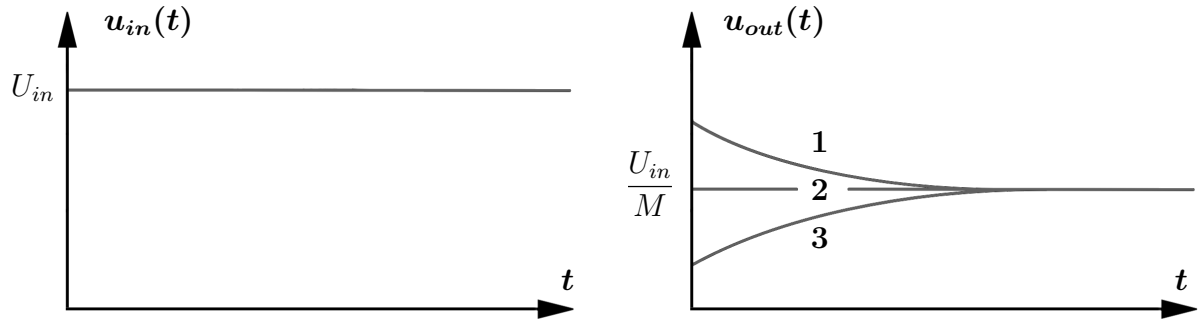

(a) Ideal voltage step input $u_{in}(t) = U_{in}\theta(t)$ **(b)** Transient response $S_{\mathrm{VD}}\{u_{in}(t)\} \rightarrow u_{out}(t)$

Figure 3.3.: Sketch of an ideal voltage step input (a) and the corresponding transient response (b). Illustrated for an undercompensated (1), compensated (2) and overcompensated (3) ohmic-capacitive voltage divider system S_{VD} for $t > 0$.

If $R_{\mathrm{HV}}C' \neq R_{\mathrm{LV}}C$, the output voltage follows an asymptotic behaviour for $t \rightarrow 0$ and $t \rightarrow \infty$, whereby for short times ($t \ll \hat{R}\hat{C}$), it applies

$$\lim_{t \to 0} u_{out}(t) = U_{in}\frac{C'}{C + C'}. \tag{3.10}$$

For long times ($t \gg \hat{R}\hat{C}$), as already introduced in Section 2.6, the output is determined by the values of resistance, i.e. the frequency-independent (DC) scale factor M, as

$$\lim_{t \to \infty} u_{out}(t) = U_{in}\frac{R_{\mathrm{LV}}}{R_{\mathrm{HV}} + R_{\mathrm{LV}}} = U_{in}A_R = \frac{U_{in}}{M} = U_{out}. \tag{3.11}$$

Thus, voltage divider disturbances through undesirable capacities in parallel to the resistances can be suppressed via frequency compensation. For instance, this technique is applied for frequency-independent dividing test probes (e.g. oscilloscope probes or current probes) using variable capacitors for fine-tuned compensation. Furthermore, such concept shall be implemented into the novel fast precision high voltage divider dealt with in the following Chapter 4.

Chapter 4

Design of the novel fast precision HV divider

The opportunity of frequency compensating the finalized G35 HV divider system comes along with various challenges. The mastery of which is highly unlikely as investigated in [Rot19] and furthermore discussed in Section 2.6. As a result, a novel fast precision HV divider was proposed and later commissioned. It features a compact design aiming for capacitance reduction and slight transient behaviour. Hence, the requirements in accuracy and long-term stability have been downsized since it will be operated as an add-on to the pre-existing G35 setup. Thereby, the G35 will function as a high-precision reference divider for pre- and post-measurement calibration. The novel add-on divider needs to provide multiple scale factor settings ensuring a voltage operation range to a desired limit of 20 kV. Also the output should be compatible to the read-out electronics integrated into the pre-existing HV measurement setup, so it can serve both divider types. The installation of the divider onto the KANYA aluminium extrusion of the current setup is striven. A first draft of the electrical design of the novel fast precision HV divider, including a switching system for tap specific frequency compensation, has been elaborated in [Rot19]. However, it was rejected in favor of a more elegant and easier to implement concept. In the following Section 4.1 this concept is set out and subsequently simulated for verification in Section 4.2. The mechanical setup is realized on the basis of the custom-made HV divider which is utilized for absolute HV calibration of the K35, K65 and G35 HV dividers [R+19]. A more detailed outline of the mechanical setup is introduced in Section 4.3.

4.1. Electrical design

Unlike the G35, the novel fast precision HV divider consists of one primary ohmic-capacitive divider chain providing a single physical measurement tap M as illustrated in Figure 4.1. This measurement tap offers three different scale factors (94 : 1, 1027 : 1 and 1961 : 1) depending on the total LV side impedance changeable via S_1 and S_2 toggle switches.

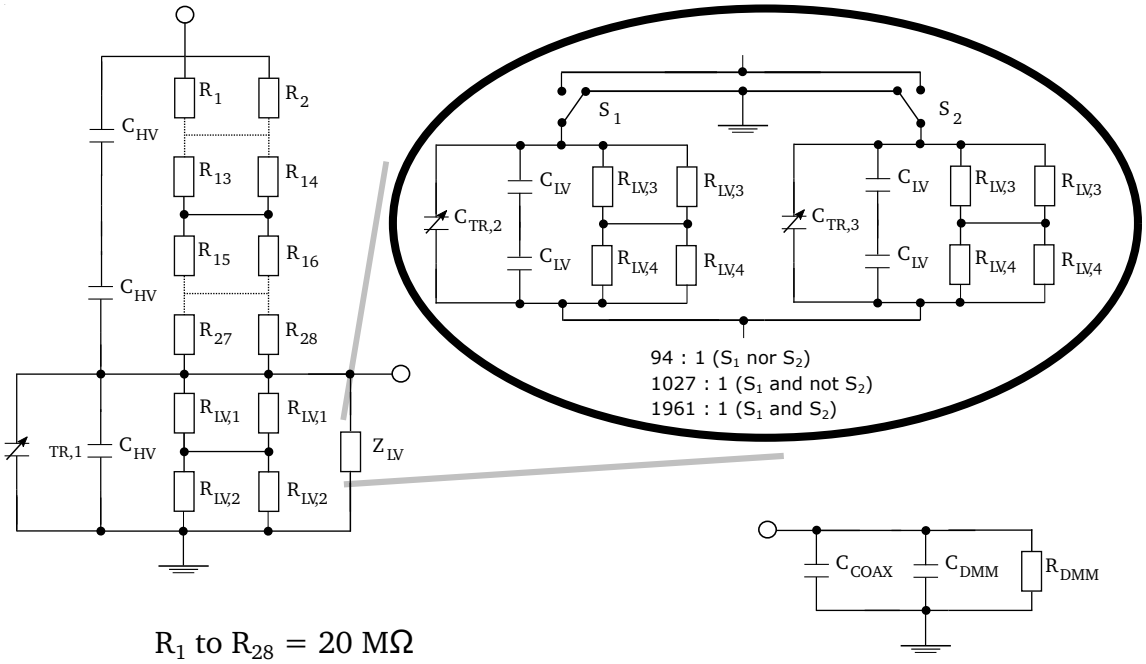

R_1 to R_{28} = 20 MΩ
$R_{LV,1}$ = 2 MΩ
$R_{LV,2}$ = 1 MΩ
$R_{LV,3}$ = 200 kΩ
$R_{LV,4}$ = 100 kΩ
R_{DMM} = >10 GΩ

C_{HV} = 18 pF
C_{LV} = 16.5 nF
C_{COAX} = 100 pF/m
C_{DMM} = 270 pF
$C_{TR,i}$ = 20...640 pF

Figure 4.1.: Circuit diagram of the novel fast precision HV divider with frequency compensation and estimated equivalent circuit of the corresponding measurement setup. The latter consists of a measurement device (digital multimeter, DMM) and a two pole (coaxial, COAX) measurement cable. The primary chain consists of three HV capacitors with $C_{HV} = 18\,\text{pF}$ and 28 precision resistors with $R_i = 20\,\text{M}\Omega$ each, realizing the HV side. Another 12 structurally identical resistors with resistances of $R_{LV,1} = 2\,\text{M}\Omega$, $R_{LV,2} = 1\,\text{M}\Omega$, $R_{LV,3} = 200\,\text{k}\Omega$ and $R_{LV,4} = 100\,\text{k}\Omega$ constitute the tapping level (or LV side) together with further $C_{LV} = 15\,\text{nF}$ LV capacitors. The measurement tap offers multiple scale factors M_k through switchable impedances. These can be selected via toggle switches $S_{1,2}$. Fine-tuned frequency compensation is reached by means of additionally LV side connected variable capacitors $C_{TR,1}$, $C_{TR,2}$ and $C_{TR,3}$.

The entire divider system is aiming for frequency compensation (see Chapter 3). For this purpose, the additional capacitors, in parallel to the partial ohmic divider chains, serve as compensation capacitances to the (estimated) induced disturbance capacities $C_{\mathrm{DMM}} \approx 270\,\mathrm{pF}$ [Dir17] and $C_{\mathrm{COAX}} \approx 100\,\mathrm{pF/m}$ of the measurement device (DMM) and coaxial cable (COAX) connected to the measurement tap. Further fine-tuning of the voltage divider time constants τ_i shall be applied via a total of three variable capacitors (TR), each in parallel to the compensation capacitors.

Figure 4.2: Model of the Caddock USF-300 Series ultra-stable low TCR ultra-precision metal film resistors. They are constructed with an aluminum oxide ceramic surrounding for high thermal conductivity [Cad20c].

Table 4.1.: Specifications of the Caddock type USF-371 & USF-340 ultra-stable low TCR ultra-precision metal film resistors which make up the composition of the ohmic divider chain of the novel fast precision HV divider [Cad20c].

	USF-371	USF-340
resistance in MΩ tolerance in %	20.0 ±0.01	2.0/1.0/0.2/0.1 ±0.01
dielectric strength in V	2500	300
voltage coefficient in ppm/V	≤ 0.02	≤ 0.02
TCR (−40 °C to 85 °C, referenced to 25 °C) in ppm/°C	5	5
power dissipation (at 85 °C)	0.75	0.33

On HV side, the ohmic divider resistance is realized by fourteen-fold serial connection of two type USF-371 ultra-stable low TCR ultra-precision metal film resistors manufactured by Caddock. These are connected in parallel with 20 MΩ resistance and 2.5 kV dielectric strength each. The LV side consists of type USF-340 resistors with 2 MΩ, 1 MΩ, 0.2 MΩ and 0.1 MΩ resistance and 300 V dielectric strength each also connected by two in parallel. Both types belong to the Caddock USF-300 Series and are similarly designed in two different dimensions according to their overall resistance as shown in Figure 4.2. Further specifications retrieved from the data sheet [Cad20c] are listed in Table 4.1. TCR and power dissipation drift of the resistors are extremely low. This is due to a surrounding aluminum oxide ceramic layer causing high heat flow away from the resistance material inside. The two-resistances-in-parallel circuit design serves the purpose of measurement device protection in case of harmful HV emergence as a consequence of breakage of a single resistor. Overall, a total of 40 precision resistors are installed into the ohmic divider chain.

The capacitive chain on HV side is composed of two serial connected K15Y-1 ceramic HV doorknob capacitors each with about 18 pF. Formerly, these capacitors were used in Russian military for powerful radio equipment working in continuous high-frequency mode in DC or pulsed circuits. They feature high dielectric strength of 10 kV each and allow an overall strength of 20 kV in serial connection. Further specifications are listed in Table 4.2.

Table 4.2.: Specifications of the Russian military K15Y-1 ceramic HV doorknob capacitors used for the capacitive chain of the novel fast precision HV divider.

	K15Y-1
capacitance in pF tolerance in %	18.0 ± 10
dielectric strength in kV	10
insulation resistance in GΩ	> 10
temperature operation range in °C	−60 to 155

Due to missing characterization of the capacitors beyond the specified ±10 % tolerance range and the high sensitivity of the capacitance chain on HV side regarding frequency compensation, a total of eight pieces were requested. Each of them was precisely measured regarding their capacity C and dissipation factor D. The latter denotes the loss-rate of energy absorbed by the dielectric material when an AC signal is applied, i.e. the ratio of the real equivalent series resistance $\mathrm{Re}\{\underline{Z}_\mathrm{C}\}$ and the reactance $\mathrm{Im}\{\underline{Z}_C\} = X_C$ of the capacitor impedance $\underline{Z}_C$. The measurement took place by means of an Aim-TTi LCR400 precision LCR bridge [Aim20], whereby the capacitor of interest was fixed at an external

Table 4.3.: Results of the 4-terminal C+D measurement of the K15Y-1 ceramic HV doorknob capacitors utilizing the Aim-TTi LCR400 precision LCR bridge in parallel equivalent circuit mode at 10 kHz test frequency. The pieces were labeled by K15Y-1-X to be distinguishable. Accuracy limits of the measurement mode are retrieved from [Aim20].

	capacitance C in pF	dissipation factor D
K15Y-1-1	17.27(35)	0.0105
K15Y-1-2	17.62(36)	0.0109
K15Y-1-3	21.17(43)	0.2475
K15Y-1-4	18.38(37)	0.0211
K15Y-1-5	17.75(36)	0.0100
K15Y-1-6	18.52(37)	0.0097
K15Y-1-7	17.90(36)	0.0099
K15Y-1-8	17.74(36)	0.0098

4-terminal connection. Further, it was measured in parallel equivalent circuit mode at 10 kHz test frequency. This offers an accuracy limit of 2 % ± 1 digit in a capacitance range of 5 pF to 200 µF. The results of the labeled K15Y-1 capacitors are listed in Table 4.3. Except for K15Y-1-3, all capacitors could be characterized within 5 % deviation to the declared value of 18 pF with a dissipation factor of about 1 − 2 %. This leads to a negligible equivalent series resistance and heat dissipation for low current values as in case of the add-on divider.

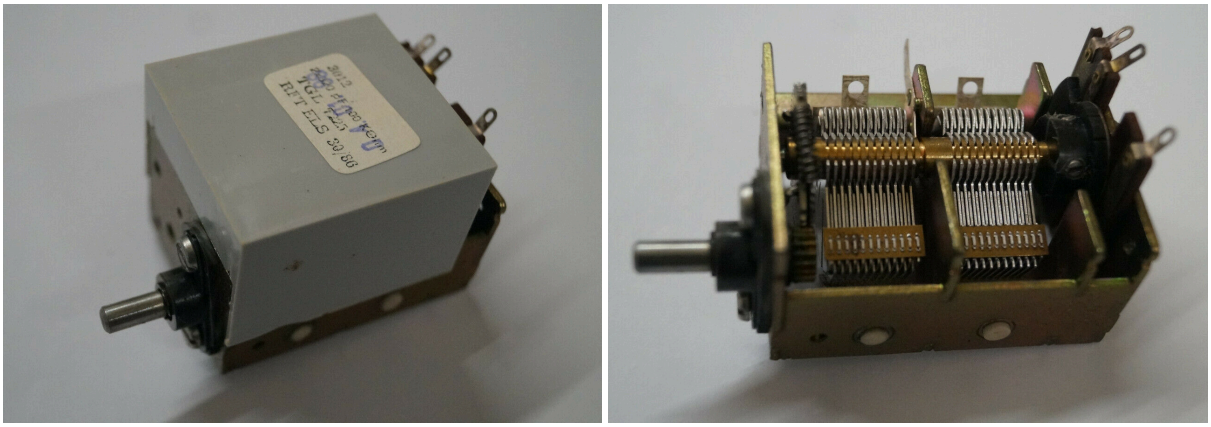

(a) Exterior view with ceramic-insulated stator **(b)** Interior view with two-section division

Figure 4.3.: Exterior (a) and interior (b) view of the variable air capacitor with fine control shaft (1 : 3), ball-bearing axis of 4.2 mm diameter and a ceramic-insulated stator. It is divided into two sections of 320 pF maximum capacity each. Further, it features an additional 100 kΩ-potentiometer which will not be in use for the divider setup.

On the one hand, The tapping level (LV side) of the capacitive divider chain consists of three two-section variable air capacitors shown in Figure 4.3. They are made up of two (stator and rotor) sets of semicircular metal plates. Those are separated by air gaps in each section with one set (rotor) attached to a fine control shaft (see Figure 4.4).

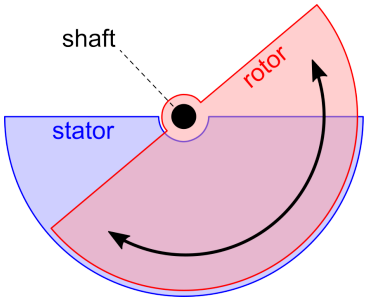

Figure 4.4: Principle of the variable air capacitor with fixed (stator) plate and rotatable (rotor) plate via shaft control [Sá14].

This allows a manual rotation of the assembly resulting in a capacitance shift due to the changing overall metal plate overlap of the two sets. One section achieves a minimum capacity of about 10 pF at minimum overlap and a maximum capacity of about 320 pF at maximum overlap. All three variable capacitors, realizing $C_{\mathrm{TR,i}}$, will be operated

with in parallel two-section interconnection. This allows a broader capacitance tuning range of about 20 to 640 pF. Hence, they enable to (re-)adjust the capacitive chain impedance aiming for maximum frequency compensation. The electrical connection of the independent capacitance sections is accomplished via solder terminals. On the other hand, another K15Y-1 capacitor is used in parallel to the permanent LV side resistance along with four 16.5 nF ± 5 % type KP-1832 polyester film capacitors by ERO (Vishay-Röderstein). The latter complement the switchable LV impedances for scale factor M_i variation in two-pair serial interconnection. More specifications of this capacitor type are listed in Table 4.4.

Table 4.4.: Specifications of the ERO (Vishay-Röderstein) type KP-1832 polyester film capacitors used for the switchable impedances of the novel fast precision HV divider on LV side.

	KP-1832
capacitance in nF tolerance in %	16.5 ± 5
dielectric strength in V	2000
insulation resistance in GΩ	> 1
temperature operation range in °C	-

4.2. Transient response simulation

Before mechanical planning and realization of the future add-on divider, its analog circuit design, discussed in Section 4.1, has been simulated regarding its transient response behaviour, i.e. the time-dependency of the implemented scale factors

$$M_i^{\text{sim.}} = M_i^{\text{sim.}}(t). \tag{4.1}$$

At first, this was accomplished by means of `Lcapy` [Mic20], a Python package for linear circuit analysis. Later, it was verified by the SPICE[1]-based analog electronic circuit simulator LTspiceXVII [Ana20]. The time-dependent scale factor simulation $M_i^{\text{sim.}}(t)$ can be described as the ratio:

$$M_i^{\text{sim.}}(t) = \frac{u_{in}^{\text{sim.}}(t)}{u_{out,i}^{\text{sim.}}(t)}. \tag{4.2}$$

The counter $u_{in}^{\text{sim.}}(t)$ denotes the computed input step function of 1 kV offset and finite 12 V/µs slew rate[2] at the HV input circuit node. The denominator $u_{out,i}^{\text{sim.}}(t)$ represents the computed output function at the tapping node.

[1] Simulation Program with Integrated Circuit Emphasis; general-purpose, open-source analog electronic circuit simulator

[2] The slew rate was chosen based on the Kepco Model BOP 1000m amplifier [Kep11] utilized for measurements treated later in this thesis and used for voltage detuning at the CRYRING@ESR electron cooler.

The computation took place via linear circuit analysis applied to an equivalent circuit[3] based on the electrical design (see Section 4.1) of the passive electronic components illustrated in Figure 4.1. The simulation was performed on all three scale factor settings $94:1$ (S_1 off and S_2 off) as shown in Figure 4.5, $1027:1$ (S_1 on and S_2 off) as shown in Figure A.1 and $1961:1$ (S_1 on and S_2 on) as shown in Figure A.2. The latter two are part of Appendix A. Each setting has been analyzed, on the one hand, with no tuning capacitance $C_{\mathrm{TR},i}$ integration and, on the other hand, with $C_{\mathrm{TR},i}$ simulated in parallel to the LV side impedance. Since the fine controls of the variable air capacitors only offer a finite tuning precision, the corresponding tuning range of about $\pm 2\,\mathrm{pF}$, deviating from its ideal value, is considered as well.

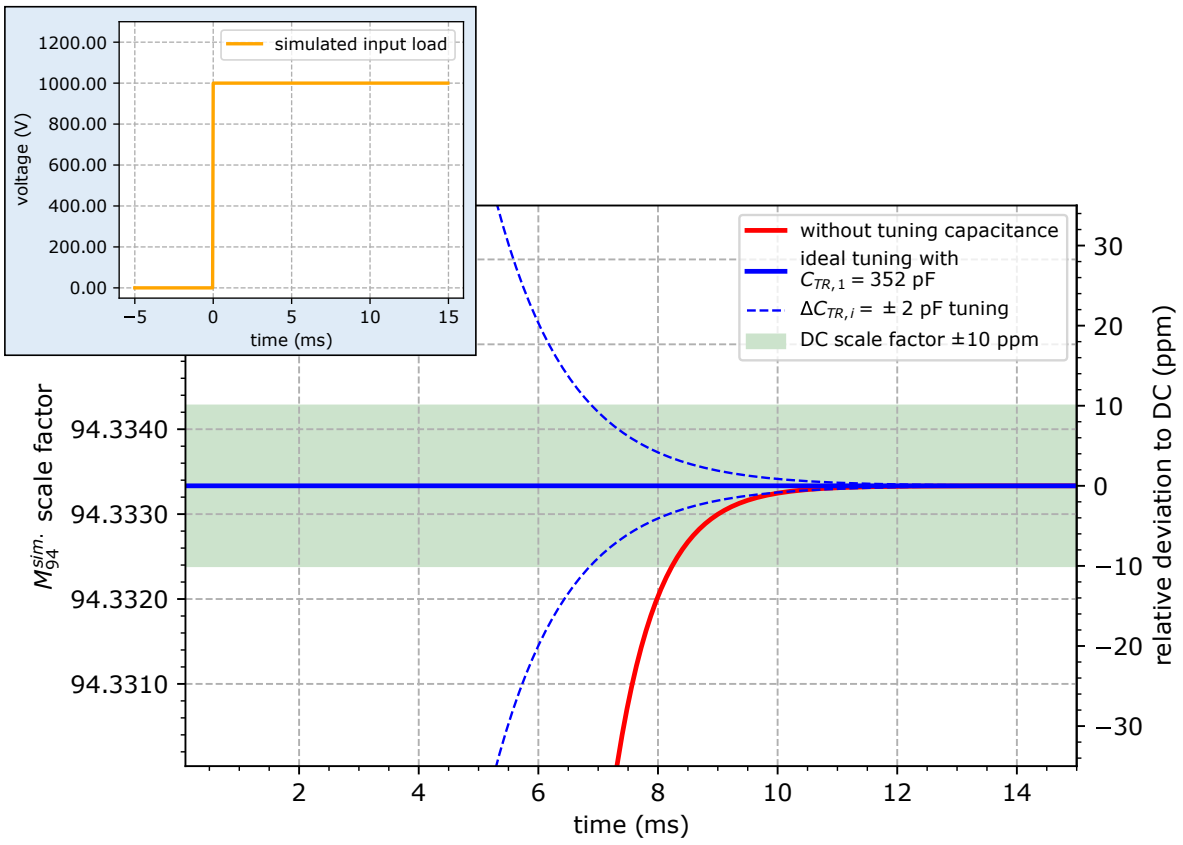

Figure 4.5.: Scale factor $M_{94}(t)$ time domain simulation over a period of 15 ms at simulated 1 kV input step load (shown upper left) of $12\,\mathrm{V/\mu s}$ slew rate with its relative deviation to the ideal DC scale factor $M_{94}^{\mathrm{DC,sim.}}$ in ppm. The plot shows the simulated transient response behaviour with no tuning capacitance (red) and with an ideal tuning of $C_{\mathrm{TR},1} = 352\,\mathrm{pF}$ (blue). The latter leads to complete frequency compensation. Furthermore, it shows the transient response range reachable with $\Delta C_{\mathrm{TR},1} = \pm 2\,\mathrm{pF}$ tuning accuracy of the variable air capacitor according to a finite tuning precision.

[3] For the measurement cable a length of $L = 2\,\mathrm{m}$ was assumed, so its capacitance was estimated to $C_{\mathrm{COAX}} = 200\,\mathrm{pF}$

The transient responses of the different scale factors M_i provided by the divider circuit, in dependence of the settings of S_1 and S_2, meet the requirements set for the novel fast precision HV divider in an idealized setup. The transient $M_i^{\text{sim.}}(t)$ relative to DC $M_i^{\text{DC,sim}}$ deviation fulfills

$$\left| \frac{M_i^{\text{DC,sim.}} - M_i^{\text{sim.}}(t)}{M_i^{\text{DC,sim.}}} \right| \sim 10\,\text{ppm} \tag{4.3}$$

within a time slice of 10 ms (see Section 2.6) despite under- and overcompensation through capacitance uncertainties of the planned physical setup. This arguably indicates low sensitivity of the divider transient response regarding its capacitve chain for the desired purpose. However, frequency compensation, leading to a more shortened time interval to reach $< 10\,\text{ppm}$ accuracy, is only possible via capacitance tuning. As the simulations demonstrate, (ideal) all-pass compensation of any of the three scale factors lies within the range reachable with $C_{\text{TR},i}$ at tuning values of $C_{\text{TR},1} = 352\,\text{pF}$ and $C_{\text{TR},2} = C_{\text{TR},2} = 150\,\text{pF}$. It follows

$$\tau_{\text{HV}}^{\text{ideal}} = \tau_{\text{LV}}^{\text{ideal}} = 1.26\,\text{ms}. \tag{4.4}$$

Estimating a capacitance tuning precision of $\Delta C_{\text{TR},i} = \pm 2\,\text{pF}$ for the variable air capacitors being used, $< 10\,\text{ppm}$ relative deviation to DC may be reached in less than 7 ms. This includes re-adjusting $C_{\text{TR},i}$ based on the real capacitance values of the setup.

4.3. Mechanical design

Unlike the G35 HV divider, which is encased in a customized stainless steel vessel, the novel fast precision HV divider is covered in a commercial Rittal AE 1037.500 (400 cm × 800 cm × 300 cm) enclosure [Rit20] with IP[4] 66 protection according to IEC[5] 60529. On the one hand, it consists of an edged and welded piece of 1.25 mm thick steel sheet. On the other hand, it features a door also made of steel sheet of 1.5 mm thickness with circumferential foamed-on PU[6] gasket mounted via two screwed door hinges. The door is lockable via two fasteners with double-bit application according to DIN[7] 43668. Moreover, the enclosure provides a gland plane in the base and a galvanized 2 mm thick steel mounting plate attached on four depth-adjustable studs in the back. Since there is no intend to operate the HV divider in a dry nitrogen environment, this solution for coverage was preferred over a customized vessel. One advantage is the easy access to the inner structure of the divider, especially the tuning control for optimizations and repair work. In addition, it allows a convenient attachment onto the movable KANYA profile of the HV measurement setup as planned and visualized in Figure 4.6.

Inside the enclosure, the HV divider is assembled on a PLA[8] structure attached to the mounting plate (see Figure 4.7). This allows a centered positioning of the divider

[4] Ingress Protection (Code)
[5] International Electrotechnical Commission standard
[6] Polyurethane; also abbreviated with PUR
[7] German Institute for Standardization (from German *Deutsches Institut für Normung*) standard
[8] Polylactide

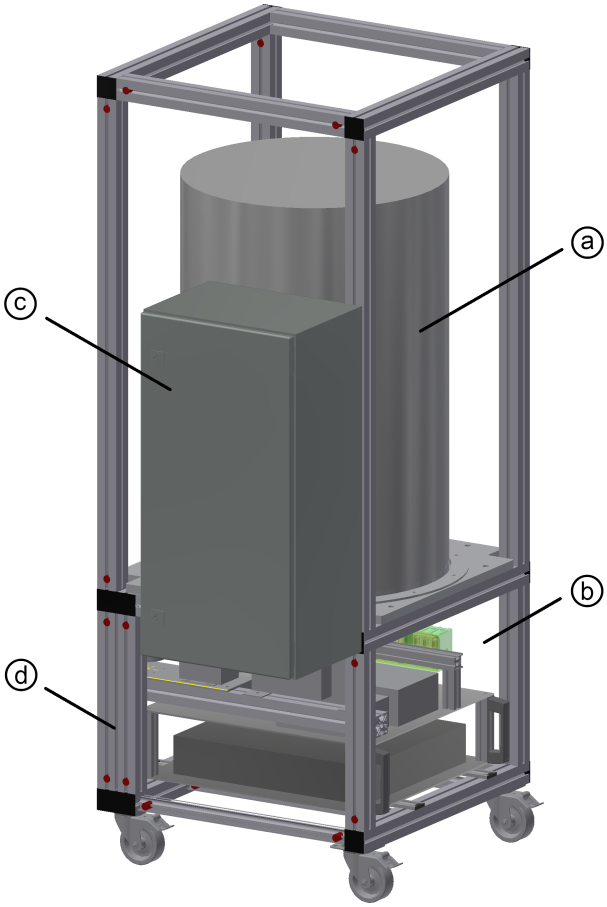

Figure 4.6: CAD model of the HV measurement setup including the G35 HV divider (a) and the periphery (b) with the Rittal AE 1037.500 enclosure (c) attached onto the movable KANYA profile (d).

setup in all three dimensions to minimize the influence of stray capacitances induced by the Faraday cage. The structure consists of a HV panel jack fixation and four main mounting stages of 8 mm thickness along with six partial resistor holders fastened in between. All PLA components were additive manufactured (3D printed). Further, these were characterized with $> 1\,\mathrm{T\Omega}$ HV insulation for voltages up to 5 kV using a GMC Metriso 5000 A/AK analog HV insulation measuring instrument [GMC20]. To enable HV input socket compatibility with the G35 main divider, an identical Heinzinger HVS65 panel jack [Hei20] is installed. The divider is physically subdivided into three storeys for the purpose of stabilization of the holder structure and the K15Y-1 capacitor fixation. The two upper storeys each include one of the HV capacitors and 14 Caddock type USF-371 resistors jointly realizing the permanent HV side of the divider with 20 kV dielectric strength. The lower storey contains the LV side impedances, i.e. the Caddock type USF-340 resistors, the ERO (Vishay-Röderstein) type KP-1832 polyester film capacitors and the remaining K15Y-1 capacitor in parallel to the permanent $1.5\,\mathrm{M\Omega}$ resistance. Next to the PLA structure, the variable air capacitors are located and likewise attached to the mounting plate along with two toggle switches in between (not shown). Altogether, they form the outer control unit for capacitance tuning and scale factor toggling. Further enclosure modifications referring to HV input connection, output routing, grounding as well as the wiring of the outer control unit for capacitance tuning and scale factor toggling will be discussed in detail in the following Chapter 5.

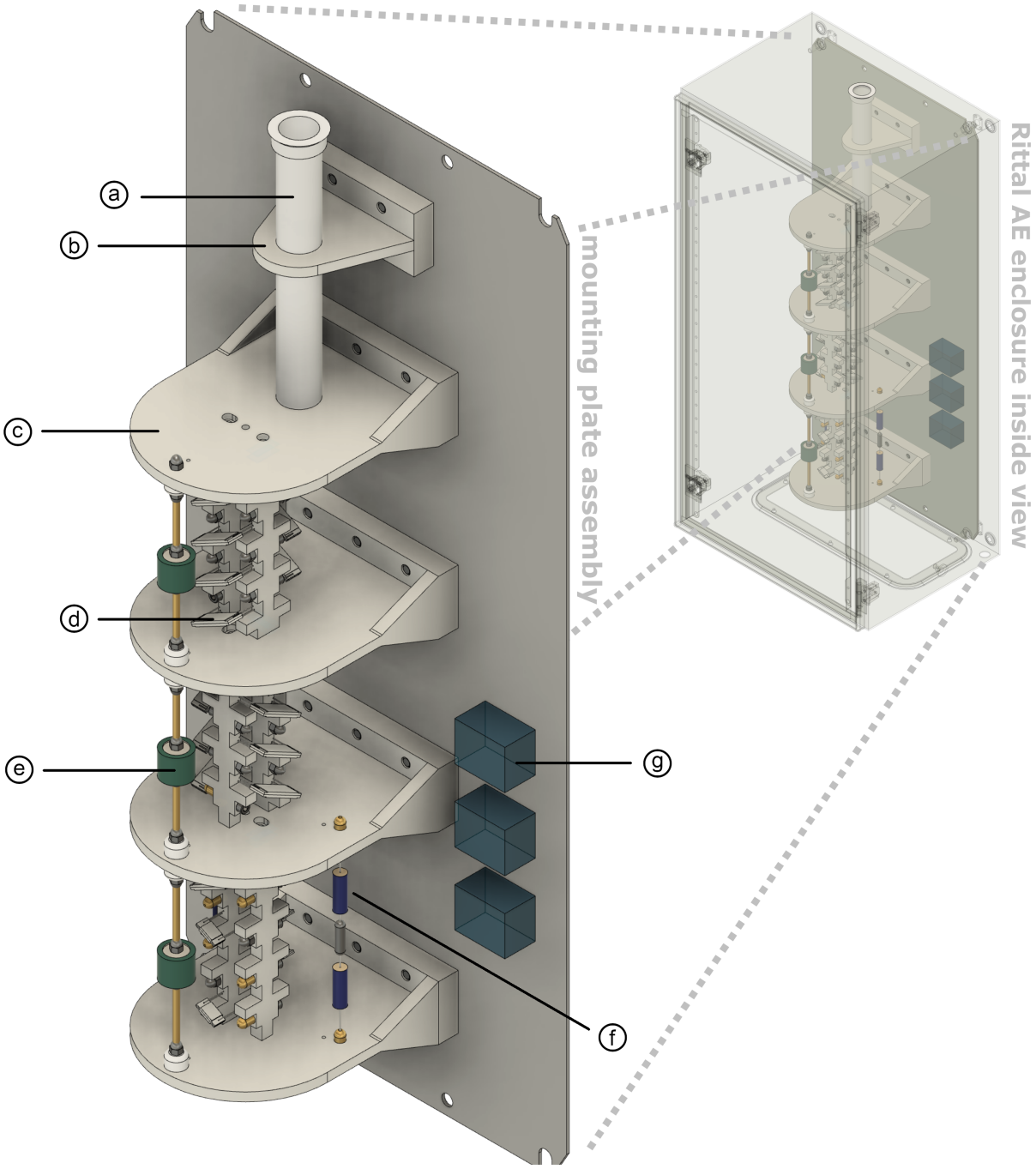

Figure 4.7.: Conceptual design plan of the interior assembly of the Rittal AE 1037.500 divider enclosure. Its components are a Heinzinger HVS65 panel jack (a), a PLA panel jack fixation (b), PLA mounting stages (c) with partial resistor holders for 40 Caddock type USF-300 Series resistors (d), three type K15Y-1 HV doorknob capacitors with brass threaded rod fixation and interconnection (e), four ERO (Vishay-Röderstein) type KP-1832 polyester film capacitors fastened on brass feed-throughs (f) and three variable air capacitors (g) attached to the steel mounting plate.

Chapter 5

Final assembly & first test measurements

This chapter deals with the final setup of the novel fast precision HV divider as well as first test measurements corresponding capacitance tuning and scale factor calibration. The divider was built and characterized in the HV laboratory of the Institute of Nuclear Physics in Münster. For this purpose, measurement devices on-site and further HV equipment carried from the KATRIN experiment in Karlsruhe were used. Moreover, in the course of this work, two 6.5-digits Keysight 34465A DMMs [Key20c] have been utilized for fast precision measurements. The DMMs allow digital readout over PC-standard I/O such as TCP/IP[1] and USB[2] via VISA[3] standard API[4]. In the following, the main foci regarding construction topics are the mechanical installation of the divider structure on the mounting plate and the outer control unit implementation. The latter includes the toggle switches along with the electrical wiring of the divider components and the output routing via dedicated output measurement cable. The construction took place with the support of the precision engineering and electronics workshop at the Institute of Nuclear Physics. The additive manufactured components have been printed via a Raise3D Pro2 Series 3D printer [Rai20] staged in the institute as well. Technical drawings of all printed parts are attached in Appendix B. An assessment of the intended use of the PLA 3D print material as HV divider holders was given from the HV insulation measurement in Section 4.3.

[1] Transmission Control Protocol/Internet Protocol
[2] Universal Serial Bus
[3] Virtual Instrument Software Architecture
[4] Application Programming Interface

5.1. Setup of the novel fast precision HV divider

As indicated above, the internal divider setup has completely been assembled in the HV laboratory of the Institute of Nuclear Physics. During such work, all conductive parts were treated with considerable caution to minimize impurities from the working space what enables a clean setup. After delivery of the Rittal AE 1037.500 enclosure, it was handed over to the precision engineering workshop for bores regarding the HV plug connector (see Subsection 5.1.1), the measurement tap (see Subsection 5.1.3), the toggle switches together with the variable air capacitor shafts (for both see Subsection 5.1.4) composing the outer control unit. In addition, 28 bores of 8 mm in diameter were drilled into the mounting plate for the PLA plug connector fixation and the PLA mounting stages. A complete overview of the finalized inner enclosure setup is depicted in Figure 5.1 and will be outlined in the following.

Figure 5.1: Front view of the completed HV divider setup inside the post-processed Rittal AE 1037.500 enclosure with through holes regarding the HV plug connector (top-centre), the toggle switches together with the variable air capacitor shafts (centre-left) and the measurement tap connection (bottom-left).

5.1.1. HV input connection

The HV input connection has been realized with a Heinzinger HVS65 panel jack (see Figure 5.2) identical to the installed HV input connection at the main G35 HV divider. It is fastened at a hole through of 37 mm in diameter at the top side of the enclosure by means of a nut element screwed to the threads of its steel head. Furthermore, it is supported by the PLA panel jack fixation.

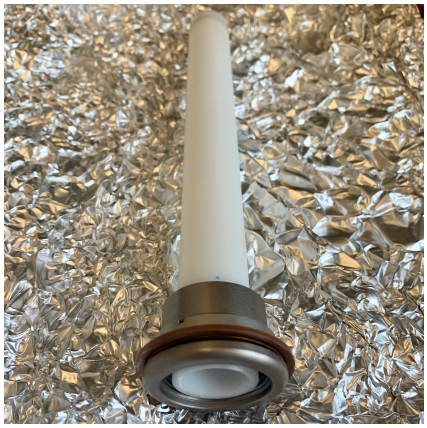

Figure 5.2: Heinzinger HVS65 panel jack for HV input connection. It is made of a (female) cylindrical PTFE plug element and a screw threaded connector steel head customized with an additional copper ring.

Besides its head, the connector consists of a (female) cylindrical plug element made of PTFE and an HV contact node at the other end of the panel jack (not shown) with threaded rod feed-through. To ensure electrical contact between the connector head and the powder-coated steel sheet of the enclosure, the coating on the inside has been removed around the through hole. Moreover, a copper ring has been added to the connector head fixation to guarantee widespread contact with the exposed steel sheet. The panel jack is wired to the divider chains by use of a brass feed-through screwed to the threaded rod of the HV contact node.

5.1.2. Configuration of the divider chains

A detailed view of the divider chain configurations in the separated storeys is shown in Figure 5.3 and 5.4. The partial resistor holders are fastened in-between the mounting stages via plastic screws to prevent disturbances caused by signal interference of loose conductor components. Since the additive manufacturing process of the partial resistor holders did not allow the print of threaded holes, these were post-processed. Hence, the parts were printed with pilot holes offering an appropriate support structure for the subsequent drill. All PLA structure parts were cleaned and freed from stringings before installation on the mounting plate.

The Caddock type USF-300 Series resistors are paired and plugged in sockets soldered on 5 mm soldering eyelets. They are fixed on 5 mm through holes of the resistor holders via stainless steel M5 hexagon screws and corresponding cap nuts forming a gradual chain. At both ends of the partial resistor chains screw-type brass feed-throughs are used to connect to the HV panel jack and to interconnect the partial chains. The feed-throughs

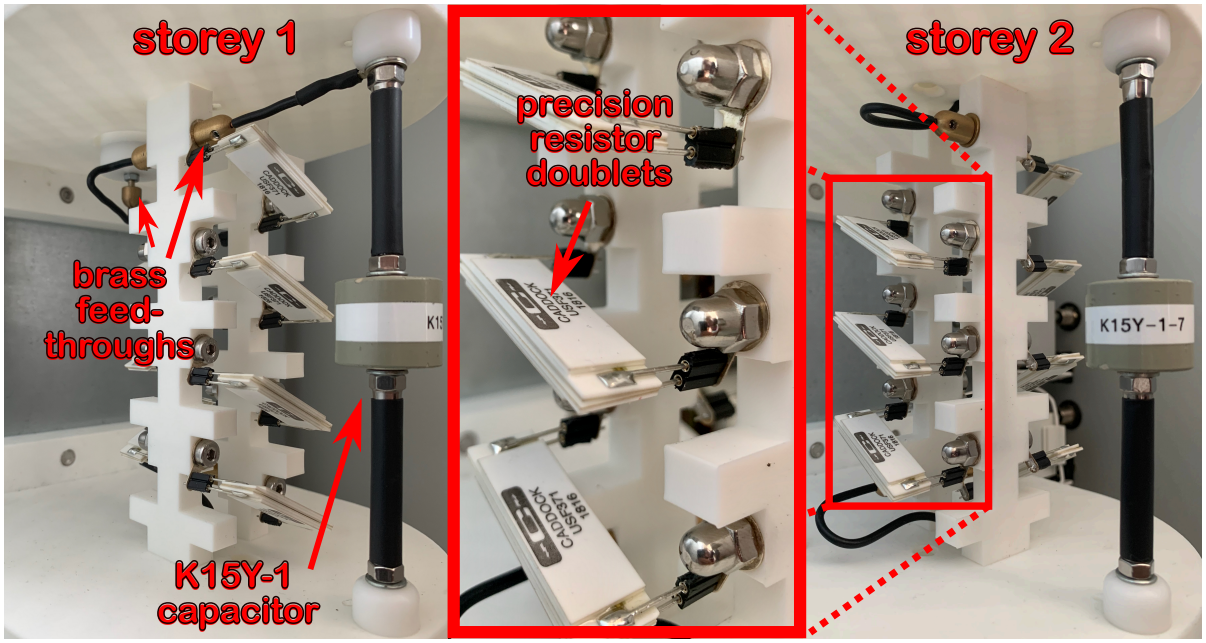

Figure 5.3.: Close-up view of storey 1 (left) and storey 2 (right) of the internal HV divider setup. It shows the vertical capacitance chain made of K15Y-1 HV doorknob capacitors and the gradual partial resistor chains realized by Caddock type USF-300 Series resistor doublets interconnected via purpose-built brass feed-throughs.

were purpose-built in the precision engineering workshop. On the other hand, the K15Y-1-5 and K15Y-1-7 labelled HV doorknob capacitors are hold in parallel to the resistor chain via tailored threaded brass rods screwed into the capacitor drills and fastened onto the mounting plates. The rods itself are stabilized with PTFE feed-throughs and further cap nuts for tightening with subsequent manufactured drill through. Additionally, they are insulated with shrinking tube on the disclosed areas. The connection of the capacitive chain with the resistor chain is realized by copper wires. These are clamped in the brass feed-throughs and between the PTFE feed-through and the cap nuts via identical soldering eyelets as appropriated for the precision resistor fixation.

In storey 3, the entire LV side setup, except for the variable air capacitors, is located. On the one hand, it includes the 2 MΩ and 1 MΩ USF-340 precision resistors and the K15Y-1-6 labelled HV doorknob capacitor realizing the default M_{94}-scale factor impedance. On the other hand, it includes the switchable impedances consisting of the 0.2 MΩ and 0.1 MΩ USF-340 precision resistors and ERO (Vishay-Rödenstein) KP-1832 capacitors. They are interconnected via the toggle switches to implement the M_{1027}- and M_{1961}-scale factors. The KP-1832 capacitors are paired by two through purpose-built stainless steel connectors. The axial wires are inserted into silver tubes which are in turn clamped inside the body of the connector. The two-pair structures are installed perpendicularly between the lowest two mounting plates fastened in brass feed-throughs. The voltage tap-off leading to the measurement tap connection is situated at the brass clamp adapter also interconnecting the permanent LV side K15Y-1-6 HV capacitor.

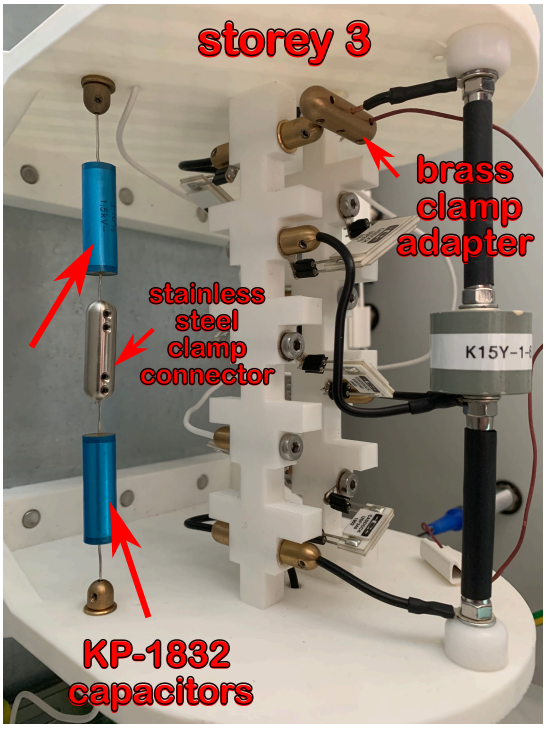

Figure 5.4: Close-up view of storey 3 of the fast precision HV divider. It shows the implemented LV side impedances of the setup with brass clamp adapter interconnecting the permanent LV side resistance and the K15Y-1 capacitor as well as the switchable impedances such as the USF-340 resistors and the ERO (Vishay-Rödenstein) type KP-1832 capacitors. The latter are perpendicularly connected via purpose-built stainless steel clamp connectors located on both sides of the resistor chain holding structure.

5.1.3. Measurement tap connection

The measurement tap connection is realized by a coaxial push-pull Series S external adapter element [Lem20] (see Figure 5.5a) manufactured by LEMO. These are analogous to the adapters implemented into the tap flange of the G35 HV divider shown in Figure 2.16a. Inside the enclosure, the adapter is interconnected with a counterpart push-pull Series S connector element [Lem20] (see Figure 5.5b). It is wired to the brass clamp

(a) Front view of the external adapter element to be fixed at the enclosure through hole for outer measurement cable connection.

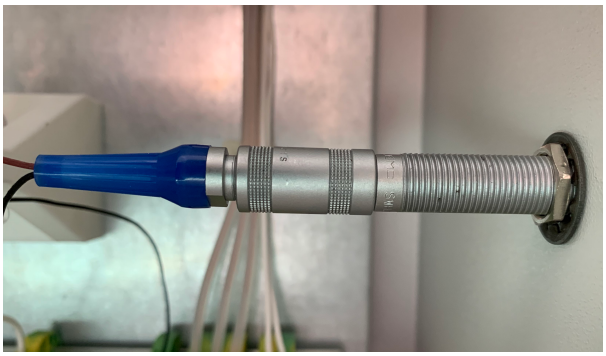

(b) Side view of the tap-off connector realization. It consists of the external adapter element and the internal push-pull connector.

Figure 5.5.: Implemented voltage tap-off connector consisting of an internal LEMO push-pull Series S connector (a) and an appropriate external LEMO adapter element (b). This allows the outer connection to the tap-off of the divider via push-pull Series S LEMO adapted coaxial cables.

adapter and to the divider grounding (see Subsection 5.1.5). In addition, the cable routing to the voltage tap-off is guided by retainers stuck at the lower mounting plate. The connector shielding is likewise grounded via the enclosure steel sheet. The external threaded adapter element is fixed at the through hole by means of a corresponding nut and a tightened toothed washer. Thus, it ensures electrical contact through the enclosure powder-coating.

The internal push-pull connector with its wiring was assembled in-house. Therefore, the transition resistance between the two leads of the connector setup has been examined to exclude manufacture defects. Using the GMC Metriso 5000 A/AK at a test voltage of 100 V, the transition resistance was determined to $> 1\,\mathrm{T}\Omega$. Hence, the application of the connector does not disturb the overall resistance implemented on LV side.

5.1.4. Variable air capacitors & toggle switch integration

To facilitate the mechanical attachment of the variable air capacitors, the mounting plate was handed over once more to the in-house workshop for 3 mm in diameter bore operations. The capacitor cases were supplemented with holed steel angles. This way, these could be fastened via screws onto the mounting plate with convenient space to the enclosure wall to add the tuning control (see Figure 5.6).

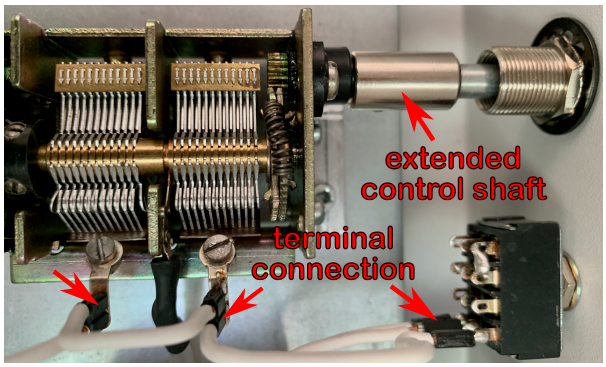

Figure 5.6: Mechanical implementation of the capacitance tuning control with extended control shaft, threaded shaft feed-through (top) as well as one of the toggle switches (bottom).

The tuning control consists of an extended shaft, fastened on the control shaft of the capacitor, together with the threaded shaft feed-through. It is tightened with a toothed washer at the respective enclosure hole. Thus, the mounting plate bores had to be precisely positioned with millimeter accuracy to fit these holes. To allow more flexibility to the extended shaft, a flexible extension was taken into account. Though, this idea was rejected preliminary due to the lack of space. The toggle switches are fixed each in-between the tuning controls in equal distance. They are connected to the divider setup via wires fixed in solder terminals soldered at the electrical contacts of the switching device. The electrical contacting of the variable air capacitors was made possible via wires fastened similarly to the precision resistors. Tight screwed soldering eyelets with sockets at the solder pads of the stator were used instead of directly soldering onto the eyelets in order to avoid damaging the capacitor plates. The stators are connected via stealthed copper cables which are shorted with the divider grounding.

On the outside of the enclosure, the extended control shafts are equipped with tuning knobs. Therefore, the extended shafts had to be shortened to fit the knob attachment properly. Lastly, any part of the control unit was labelled regarding its functionality as well as the measurement tap connection as shown in Figure 5.7. This should increase the ease of use during measurement preparation.

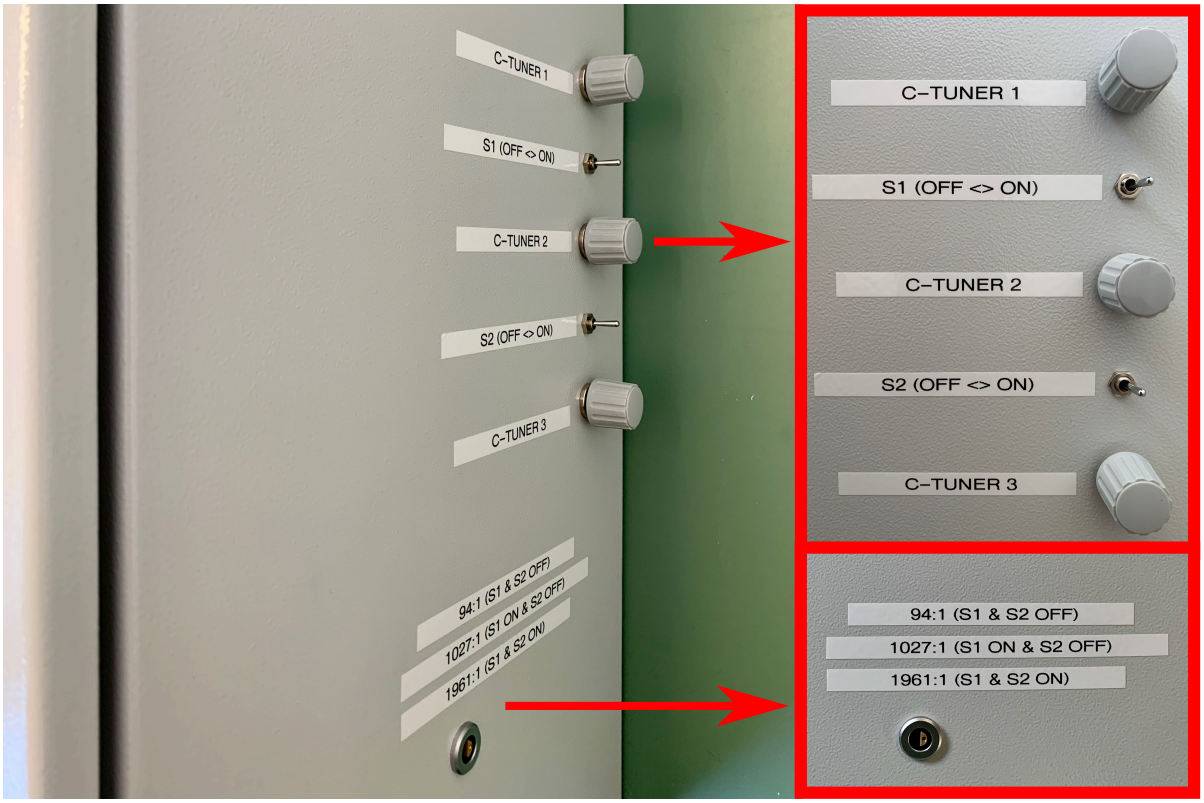

Figure 5.7.: Exterior side view of the post-customized Rittal AE 1037.500 enclosure with labelled control unit (top). It includes the capacitance tuning control and the toggle switches along with the measurement tap implementation (bottom) providing three different scale factors depending on the toggle switch setting.

5.1.5. Grounding

The grounding of the inner divider setup is implemented via an UT 2,5 RD - 3045062 feed-through terminal block [Pho20] fabricated by Phoenix Contact. It is attached to the mounting plate through the studs at the enclosure bottom. The individual terminals interconnect the different components of the divider as sketched in Figure 5.8. In practice, the wires are guided into the entry funnel of the terminals and clamped via screw connection as shown in Figure 5.9a. The terminal block is in turn connected to the enclosure grounding realized by a threaded copper rod that is mounted on the enclosure steel sheet. It is further connected to the enclosure door via copper cables of 8 mm thickness (see Figure 5.9b). Consequently, the components of the interior are star-type grounded.

This prevents the divider system from ground loops. A prefabricated and coverable hole in the bottom of the enclosure furthermore provides the opportunity for ground cable routing from a global earth to the enclosure grounding.

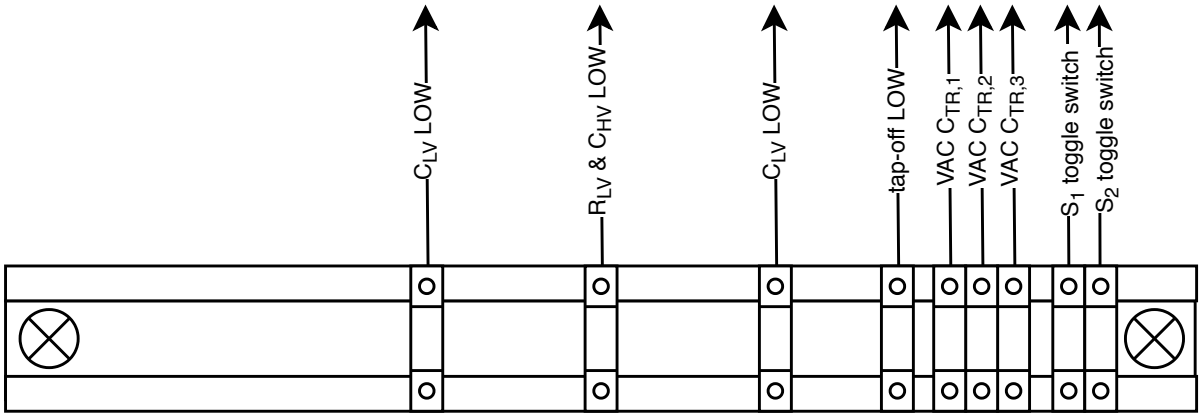

Figure 5.8.: Sketch of the UT 2,5 RD - 3045062 feed-through terminal block. It realizes the inner divider grounding with connections to the toggle switches, the variable air capacitors (VAC), the measurement tap connection and the divider chain ground nodes (LV side resistors and capacitors).

(a) Close-up view of a terminal block segment **(b)** Star-type grounding point

Figure 5.9.: Installation of the UT 2,5 RD - 3045062 feed-through terminal block. It interconnects the separate divider components as illustrated in Figure 5.8. The block is furthermore connected to the enclosure grounding point to ensure star-type grounding of the internal divider system.

5.2. Impedance characterization

In the first instance after assembly, the functionality of the outer control unit, has been tested. In particular, the total impedance change on LV side through altering the toggle switch settings of S_1 and S_2 was examined. For this, the total LV side resistance $R_{\mathrm{LV}}^{\mathrm{tot.}}$ and

capacitance $C^{\text{tot.}}_{\text{LV,min/max}}$ with minimum and maximum capacitance, reachable utilizing the variable air capacitors, were measured. Each measurement took place over a certain amount of time while altering the state of the toggle switches successively. Thereby, one of the available Keysight 34465A DMMs, programmed for 2-terminal resistance respectively capacitance acquisition in AUTO range mode with 10 PLC, was utilized. The device was connected to the measurement tap of the divider. Therefore, a dedicated push-pull Series S LEMO adapted coaxial measurement cable of about 1 m and an appropriate custom shielded banana plug adapter (shown in Figure 5.10) were used. Hence, parallel disturbance capacitances and resistances of the DMM and the measurement cable are added to the measured LV side impedance. This prepares for the intended experimental setup at GSI.

Figure 5.10: Custom banana plug to LEMO Series S adapter with shielding utilized for DMM measurements.

Over a period of about 3 min, the resistance respectively capacitances were measured. At about 55 s, toggle switch S_1 was activated and followed by toggle switch S_2 at about 110 s. The results at any valid state of the toggle switches are listed in Table 5.1. It shows the means of each impedance measurement for the different toggle switch settings. From that, an estimated characteristic time constant range $[\tau^{\text{est.}}_{\text{LV,min}}, \tau^{\text{est.}}_{\text{LV,max}}]$ can be derived.

Table 5.1.: Results of the various LV side impedance measurements with minimum and maximum tuning capacitance and the estimated τ-ranges reachable via capacitance tuning.

toggle switch ON	-	S_1	$S_1 \wedge S_2$
$R^{\text{tot.}}_{\text{LV}}$ in kΩ	1500.09(3)	136.382(5)	71.435(4)
$C^{\text{tot.}}_{\text{LV,min}}$ in nF	0.401(9)	9.597(8)	18.15(1)
$C^{\text{tot.}}_{\text{LV,max}}$ in nF	0.950(9)	10.793(8)	19.59(1)
$\tau^{\text{est.}}_{\text{LV,min}}$ in ms	0.600	1.309	1.279
$\tau^{\text{est.}}_{\text{LV,max}}$ in ms	1.425	1.472	1.399

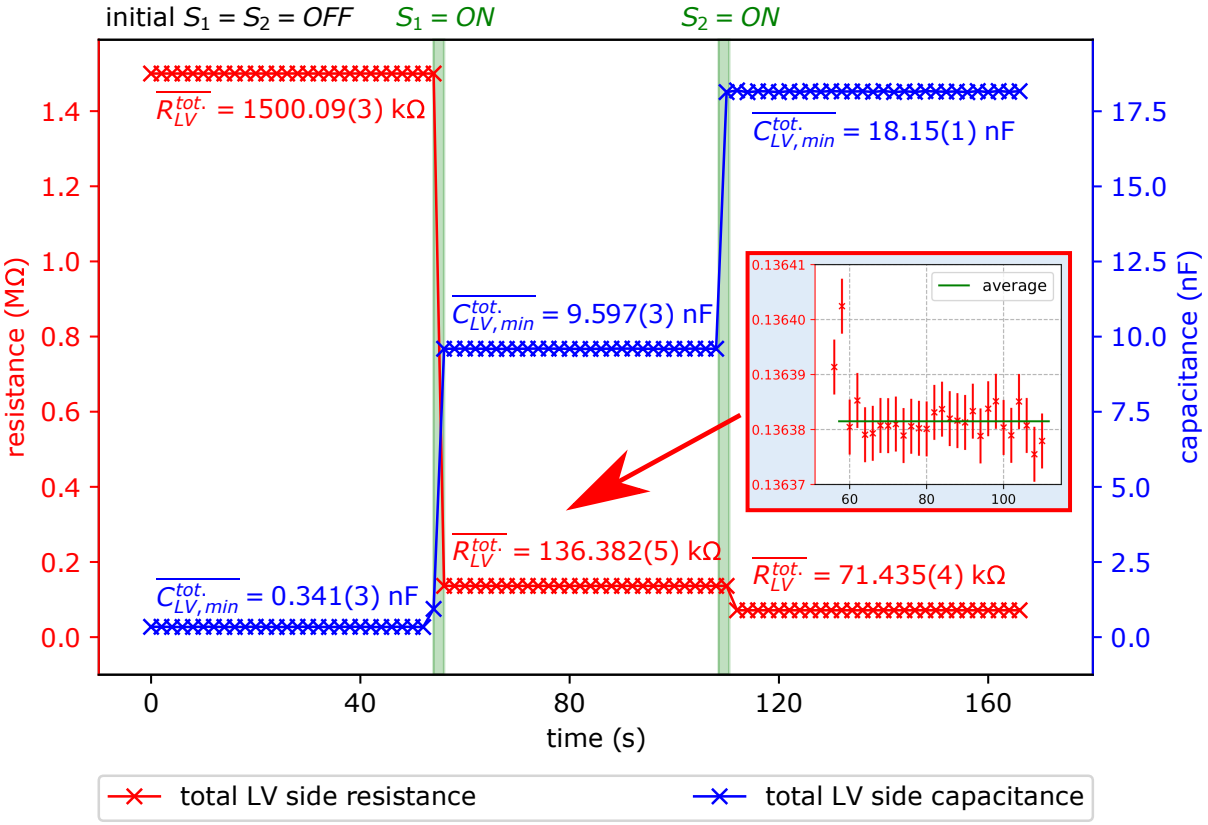

Figure 5.11.: Measured total LV side resistance $R^{\text{tot.}}_{\text{LV}}$ and minimum capacitance $C^{\text{tot.}}_{\text{LV,min}}$ over a measurement period of about 3 min each. The total impedance on LV side was altered via switching S_1 and S_2 with the effects formerly discussed.

The results of $R^{\text{tot.}}_{\text{LV}}$ and $C^{\text{tot.}}_{\text{LV,min}}$ with respect to the acquisition time are illustrated in Figure 5.11. Consequently, the measurements demonstrate the proper functionality of the scale factor and time constant variation of the divider system. As expected, the difference between the overall minimum and maximum capacitance lies in the order of about 600 pF times the amount of switched variable air capacitors. To evaluate the opportunity to align the time constants of the entire system, the HV side impedance was investigated as well. Hence, the HV side resistance R_{HV} and capacitance C_{HV} were measured using the Aim-TTi LCR 400 with its external 4-terminal test fixture connection to exclude unintended disturbances induced by the LCR bridge probe. The test frequency was set to 100 Hz. The device was readout over RS-232[5] serial interface. The fixture was fastened directly at the ohmic divider chain located between storey 1 and 2. The measurement period was chosen to be about 60 s with the results being

$$\begin{aligned} R_{\text{HV}} &= 140.018(3)\,\text{MΩ} \\ C_{\text{HV}} &= 8.9(3)\,\text{pF} \end{aligned} \tag{5.1}$$

by which the characteristic time constant of the HV side impedance can be estimated.

[5] Recommended Standard 232; standard for serial communication transmission of data

Subsequently, this leads to the following approximation:

$$\tau_{\mathrm{HV}} = R_{\mathrm{HV}} C_{\mathrm{HV}} \approx 1218\,\mathrm{M\Omega pF} = 1.218\,\mathrm{ms}. \tag{5.2}$$

Based on the results presented in Table 5.1, complete frequency compensation should be possible for the M_{94}-scale factor setting. The determined τ-range includes the measured time constant which characterizes the divider impedance on HV side. In case of the M_{1027}- and M_{1961}-setting, τ_{HV} deviates about 5 % from the reachable τ-range since the installed LV side capacitances surpass the design expectations. To what extent these deviations influence the emerging transient response behaviour and if further divider modifications are required, will be investigated in the following. Furthermore, the DC scale factors can be estimated via

$$M_i^{\mathrm{DC,est.}} = R_{\mathrm{HV}} / R_{\mathrm{LV}}^{\mathrm{tot.}} + 1. \tag{5.3}$$

The results are listed in Table 5.2 for any of the three scale factor settings M_i provided by the measurement tap.

Table 5.2.: Estimated DC scale factors $M_i^{\mathrm{DC,est.}}$ of the novel fast precision HV divider based on performed resistance measurements. The values were derived by use of Equation 5.3.

	toggle switch ON	DC scale factor $M_i^{\mathrm{DC,est.}}$
M_{94}	-	94.3397(77) : 1
M_{1027}	S_1	1027.66(12) : 1
M_{1961}	$S_1 \wedge S_2$	1961.07(30) : 1

5.3. 10 V pulse transmission tests

As part of the commissioning of the HV divider system, the very first investigation of its step voltage transmission was conducted with the following experimental setup (sketched in Figure 5.12):

- a Tektronix AFG3102 **arbitrary/function generator** providing 1 mHz to 50 MHz arbitrary waveform generation with 20 $\mathrm{mV_{p\text{-}p}}$ to 10 $\mathrm{V_{p\text{-}p}}$ amplitude into 50 Ω and 100 MHz noise bandwidth (−3 dB) [Tek20a]
- an Agilent InfiniiVision DSO-X 2024A **200 MHz oscilloscope** characterized with $R_{\mathrm{OSC}} = 1\,\mathrm{M\Omega} \pm 2\,\%$ in parallel with $C_{\mathrm{OSC}} = 11\,\mathrm{pF}$ input impedance [Key20b]

The arbitrary/function generator and the 200 MHz oscilloscope were both controlled remotely over USB and programmed with instructions retrieved from [Tek20b] and [Key20b]. The signal output of the arbitrary/function generator was completed with 50 Ω and connected to the HV divider input connection via a dedicated banana plug to

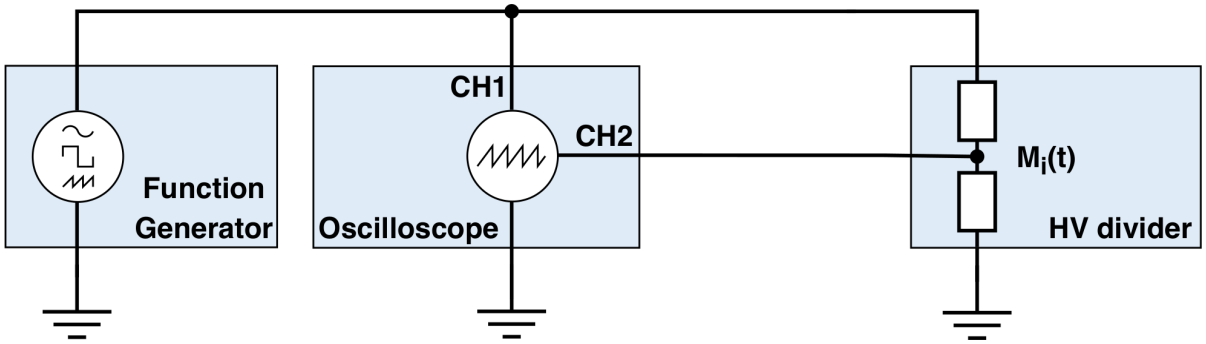

Figure 5.12.: Sketched experimental setup visualizing the signal transmission of the novel fast precision HV divider. The input signal was generated by means of a Tektronix AFG3102 arbitrary/function generator and acquired along with the corresponding divider output. For acquisition an Agilent InfiniiVision DSO-X 2024A 200 MHz oscilloscope was utilized.

HVS65 (male) plug connector. Furthermore, it was connected to input channel 1 (CH1) of the oscilloscope via BNC coaxial cable. Moreover, the measurement tap of the HV divider was connected to channel 2 (CH2) through a 5 m push-pull Series S LEMO adapted coaxial cable and a purpose-built LEMO Series S to BNC connector. The chosen cable length serves to compensate the low capacitance of the oscilloscope in comparison to the DMM appropriated for precision measurements in the final setup. All devices including the HV divider were grounded to the same global earth in order to avoid unintended noise caused by ground loops.

The input signal was programmed to be intermittent rectangular voltage pulses of 10 ms length (at 50 % duty cycle) and 10 V amplitude with 5 ns leading and trailing. Utilizing the Agilent InfiniiVision DSO-X 2024A 200 MHz oscilloscope, both input and output voltages were acquired simultaneously via dual-channel data acquisition.

In Figure 5.13, the measurement of the M_{94}-scale factor transient at minimum tuning capacitance $C_{\mathrm{TR},1}$ is visualized. Because of the input impedance of the oscilloscope connected in parallel to the LV side impedance of the divider system, the overall DC scale factor changes to

$$M^{\mathrm{DC}}_{94+\mathrm{OSC}} = M^{\mathrm{DC}}_{94} + R_{\mathrm{HV}}/R_{\mathrm{OSC}}. \tag{5.4}$$

To manually reduce the observed undercompensation (compare Section 3.2), the LV side capacitance was tuned via C-Tuner 1 control. The resulting optimized output signal is depicted in Figure 5.14 (blue). As is evident, an ideal all-pass condition cannot be reached since the high frequent components dominate the transient response despite manual tuning aiming for frequency compensation. Consequently, this reveals an initial transient characteristic that may emerge from residual stray capacitances, i.e. underlying systematic disturbances of higher order within the divider setup. How far the characteristic transient influences the transient response behaviour on ppm-scale, cannot be answered. That is because the precision obtained from the Agilent InfiniiVision DSO-X 2024A 200 MHz oscilloscope does not meet the required scope.

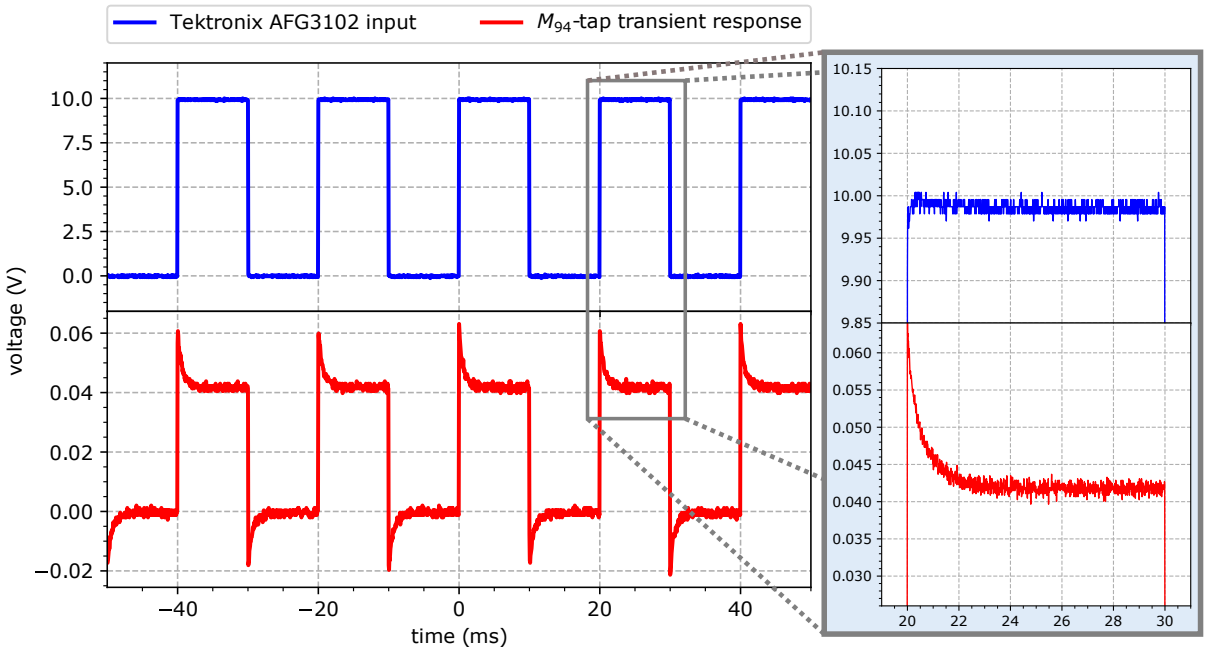

Figure 5.13.: Agilent InfiniiVision DSO-X 2024A dual-channel acquisition of the intermittent 10 V rectangular pulse input produced by the Tektronix AFG3102 arbitrary/function generator (blue) and the corresponding output transient signal stem from the novel fast precision HV divider at $M = M_{94}$ with minimum tuning capacitance $C_{\mathrm{TR},1}$ (red).

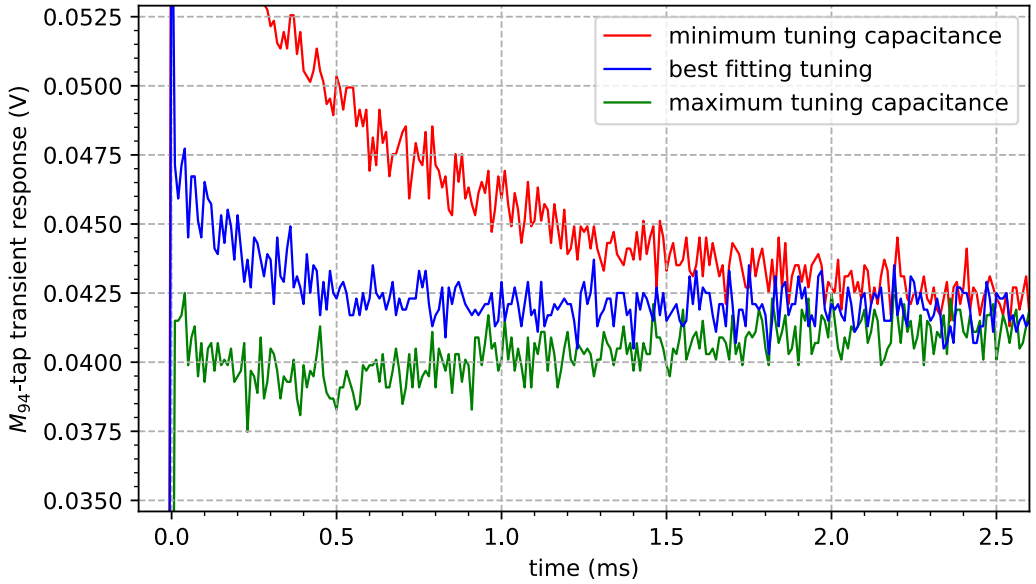

Figure 5.14.: Agilent InfiniiVision DSO-X 2024A single-channel acquisition of a transmitted 10 ms rectangular pulse at $M = M_{94}$ adjusted via capacitance tuning of $C_{\mathrm{TR},1}$ in a close-up view for various tuning settings.

Identical measurements were conducted for the M_{1027}- and M_{1961}-setting confirming the functionality of the signal transmission (see Figure 5.15). Unlike the M_{94}-tap measurement, no transient response behaviour, affecting the shape of the transmitted step voltage input, could be observed. This is due to the low voltage input of 10 V amplitude which causes too low SNR at the output. In response to the aforementioned systematic measurement problems, further calibrations will be performed using a more advanced experimental setup which includes an HV input source and high-precision DMMs. This will be outlined in the subsequent Section 5.4.

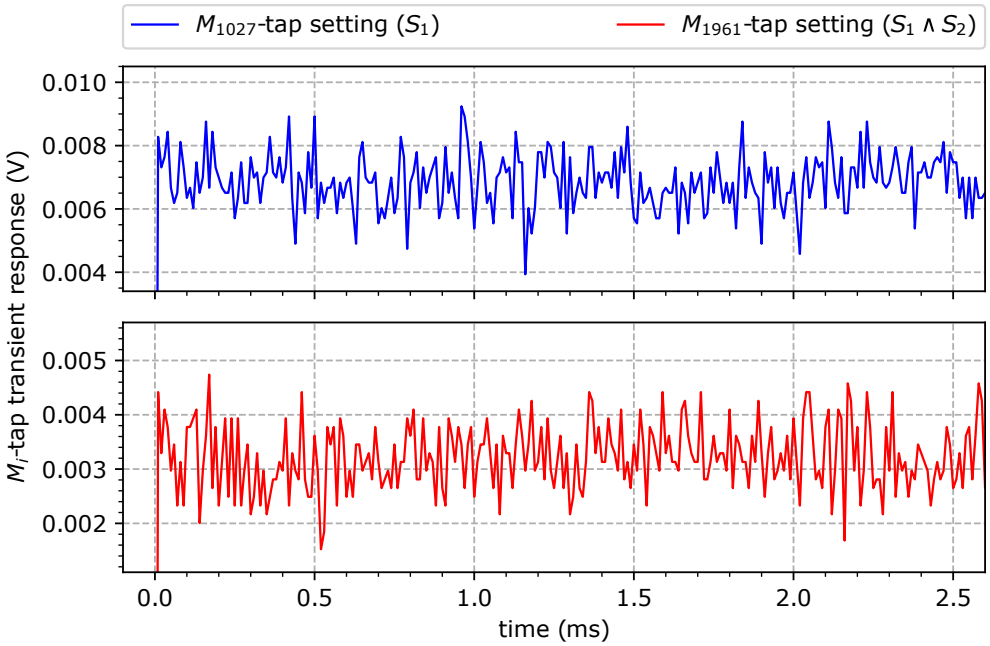

Figure 5.15.: Agilent InfiniiVision DSO-X 2024A single-channel acquisition of the transmitted 10 ms rectangular pulses at $M = M_{1027}$ (blue) and $M = M_{1961}$ (red). Due to the oscilloscope in parallel connection, the DC scale factor of the divider output changes to $M^{\mathrm{DC}}_{i+\mathrm{OSC}} = M^{\mathrm{DC}}_i + R_{\mathrm{HV}}/R_{\mathrm{OSC}}$.

5.4. Calibration with HV power supply

In order to validate the proper functionality of the novel fast precision HV divider for usage in DR experiments at CRYRING@ESR, it has been characterized regarding its target features. These consider capacitance tuning for frequency compensation and the consequent transient response behaviour. Thus, an experimental setup with amplified HV input up to 1 kV for SNR reduction was established in order to calibrate the time-dependency of the three scale factor settings $M_i(t)$. A similar HV amplification setup is used at CRYRING@ESR, so that the influence of voltage ramping on the divider transmission can be investigated as well. The subsequent measurements were performed in the HV laboratory with all data acquired by use of a Keysight 34465A DMM. It provides opportunities for high-precision voltage measurements in short time intervals which is

indispensable for investigating the divider transient response behaviour in a range of 10 ms with high accuracy. An overview of the available NPLC operation modes provided by the Keysight 34465A DMM is listed in Table 5.3. The programming and readout was done remotely over USB via `PyVISA` [Mat20]. This Python package implements the VISA standard API, using the SCPI[6] programming language. Specific programming instructions are retrieved from [Key20c].

Table 5.3.: NPLC operation modes of the Keysight 34465A DMM with respect to the measurement precision in digits and readings per second with A-Zero mode enabled. For integration times greater than 1 PLC the DMM averages the number of readings made, using 1 PLC of integration time [Key20c].

NPLC	integration time	digits	readings/sec
0.0001	20 µs	4.5	50000
0.002	40 µs	5	25000
0.006	100 µs	5	10000
0.02	300 µs	6	3333
0.06	1 ms	6	1000
0.2	3 ms	6.5	333
1	20 ms	6.5	50
10	200 ms	6.5	5
100	2 s	6.5	0.5

5.4.1. The Kepco Bop 1000m amplifier

The ramp of the electron cooler voltage, which introduces relative electron-ion energies in DR experiments at CRYRING@ESR, will be realized using a fast HV amplifier with a voltage range of ±2 kV [A+15]. A similar in-house Kepco Bop 1000m HV bipolar power supply [Kep11] (depicted in Figure 5.16), with a voltage range of ±1 kV and 12 µs/V

Figure 5.16: Front panel view of the Kepco Bop 1000m HV bipolar power supply appropriated to examine the transmission behaviour of the divider setup [Kep20].

[6] Standard Commands for Programmable Instruments; standard for syntax and commands to use in controlling programmable test and measurement devices.

slew rate, was used as an AC amplifier to characterize the transmission behaviour in an HV input test setup. The device is able to amplify a variety of waveshapes. These include step functions from external voltage sources intended to simulate electron cooler HV ramps. To disclose possible characteristics in amplifying external AC input voltage signals, the Kepco Bop 1000m has been characterized regarding its transfer function $|H(f)|$ in frequency domain beforehand. This serves the purpose to evaluate the grade of high frequent step voltage amplification in short time intervals, as conducted for the subsequent calibration measurements. Thereby, the amplified amplitude $U_{\alpha_K}(f)$ of a sinusoidal input $u_\alpha(t) = U_\alpha \cdot \sin(2\pi f t)$, generated by an external AC input source with amplitude U_α, has been measured[7] for various frequencies $f = \frac{\omega}{2\pi}$ on a logarithmic scale. Consequently, the AC amplification

$$\frac{U_{\alpha_K}(f)}{U_\alpha} = |H(f)| \tag{5.5}$$

serves to approximate the transfer function of the HV amplifier as plotted in Figure 5.17.

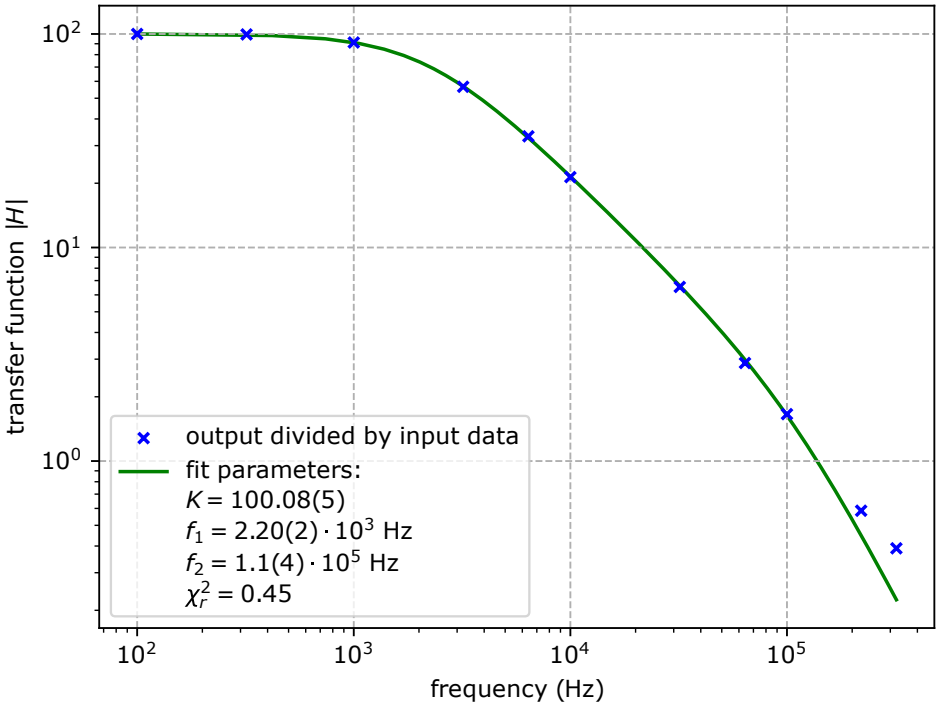

Figure 5.17.: Measurement data of the acquired relative AC amplification $U_{\alpha_K}(f)/U_\alpha$ (blue) of the Kepco Bop 1000m HV amplification at various input frequencies f. The data was fitted (green line) via the second-order low-pass filter transfer function derived from Equation 5.6 with the resulting fit parameters shown.

[7] These measurements were not conducted as part of this work, but formerly by O. Rest back in 2014. Hence, no detailed descriptions concerning the exact experimental setup nor its error estimations can be given.

The Kepco Bop 1000m amplifier can be approximated as second-order low-pass filter with absolute transfer function

$$|H(f)| = \frac{K}{\sqrt{(1+f^2/f_1^2)(1+f^2/f_2^2)}} \tag{5.6}$$

as a Laplace representation. K denotes the gain and $f_{1,2} \overset{1)}{=} (2\pi\tau_{1,2})^{-1}$ are the cut-off frequencies in dependence of the characteristic time constants $\tau_{1,2}$ of the second-order system. A fit of the transfer function on the data reveals the two cut-off frequencies with $-20\,\mathrm{dB/octave}$ attenuation at $f_1 = 2.2\,\mathrm{kHz}$ and $-40\,\mathrm{dB/octave}$ attenuation at $f_2 = 0.1\,\mathrm{MHz}$ from the gain $K = 100$. In Laplace representation, a fast voltage ramp can be approximated by the general step function U/s with complex frequency $s = i\omega = i2\pi f$ and amplitude U. Inverse Laplace transforming the product of the transfer function $H(s)$ with $|H(s)| = |H(f)|$ and the general step function leads to the expected amplified output function of the Kepco Bop 1000m evolving over time t as

$$\begin{aligned}
\mathcal{L}_s^{-1}\left[H(s)\times\frac{U}{s}\right](t) &= \mathcal{L}_s^{-1}\left[\frac{K}{(1+s^2\tau_1^2)(1+s^2\tau_2^2)}\times\frac{U}{s}\right](t) \\
&= U_K\left(1-\frac{\tau_1}{\tau_1-\tau_2}e^{-t/\tau_1}+\frac{\tau_2}{\tau_1-\tau_2}e^{-t/\tau_2}\right)+U_K^{\text{offs.}} \\
&\overset{1)}{=} U_K\left(1-\frac{f_2}{f_2-f_1}e^{-2\pi f_1 t}+\frac{f_1}{f_1-f_2}e^{-2\pi f_2 t}\right)+U_K^{\text{offs.}}
\end{aligned} \tag{5.7}$$

with amplitude $U_K = U \cdot K$ and an amplitude offset $U_K^{\text{offs.}}$.

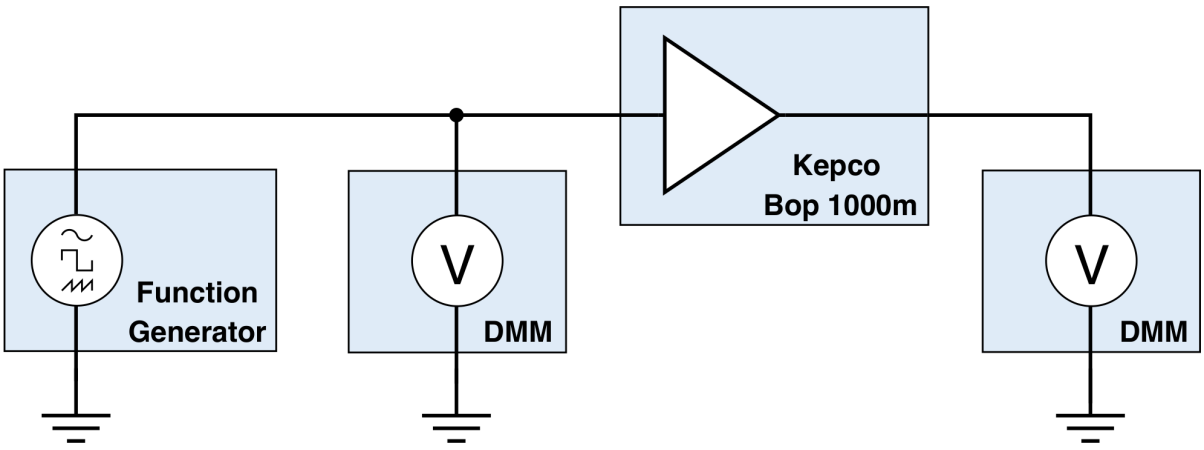

Figure 5.18.: Sketched experimental setup to examine the step voltage amplification of the Kepco Bop 1000m amplifier. The Tektronix AFG3102 arbitrary/-function generator produces a rectangular pulse signal of amplitude U which is measured for before and after amplification via two Keysight 34465A DMMs.

In order to validate the expected outcome in comparison to the real amplification behaviour, the experimental setup was used as follows (also see Figure 5.18):

- the Tektronix AFG3102 **arbitrary/function generator** as external step voltage input source producing a $U = 5\,\mathrm{V}$ rectangular pulse of 15 ms length with 5 ns leading and trailing. The programming was similar to the 10 V pulse transmission tests outlined in Section 5.3
- two Keysight 34465A **6.5-digit digital multimeters** with 0.02 PLC and 10 V (before amp.) respectively 1000 V (after amp.) voltage operation range in DCV mode with A-Zero off

The arbitrary/function generator was connected with 50 Ω termination to the voltage programming input of the HV power supply via BNC to banana plug adapter and moreover to one of the Keysight 34465A devices. Further, the Bop output was connected to the input terminals of the second DMM with shortened common and ground. The 5 V rectangular pulse along with the resulting amplified output were measured simultaneously by means of the precision DMMs. The measurement data is shown in Figure 5.19. The expected time evolution of the amplified output has been fitted on the output data with fixed cut-off frequencies $f_{1,2}$ (compare Figure 5.17) with the resulting fit function (green line).

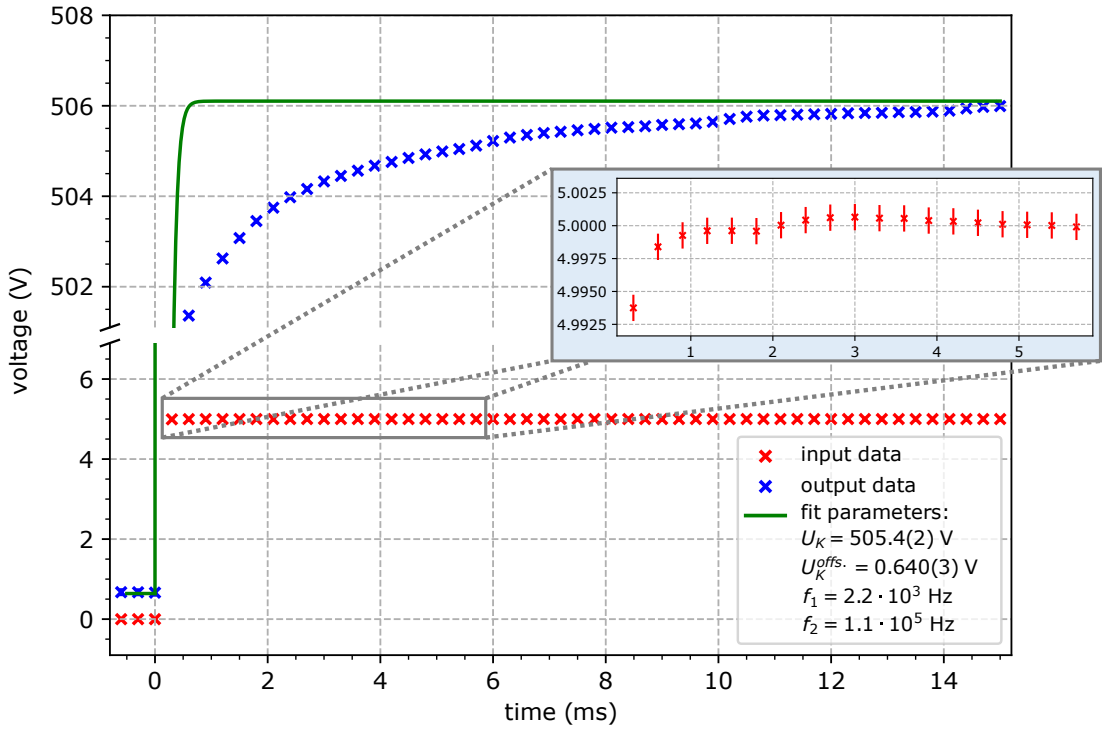

Figure 5.19.: Measurement data of the acquired 5 V step voltage input produced by the Tektronix AFG3102 arbitrary/function generator (red). A close-up view of the voltage load in the first 5 ms and the resulting amplified output signal originating from the Kepco Bop 1000m amplifier is shown (blue). The latter was fitted (green line) via Equation 5.7 at fixed cut-off frequencies $f_{1,2}$ obtained from Figure 5.17 with the resulting parameters shown.

As the fit implies, an accurate prediction of the amplification behaviour cannot be conducted when approximating the HV amplifier as second-order low-pass filter with cut-off frequencies $f_{1,2}$. The amplified output suffers from a significant voltage load when transmitting a stable input step function. Therefore, the amplified Kepco Bop 1000m output has a non-negligible impact on the measurement of the transient response behaviour. Its characteristic loading behaviour reshapes the output signal originating from the divider setup. Based on this knowledge, a measurement technique has been developed in order to calibrate the scale factor time-dependencies $M_i(t)$ under consideration of the HV input load. A detailed description of the calibration method is given in the subsequent Subsection 5.4.2.

5.4.2. Method

The $M_i(t)$-calibrations aim to characterize the output transmission behaviour while taking into account its reproducibility as well as its long-term stability. They were conducted using the experimental setup shown in Figure 5.20 with the devices introduced in Subsection 5.4.1. The Kepco Bop output provided an amplified signal with gain $K = 100$ initiated by the Tektronix AFG3102. It was connected to the voltage programming input completed with $50\,\Omega$. The divider input $u_{in,K}(t)$ was supplied using the banana plug to HVS65 (male) plug connector. It was measured via one of the Keysight 34465A DMMs

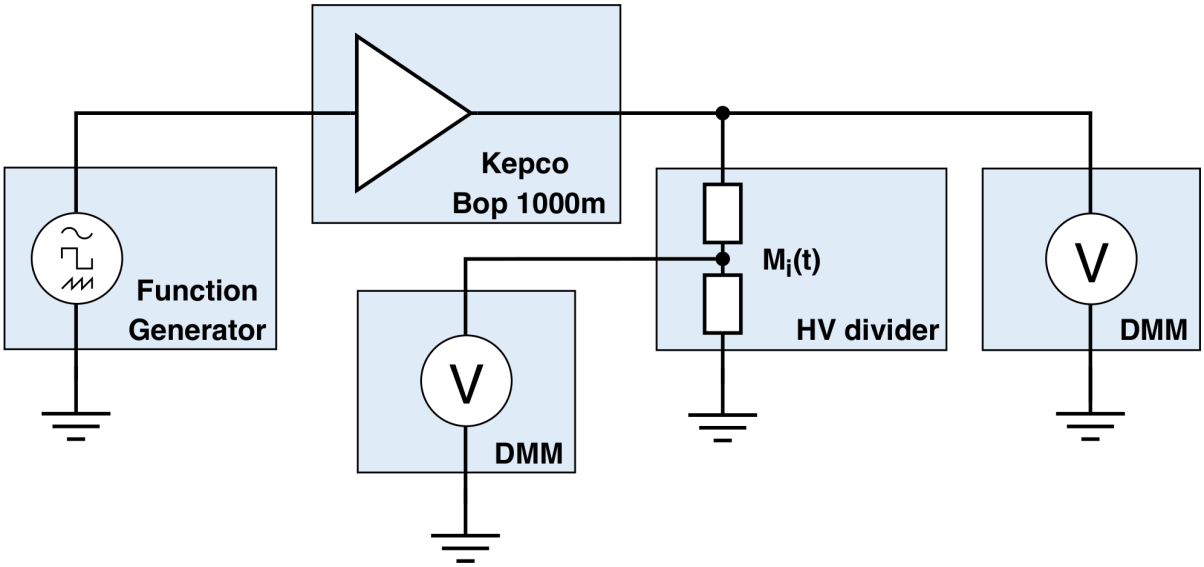

Figure 5.20.: Sketched experimental setup for HV $M_i(t)$-calibration measurements. The Tektronix AFG3102 arbitrary/function generator produces a continuous signal of periodic rectangular pulses of amplitude U subsequently amplified by the Kepco Bop 1000m HV amplifier. The amplified signal sequence is then guided to the HV divider input, where it is divided with a characteristic scale factor $M_i(t)$. Both divider input and output signal are measured simultaneously by use of high precision Keysight 34465A DMMs.

set in DCV mode with 0.02 PLC and A-Zero at 1000 V operation range. The second DMM connects the measurement tap via the push-pull Series S LEMO coaxial cable of 1 m length. The device was programmed equally except for its DCV operation range which was 10 V for M_{94} respectively 1 V for M_{1027} and M_{1961}. This allows an acquisition of the output voltages

$$u_{out,i}(t) = \frac{u_{in,K}(t)}{M_i(t)} \tag{5.8}$$

with highest precision. The Tektronix AFG3102 input sequence was chosen to be intermittent rectangular voltage pulses of 25 ms length (at 50 % duty cycle) and $U = 8\,\mathrm{V}$ amplitude with 5 ns leading and trailing. The divider enclosure was star-type grounded with all devices participating in the experimental setup to a global earth. Through measuring both, the input $u_{in,K}(t)$ and output $u_{out,i}(t)$, the transmission behaviour induced by the divider setup could be examined separately from the amplification load caused by the HV amplifier as aforementioned. Neglecting higher order terms, the transient response of the scale factors M_i can be determined (in reference to Equation 2.30) as

$$M_i(t) = \frac{u_{in,K}(t)}{u_{out,i}(t)} = \tilde{A}_i e^{-(t-t_0)/\tau_i} + M_i^{\mathrm{DC}} \tag{5.9}$$

$\tilde{A}_i$ and τ_i represent parameters that depend on the capacitance tuning setting of the divider system. $\tilde{A}_i < 0$ applies for undercompensation, $\tilde{A}_i > 0$ for overcompensation and $\tilde{A}_i = 0$, when the all-pass compensation condition is fulfilled (compare Section 3.1 and 3.2). τ_i stands for the time constant of the uncompensated divider transient response while M_i^{DC} represents the DC scale factor of the divider setting.

5.4.3. All-pass tuning

In order to prepare the add-on divider for subsequent calibration measurements, its scale factor settings have been step-wise tuned regarding frequency compensation by means of the outer control unit. Meanwhile, the transient response of the corresponding scale factor $M_i(t)$ is measured for an input sequence of 1 s duration for each tuning setting and re-adjusted until minimum transient load is reached. As already worked out during the impedance characterization, the M_{1027}- and M_{1961}-transients could not be optimized properly. This required further modifications on the experimental divider setup. Hence, the switchable LV side capacitances were reduced exchanging one of the 16.5 nF KP-1832 capacitors in favor of a lower-capacity 10 nF ± 5 % TFF aluminium foil polyester capacitor manufactured by WIMA.

In Figure 5.21, the acquired divider output data together with the HV input pulse data divided by the estimated DC scale factor $M_{94}^{\mathrm{DC,est.}}$ (see Table 5.2) for the M_{94} setting are shown (top). Likewise, the resulting scale factor $M_i(t)$ measurement is depicted (bottom).

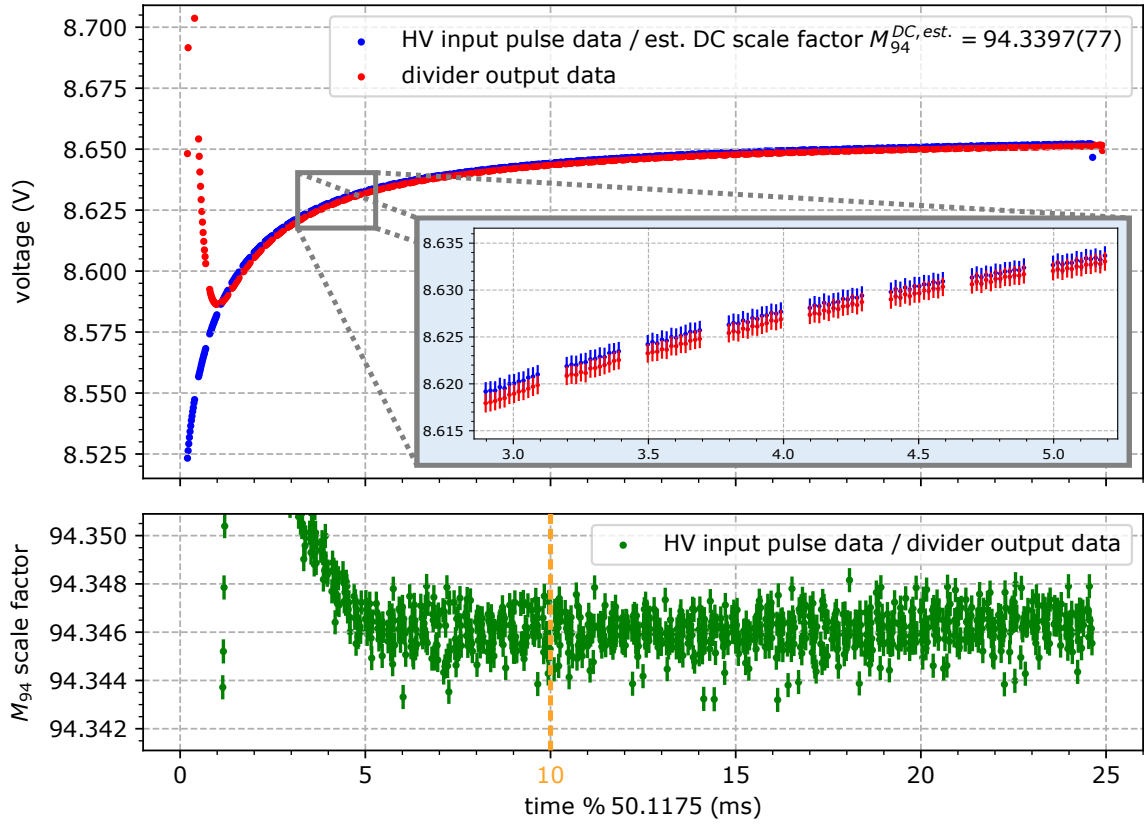

Figure 5.21.: Acquired divider output (blue) and scaled HV input pulse (red) modulo 50.1175 ms superimposed data sequence of the $M_{94}(t)$-calibration measurement. The relation between the datasets leads to the characteristic time-dependent scale factor $M_{94}(t)$ (green).

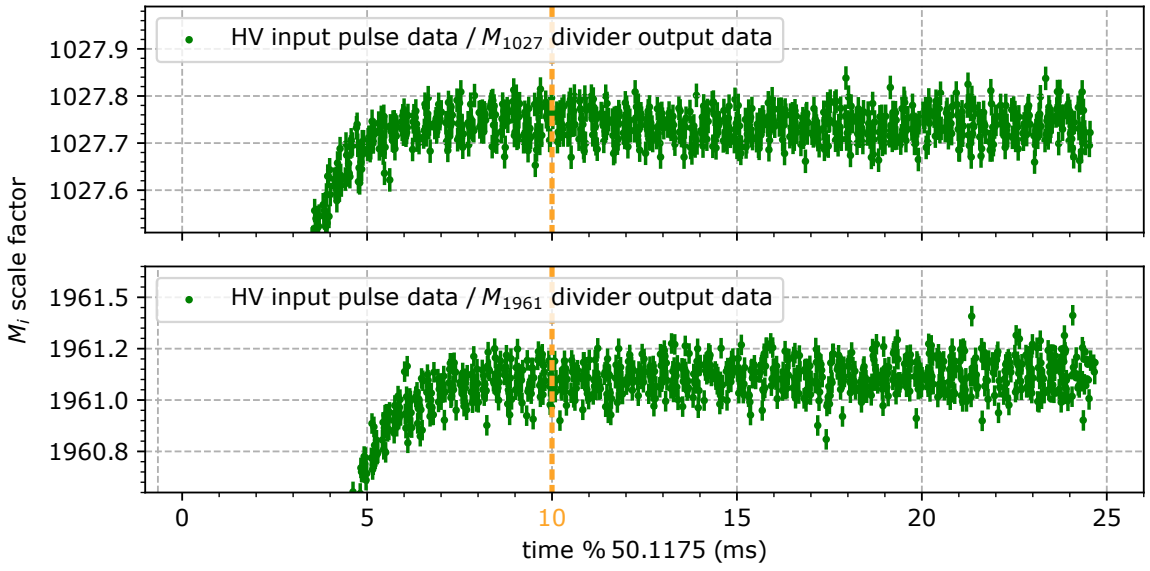

Figure 5.22.: Acquired characteristic time-dependent scale factor $M_i(t)$ modulo 50.1175 ms superimposed data sequences of the M_{1027}- (top) and M_{1961}-calibration measurements (bottom).

Furthermore, the acquisitions of the other two scale factors are plotted in Figure 5.22. The settings were tuned towards frequency compensation using C-Tuner 2 respectively C-Tuner 3. The data sequences were superimposed in time series with modulo 50.1175 ms being the input pulse generation period. For each setting, the fine-tuning was done by sense of proportion leading to the shown transients with short-lasting over- and under-compensation. Approximately, time-independency $M_i(t) \approx M_i^{\mathrm{DC}}$ could be reached after 5 to 8 ms response time.

To achieve a more accurate all-pass tuning, the setup has further been modified for test purposes. Thereby, an additional sub-pF SGNM type A3T10004 trimmer capacitance [Spr20] manufactured by Sprague-Goodman Electronics with 1 kV voltage operation range and a tuning range ($\Delta C_{\mathrm{TR,add.}}$) of 1 to 10 pF has been integrated into the divider setup. It was installed in parallel to the C-Tuner 1 device connected via solder terminals. Since there was a suggestion, that the variable air capacitors do not facilitate the necessary tuning precision, the complementing capacitance was used as a fine-tuning control on top of the present control unit. This exceeds the corresponding tuning range to

$$C'_{\mathrm{TR},1} = C_{\mathrm{TR},1} + C_{\mathrm{TR,add.}} \tag{5.10}$$

with sub-pF tuning precision. However, this modification did not lead to the desired enhancements. Prospects of further improvement based on this approach will be proposed in Chapter 6.

5.4.4. Experimental results

After tuning the HV divider system for the purpose of fast step voltage input pulse transmission, its reproducibility and accuracy was examined. At first, the DC scale factors were estimated analyzing the fit distribution of M_i^{DC} on a dataset of transient responses $M_i(t)$. These were measured over a period of 15 min for each scale factor setting leading to a measure of short-term reproducibility. A subset of the measurement data for the M_{94}-scale factor characterization is shown in Figure 5.23. The M_{94}^{DC} parameters were computed by fitting Equation 5.9 successively on a set of single transients with the resulting distribution illustrated in Figure 5.24. The measurement has been performed initially on October 17, 2020 (left) and repeated on October 19, 2020 (right) after 48 h of applied Kepco HV giving a measure of long-term reproducibility. Further, this procedure has been redone for the other two scale factor settings measured from October 19, 2020 to October 23, 2020 with the results appended in Figure A.3 (M_{1027}) and A.5 (M_{1961}).

In order to evaluate the transient $M_i(t)$ relative to DC M_i^{DC} deviation given in a certain response time interval $\Delta T_{t_1-t_2}$, the single transient means

$$\mu_i(\Delta T_{t_1-t_2}) = M_i^{\mathrm{DC}} - \mathrm{bias}_i(\Delta T_{t_1-t_2}) \tag{5.11}$$

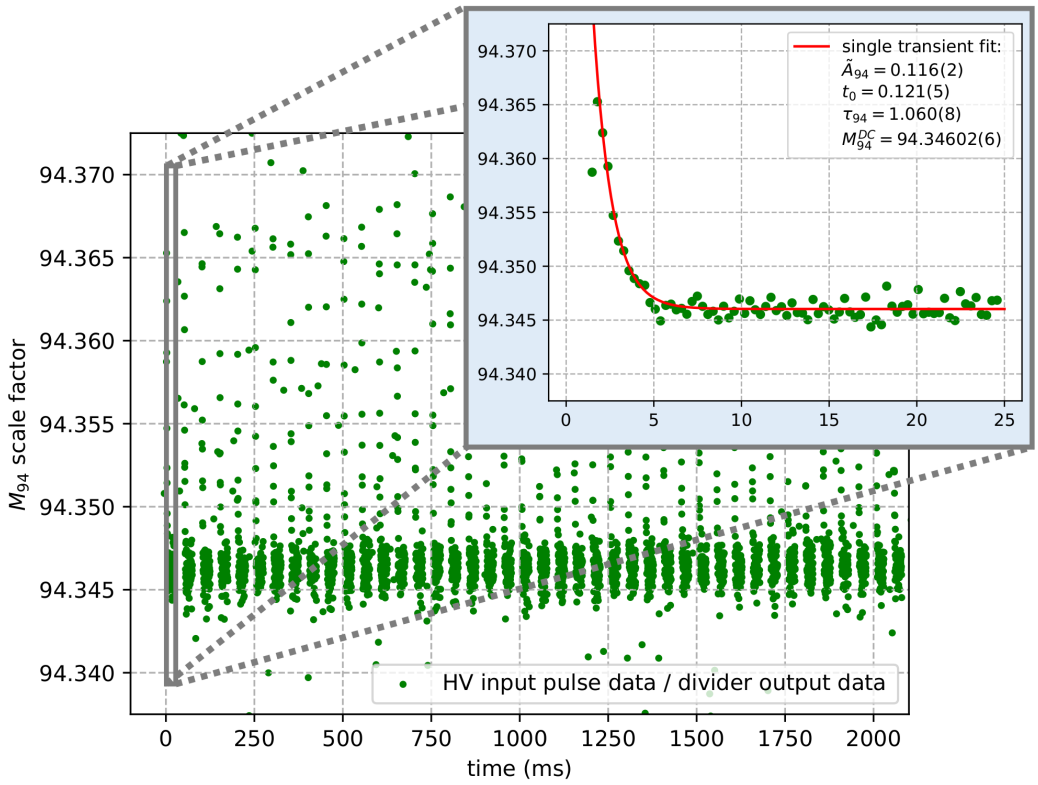

Figure 5.23.: Subset of the M_{94}-scale factor characterization measurement as a relation of the amplified HV input pulse data and divider output data acquired by the two Keysight 34465A DMMs. As illustrated in the close-up view, the single transients are fitted separately via Equation 5.9.

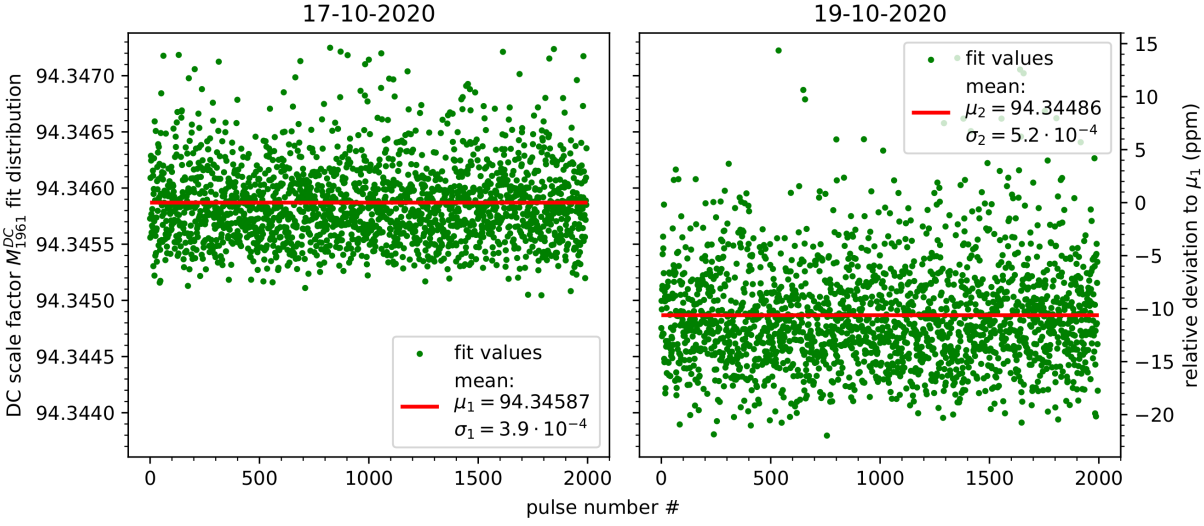

Figure 5.24.: M_{94}^{DC} fit distribution of 2000 analyzed single transient responses along with its mean $\mu_{1,2}$ and standard deviation $\sigma_{1,2}$. Besides the initial characterization measurement performed on October 17, 2020, it was repeated after 48 h on October 19, 2020 to investigate the long-term stability of the M_{94}-scale factor setting.

between various intervals $[t_1, t_2]$ were computed. It holds $t_1, t_2 > t_0 \bmod 50.1175\,\text{ms}$, whereby t_0 is the initial time of the HV divider output response. $\mu_i(\Delta T_{t_1-t_2})$ differs from the estimated DC scale factor by a correction bias which characterizes the goodness of the frequency compensation. In terms of future time slice analysis at DR experiments, it was compared for 8 to 10 ms, 8 to 15 ms and 10 to 15 ms (mod 50.1175 ms) response time intervals. All analysis took place based on the initial measurements performed to investigate the long-term reproducibility. The resulting mean distributions of the M_{94}-scale factor characterization - binned by 200 pulses - in comparison to the corresponding DC scale factor M_{94}^{DC} estimation are depicted in Figure 5.25. The initial measurement distributions of the other two scale factor settings with analogous time intervals $\Delta T_{t_1-t_2}$ are appended in Figure A.4 (M_{1027}) and A.6 (M_{1961}).

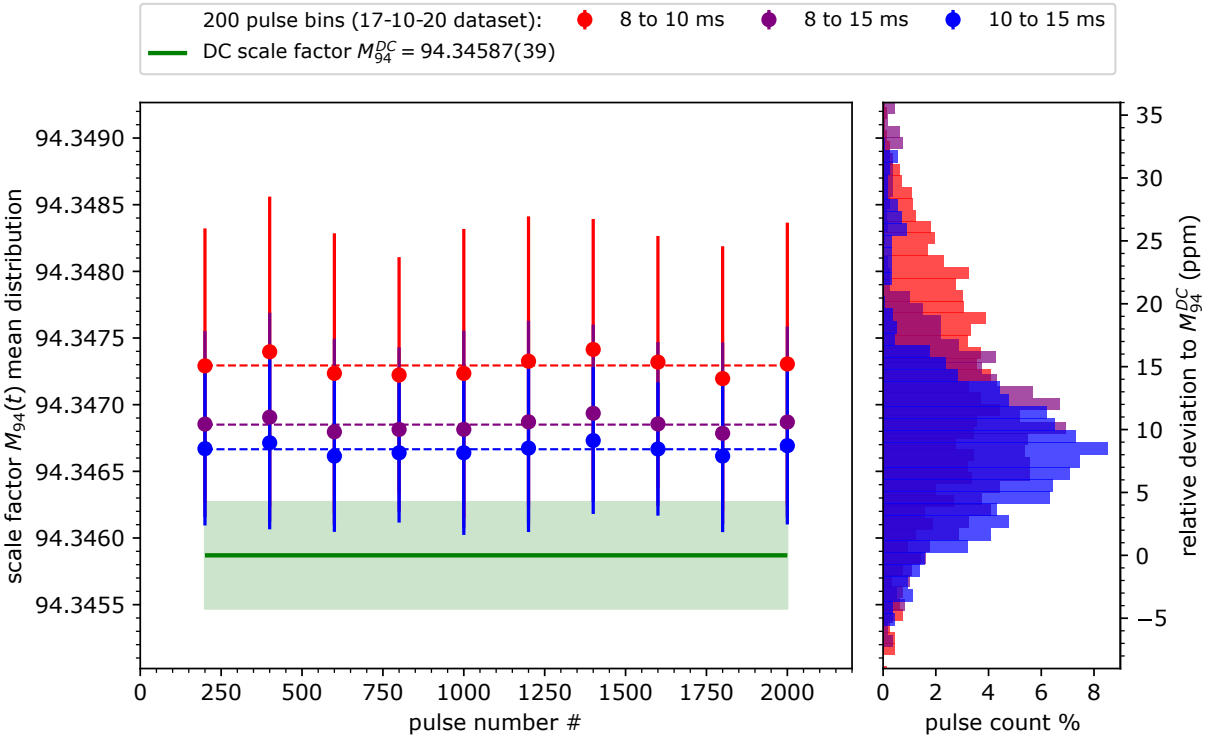

Figure 5.25.: 200 pulse binned μ_{94}-distribution for the 8 to 10 ms (red), 8 to 15 ms (purple) and 10 to 15 ms (blue) response time intervals $\Delta T_{t_1-t_2}$ compared to the DC scale factor M_{94}^{DC} (green). The latter was determined from the fit distribution illustrated in Figure 5.24 (17-10-20).

As a result, the investigations demonstrate scale factor shifts that indicate 48 h long-term stability in the order of about 4 to 10 ppm (2 to 5 ppm/d). Partially, these shifts may be caused by temperature fluctuations in the laboratory during the waiting period as well as induced by the Keysight 34465A DMMs themselves. Moreover, the DC scale factors could be determined with an accuracy of 4 to 9 ppm.

In addition, the resulting divider transient mean $\mu_i(\Delta T_{t_1-t_2})$ relative to DC M_i^{DC} deviations

$$\left|\frac{M_i^{\text{DC}} - \mu_i(\Delta T_{t_1-t_2})}{M_i^{\text{DC}}}\right| = \left|\frac{\text{bias}_i(\Delta T_{t_1-t_2})}{M_i^{\text{DC}}}\right| =: \text{Var}_i(\Delta T_{t_1-t_2}) \tag{5.12}$$

at given time intervals $\Delta T_{t_1-t_2}$ are shown in Table 5.4. These calibration results are limited to the current adjusted capacitance tuning setting and need to be re-calibrated when altering the measurement setup and or the tuning setting. Further, the results verify the opportunity for fast HV division with the novel fast precision HV divider in a tuned frequency compensated setup. The output transmission for all settings can be succeeded with a stability (derived from the transient mean $\mu_i(\Delta T_{t_1-t_2})$ uncertainty) of about 10 ppm, considering $\Delta T_{t_1-t_2} = [8\,\text{ms}, 10\,\text{ms}]$ time slice analysis, up to ~ 5 ppm when exceeding the time slices by 5 ms.

Table 5.4.: $M_i(t)$-calibration of the novel fast precision HV divider using the Kepco Bop 1000m HV power supply. The transient response behaviour $M_i(t)$ is characterized by its relative mean transient $\mu_i(\Delta T_{t_1-t_2})$ deviation to the DC scale factor M_i^{DC} in a certain time interval $\Delta T_{t_1-t_2}$ denoted by $\text{Var}_i(\Delta T_{t_1-t_2})$. The calibrations took place after capacitance tuning of the corresponding scale factor settings as described in the former Subsection 5.4.3.

		M_{94} (17-10-20)	M_{1027} (19-10-20)	M_{1961} (21-10-20)
DC scale factor M_i^{DC} at 800 V		94.3459(4) : 1	1027.721(7) : 1	1961.092(11) : 1
$\mu_i(\Delta T_{t_1-t_2})$	8 to 10 ms	94.3473(10)	1027.697(10)	1961.037(21)
	8 to 15 ms	94.3469(7)	1027.703(7)	1961.059(15)
	10 to 15 ms	94.3467(5)	1027.706(6)	1961.068(14)
$\text{bias}_i(\Delta T_{t_1-t_2})$	8 to 10 ms	−0.0014(14)	0.024(18)	0.053(32)
	8 to 15 ms	−0.0010(11)	0.018(14)	0.031(26)
	10 to 15 ms	−0.0008(10)	0.015(13)	0.022(25)
$\text{Var}_i(\Delta T_{t_1-t_2})$	8 to 10 ms	(15 ± 15) ppm	(23 ± 18) ppm	(27 ± 16) ppm
	8 to 15 ms	(11 ± 12) ppm	(18 ± 14) ppm	(16 ± 13) ppm
	10 to 15 ms	(8 ± 11) ppm	(15 ± 13) ppm	(11 ± 12) ppm

The $M_i(t)$-calibrations conclude relative deviations to the terminating DC value of 8 to 27 ppm (with uncertainties from 11 to 18 ppm). This depends on the response time interval $\Delta T_{t_1-t_2}$ and the goodness of the all-pass tuning which was limited by the tuning precision of the variable air capacitors. In principle, there are ways to further increase the precision to an upper limit. On the one hand, the response time interval could be extended by a few milliseconds. On the other hand, the correction bias along with the corresponding DC scale factor M_i^{DC} could be calibrated with higher accuracy. The latter can be achieved utilizing the main G35 HV divider (see Subsection 2.5.2) in a temperature stabilized environment along with proper calibration equipment.

Chapter 6

Summary & outlook

Over the last decades, numerous breakthroughs were achieved in the field of nuclear and atomic physics within the Standard Model. Still, lots of important predictions remain unverified concerning atomic processes and dynamics including many-body, relativistic and QED effects. Aspiring research opportunities for explorations in this realm are spectroscopy experiments with low-energy highly charged heavy ions which can be stored and collided in dedicated synchrotron and storage rings. The low-energy heavy ion storage ring CRYRING@ESR, as the first component of the future particle accelerator complex FAIR in Darmstadt, aims at a variety of experimental approaches. These comprise high-sensitive spectroscopy with HCI exploiting electron-ion collision events to examine transition energies of resonant DR processes. From that, QED corrections or various nuclear parameters like charge radii and magnetic moments can be derived. Key features of CRYRING@ESR are the capability of fast energy-ramping the stored ions and electron cooling. This is achieved by its implemented electron cooler section which allows sharp energy distributions in a narrow beam profile and hence high-resolution in spectroscopy.

As it turned out during storage ring beam time at ESR in 2011, measuring the ground-state hyperfine transition in lithium-like bismuth as part of the LIBELLE experiment, the accuracy in determining the transition energy in the ions rest frame was limited. This restriction occurred due to the insufficient knowledge of the ion velocity determined by the electron cooler potential difference. Hence, the facility was equipped with a DC precision HV divider setup (G35) constructed at the Institute of Nuclear Physics of the University of Münster in 2019. It features low-ppm accuracy in HV measurements up to 35 kV. Similar uncertainties in experiments with fast changing electron cooler voltages, as in case of DR spectroscopy, where relative electron-ion collision energies are

introduced, ought to be avoided. Therefore, a complementing novel fast precision HV divider has been commissioned with special signal processing characteristics for surge HV transmission. This should enable a frequency independent voltage division and subsequent acquisition of the short-lasting detuning potentials with high accuracy in the order of 10 ppm. Currently, this is out of reach using the pre-existing G35 HV divider setup.

As part of this work, this novel add-on divider has been designed, assembled and tested regarding its requirements for utilization at CRYRING@ESR. It features a low TCR ultra-precision ohmic divider chain along with an additional capacitive chain. The latter seeks to frequency compensate the divider setup by realizing an all-pass transmission behaviour. The divider provides three different scale factor settings ($M_{94} = 94 : 1$, $M_{1027} = 1027 : 1$ and $M_{1961} = 1961 : 1$), switchable by means of an outer control unit. This addresses a proper voltage operation range up to 20 kV in a single measurement tap. Further, it offers capacitance tuning extensions connected to a variable air capacitor section. These complement the capacitance chain for the use of fine-tuning the quality of frequency compensation. The HV input and output connectors are compatible with the G35 connections. Thus, its employment alongside the G35 with the current HV equipment stationed at GSI is possible. To verify the divider demands for fast precision HV division, a calibration method has been developed. This gave insights into the transmission behaviour regarding fast changing HV input division using an in-house Kepco Bop 1000m HV power supply. It was shown, that the short-term reproducibility of the divider transmission fulfills the requirements with an uncertainty range of 4 to 9 ppm. The long-term stability was characterized as 2 to 5 ppm/d, depending on the corresponding scale factor setting. To examine the transient response behaviour, the transient means in different response time slices were considered. Thereby, the relative mean deviations to the DC scale factor, derived from the reproducibility investigations, could be determined as a measure of the quality of frequency compensation. As a result, deviations from (15 ± 15) ppm to (27 ± 16) ppm were intended considering 8 to 10 ms response time. This can be reduced by further increasing the time slices. Hence, 10 to 15 ms intervals lead to deviations of (8 ± 11) ppm for the M_{94}-setting, (15 ± 13) ppm for the M_{1027}-setting and (11 ± 12) ppm for the M_{1961}-setting (with DC uncertainty included). Since the precision of the integrated variable air capacitors appear to be limited to a certain degree, it prevents to elaborate a more precise all-pass tuning. Therefore, the transient response behaviour for the different scale factor settings did not vanish. However, it is possible to calibrate the characteristic correction bias against the DC output.

Future proceedings could include a complementing sub-pF capacitance tuner implementation (as already introduced in Subsection 5.4.3) into the divider circuit in parallel to the C-Tuner 1 device. This would extend the tuning precision of the control unit. Currently, this is limited by the variable air capacitors as intended during work on the divider calibration. Nonetheless, it is not conclusively clarified whether the remaining transient response behaviour is induced by the characteristic transient divider observed during the 10 V pulse transmission tests (see Section 5.3) or is the result of an imprecise tuning. To what degree the time-dependency can be reduced is thereby unknown, but there may be a scope for improvement allowing measurements within 10 ms response time in a broader

range. To enable a more user friendly capacitance tuning in the future, the HV power supply calibration shall be improved. This shall include synchronous acquisition and real-time display of the scale factor time-dependency which results from the acquired input and output signal data. Thereby, time jitter effects must be taken into account which emerge from asynchronous measurement device control.

Furthermore, the novel fast precision HV divider needs to be transferred to the facilities of CRYRING@ESR at GSI in Darmstadt. There it will be installed onto the KANYA aluminium extension profile of the stationed pre-existing HV measurement setup. This will establish a new combined setup as illustrated in Section 4.3. A calibration with the main G35 HV divider before and after each measurement period will be mandatory in order to allow fast changing HV measurements for high-precision DR spectroscopy experiments.

References

[A+12] G. Aad et al. Observation of a new particle in the search for the Standard Model Higgs boson with the ATLAS detector at the LHC. *Physics Letters B*, 716(1):1–29, September 2012.

[A+15] Z. Andelkovic et al. Technical Design Report: Experimental Instrumentation of CRYRING@ESR. 2015.

[Aim20] Aim-TTi LCR400 Precision LCR Bridge Data Sheet. https://docs.rs-online.com/9331/0900766b813d7b26.pdf, 2020. Accessed: 2020-07-15.

[Ana20] Analog Devices, Inc. Website. https://www.analog.com/en/design-center/design-tools-and-calculators/ltspice-simulator.html, 2020. Accessed: 2020-08-12.

[B+08] C. Brandau et al. Isotope Shift in the Dielectronic Recombination of Three-Electron $^{A}Nd^{57+}$. *Physical Review Letters*, 100(7), February 2008.

[B+13] S. Bauer et al. Next generation KATRIN high precision voltage divider for voltages up to 65kV. *Journal of Instrumentation*, 8(10):P10026–P10026, October 2013.

[BK12] C. Brandau and C. Kozhuharov. Storage-Ring Studies of Dielectronic Recombination as a Tool for Precision Spectroscopy. In *Atomic Processes in Basic and Applied Physics*, pages 283–306. Springer Berlin Heidelberg, 2012.

[BV16] Rosario Bartiromo and Mario De Vincenzi. *Electrical Measurements in the Laboratory Practice*. Springer International Publishing, 2016.

[Cad20a] Caddock MS260 Power Film Resistors Data Sheet. http://www.caddock.com/Online_catalog/Mrktg_Lit/TypeMS.pdf, 2020. Accessed: 2020-06-30.

[Cad20b] Caddock MX450 Power Film Resistors Data Sheet. http://www.caddock.com/Online_catalog/Mrktg_Lit/TypeMX.pdf, 2020. Accessed: 2020-06-30.

[Cad20c] Caddock Type USF Ultra-Stable Low TC Film Resistors 200 Series and 300 Series Data Sheet. https://www.mouser.de/datasheet/2/62/TypeUSF-3658.pdf, 2020. Accessed: 2020-07-13.

[D+94] H. Danared et al. Electron Cooling with an Ultracold Electron Beam. *Physical Review Letters*, 72(24):3775–3778, June 1994.

[D+11] H. Danared et al. LSR Low-Energy Storage Ring. 2011.

[Dan93] H. Danared. Fast electron cooling with a magnetically expanded electron beam. *Nuclear Instruments and Methods in Physics Research Section A: Accelerators, Spectrometers, Detectors and Associated Equipment*, 335(3):397–401, November 1993.

[Dir17] T. Dirkes. Design einer Frequenzkompensation des 35kV-Präzisionshochspannungsteilers für den CRYRING@ESR an der GSI/FAIR. Bachelor's thesis, 2017.

[Ein05] A. Einstein. Zur Elektrodynamik bewegter Körper. *Annalen der Physik*, 322(10):891–921, 1905.

[Flu20a] Fluke 732A Reference Source Data Sheet. https://accusrc.com/uploads/datasheets/7181_732A.pdf, 2020. Accessed: 2020-06-30.

[Flu20b] Fluke 752A Reference Divider Data Sheet. http://download.flukecal.com/pub/literature/752A____imeng0100.pdf, 2020. Accessed: 2020-07-02.

[Gei20] W. Geithner. Cut through a 3D model of CRYRING@ESR with Cave. https://www.gsi.de/work/forschung/appamml/atomphysik/anlagen_und_experimente/cryringesr.htm, 2020. Accessed: 2020-06-30.

[GMC20] METRISO 5000 A/AK Data Sheet. https://www.gossenmetrawatt.com/resources/zz_tam/metriso-5000a/ba_d.pdf, 2020. Accessed: 2020-08-25.

[H+19] C. Hahn et al. A scintillator-based particle detector for CRYRING@ESR. *X-Ray Spectrometry*, 49(2):338–341, September 2019.

[Hei20] Heinzinger High Voltage Plugs HVS Data Sheet. https://www.heinzinger.de/fileadmin/user_upload/Datenblaetter/Katalogseiten/EN/High-voltage-plugs-HVS_HVB-heinzinger.pdf, 2020. Accessed: 2020-07-02.

[Kep11] Operator's Manual - High Voltage Bipolar Power Supply. https://www.kepcopower.com/support/2281733-b.pdf, 2011. Accessed: 2020-09-10.

[Kep20] Kepco BOP 1000M Bipolar Operational Power Supply / Amplifier 1000V 40mA 40W Product Page. http://www.svtechparts.com/index.php/kepco-bop-1000m-bipolar-operational-power-supply-amplifier-1000v-40ma-40w.html, 2020. Accessed: 2020-11-02.

[Key20a] Keysight 3458A Data Sheet. https://www.keysight.com/de/de/assets/7018-06796/data-sheets/5965-4971.pdf, 2020. Accessed: 2020-06-30.

[Key20b] Keysight InfiniiVision 2000 X-Series Data Sheet. https://www.keysight.com/de/de/assets/7018-02733/data-sheets/5990-6618.pdf, 2020. Accessed: 2020-09-29.

[Key20c] Keysight Truevolt Series Digital Multimeters Data Sheet. https://literature.cdn.keysight.com/litweb/pdf/34460-90901.pdf, 2020. Accessed: 2020-09-15.

[L+08] M. Lestinsky et al. Screened Radiative Corrections from Hyperfine-Split Dielectronic Resonances in Lithiumlike Scandium. *Physical Review Letters*, 100(3), January 2008.

[L+14] M. Lochmann et al. Observation of the hyperfine transition in lithium-like bismuth $^{209}Bi^{80+}$: Towards a test of QED in strong magnetic fields. *Physical Review A*, 90(3), September 2014.

[Lem20] Coaxial, triaxial, multi & mixed connectors - short form catalogue. https://www.lemo.com/catalog/ROW/UK_English/Coax_triax_mixed_en.pdf, 2020. Accessed: 2020-09-17.

[Les07] M. Lestinsky. High-Resolution Electron Collision Spectroscopy with Multicharged Ions in Merged Beams. PhD thesis, 2007.

[Mat20] Matthieu Dartiailh, Hernan Grecco. PyVISA, Github repository. https://github.com/pyvisa, 2020. Accessed: 2020-09-24.

[Mer20] Merged-beams collision spectroscopy at the CRYRING@ESR cooler. https://www.gsi.de/work/forschung/appamml/atomphysik/sparc/arbeitsgruppen/electron_targets_cooler/merged_beams_collisions_at_the_cryringesr_cooler.htm, 2020. Accessed: 2020-06-30.

[Mic20] Michael Hayes. Lcapy, Github repository. https://github.com/mph-/lcapy, 2020. Accessed: 2020-08-12.

[Mü08] A. Müler. Electron–ion collisions: Fundamental processes in the focus of applied research. In *Advances In Atomic, Molecular, and Optical Physics*, pages 293–417. Elsevier, 2008.

[Ott16] G. Otto. First turn in FAIR's first ring: Big step forward in installation of CRYRING ion storage ring. https://fair-center.eu/for-users/experiments/appa/newsview-appa/article/first-turn-in-fairs-first-ring-big-step-forward-in-installation-of-cryring-ion-storage-ring.html, December 2016. Accessed: 2020-06-30.

[P+10] R. Pohl et al. The size of the proton. *Nature*, 466(7303):213–216, July 2010.

[Pho20] Feed-through terminal block - UT 2,5 RD - 3045062 Data Sheet. https://asset.conrad.com/media10/add/160267/c1/-/en/000658691DS02/datenblatt-658691-phoenix-contact-ut-25-rd-3045062-durchgangsreihenklemme-polzahl-2-014-mm-4-mm-rot-1-st.pdf, 2020. Accessed: 2020-09-22.

[R+19] O. Rest et al. A novel ppm-precise absolute calibration method for precision high-voltage dividers. *Metrologia*, 56(4):045007, July 2019.

[Rai20] Raise3D Pro2 Dual Extruder 3D Printer Product Page. https://www.raise3d.com/pro2/, 2020. Accessed: 2020-11-02.

[Res19] O. Rest. Precision high voltage at the KATRIN experiment and new methods for an absolute calibration at ppm-level for high-voltage dividers. PhD thesis, 2019.

[Rit20] Kompakt-Schaltschränke AE – AE 1037.500 Data Sheet. http://www.rittal.com/de-de/ebooks/generated-pdf/de-de/1037500/1037500.pdf?json=%7B%22successURL%22%3A+%22ebooks%2Fgenerated-pdf%2Fde-de%2F1037500%2F1037500.pdf%22%7D, 2020. Accessed: 2020-08-17.

[Roß15] J. Roßbach. Electron Cooling at GSI and FAIR - Status and Latest Activities, COOL Workshop Talk. https://accelconf.web.cern.ch/cool2015/talks/wexaud04_talk.pdf, 2015. Accessed: 2020-06-30.

[Rot19] D. Roth. Frequency compensation for fast voltage measurements with the G35 precision HV divider at CRYRING@ESR. Master's thesis, 2019.

[Rut11] E. Rutherford. LXXIX. The scattering of α and β particles by matter and the structure of the atom. *The London, Edinburgh and Dublin Philosophical Magazine and Journal of Science*, 21(125):669–688, May 1911.

[S+05] R. Schuch et al. Dielectronic Resonance Method for Measuring Isotope Shifts. *Physical Review Letters*, 95(18), October 2005.

[Spr20] Sprague-Coodman Electronics SGNMA3T10004 CAP TRIMMER 1-10PF 1000V TH Data Sheet. https://media.digikey.com/pdf/Data%20Sheets/Sprague-Goodman%20PDFs/SGNMA3T10004_Dwg.pdf, 2020. Accessed: 2020-11-7.

[Sá14] Zátonyi Sándor. Principle of the rotary variable capacitor. *Wikimedia Commons*. https://commons.wikimedia.org/w/index.php?curid=30492395, 2014. Accessed: 2020-09-09.

[T+02] M. Tokman et al. Dielectronic recombination resonances in F^{6+}. *Physical Review A*, 66(1), July 2002.

[Tek20a] Tektronix AFG3000 Series Datasheet. https://www.tek.com/signal-generator/afg3000-manual/afg3000-series-2, 2020. Accessed: 2020-09-29.

[Tek20b] Tektronix AFG3000 Series Programmer Manual. https://mmrc.caltech.edu/Tektronics/AFG3021B/AFG3021B%20Programmer%20Manual.pdf, 2020. Accessed: 2020-09-29.

[Tho97] J. J. Thomson. XL. Cathode Rays. *The London, Edinburgh and Dublin Philosophical Magazine and Journal of Science*, 44(269):293–316, October 1897.

[TTW09] R. Marx T. Thümmler and C. Weinheimer. Precision high voltage divider for the KATRIN experiment. *New Journal of Physics*, 11(10):103007, October 2009.

[Vis20a] Vishay MKT1816 Metallized Polyester Film Capacitors Data Sheet. `https://pdf.datasheetcatalog.com/datasheet/vishay/mkt1816.pdf`, 2020. Accessed: 2020-06-30.

[Vis20b] Vishay VHA518-11 Data Sheet. `http://www.vishaypg.com/docs/63006/hmetlab.pdf`, 2020. Accessed: 2020-06-30.

[Win20] D. Winzen. Laser spectroscopy of lithium-like carbon with a novel XUV detection system at the ESR and construction of a precision high voltage divider for the CRYRING@ESR electron cooler. PhD thesis, 2020.

List of Figures

List of Tables

Appendix A

Simulation & measurement graphics

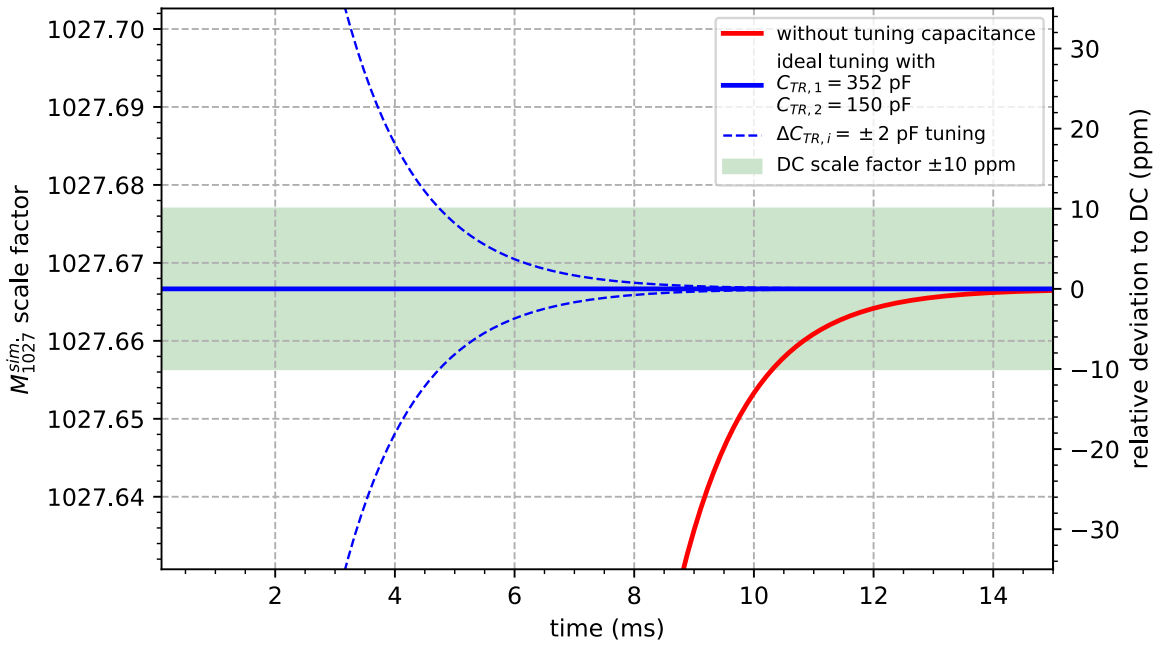

Figure A.1.: Scale factor M_{1027} time domain simulation similar to the M_{94} time domain simulation illustrated in Figure 4.5 with no tuning capacitance (red) and with ideal step-wise tuning of $C_{\mathrm{TR},1} = 352\,\mathrm{pF}$ and $C_{\mathrm{TR},2} = 150\,\mathrm{pF}$ (blue).

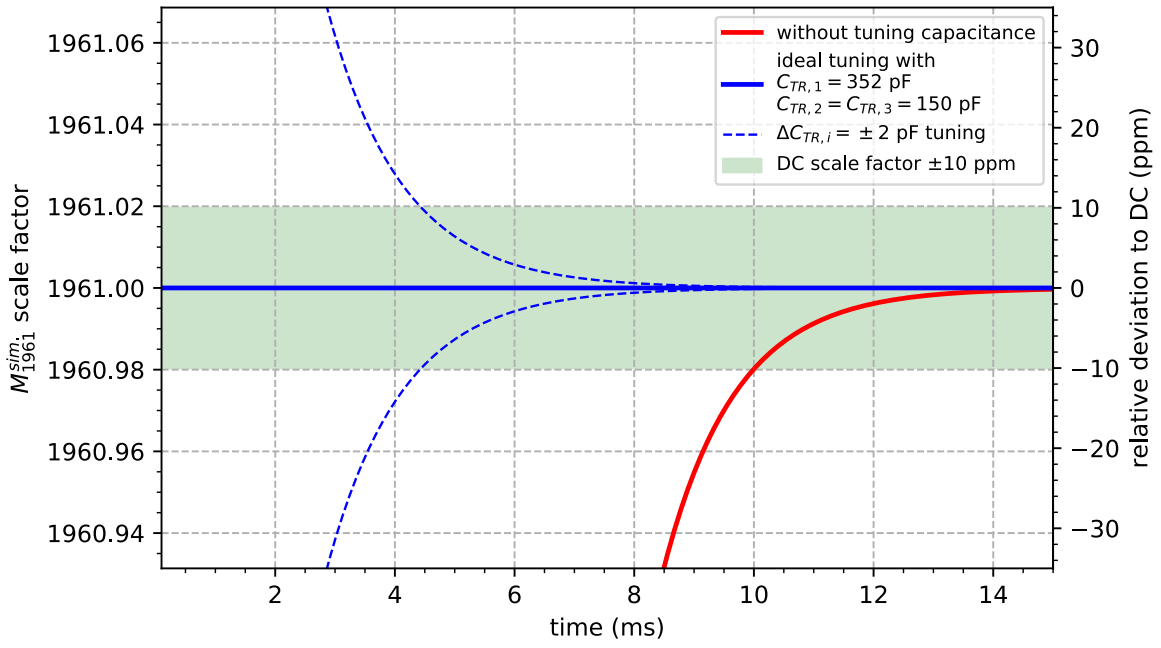

Figure A.2.: Scale factor M_{1961} time domain simulation similar to the M_{94} time domain simulation illustrated in Figure 4.5 with no tuning capacitance (red) and with ideal step-wise tuning of $C_{\mathrm{TR},1} = 352\,\mathrm{pF}$ and $C_{\mathrm{TR},2} = C_{\mathrm{TR},3} = 150\,\mathrm{pF}$ (blue).

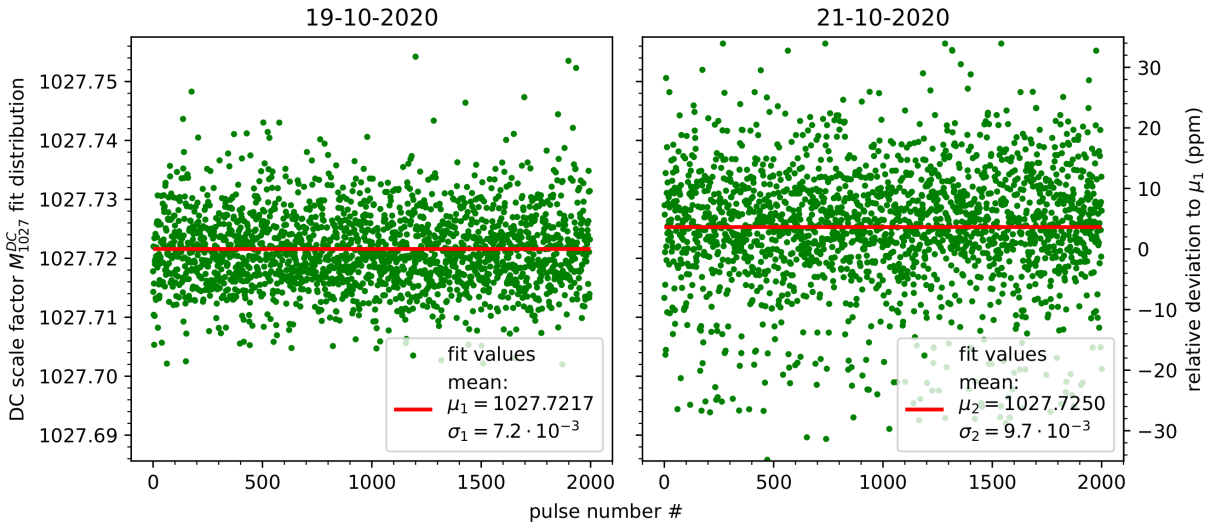

Figure A.3.: M_{1027}^{DC} fit distribution of 2000 analyzed single transient responses along with its mean $\mu_{1,2}$ and standard deviation $\sigma_{1,2}$ based on measurements performed on October 19, 2020 and October 21, 2020 with 48 h delay to investigate the long-term stability of the M_{1027}-scale factor setting.

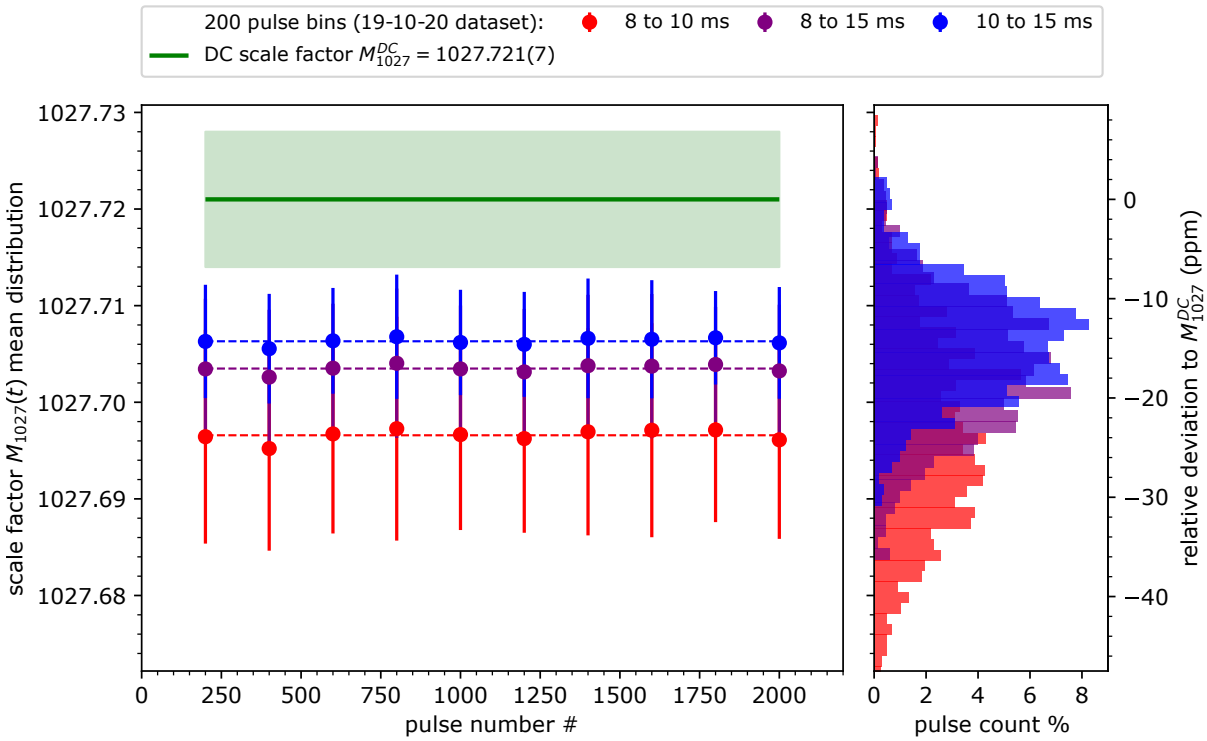

Figure A.4.: 200 pulse binned μ_{1027}-distribution for the 8 to 10 ms (red), 8 to 15 ms (purple) and 10 to 15 ms (blue) response time intervals $\Delta T_{t_1-t_2}$ compared to the DC scale factor M_{1027}^{DC} (green). The latter was determined from the fit distribution illustrated in Figure A.3 (19-10-20).

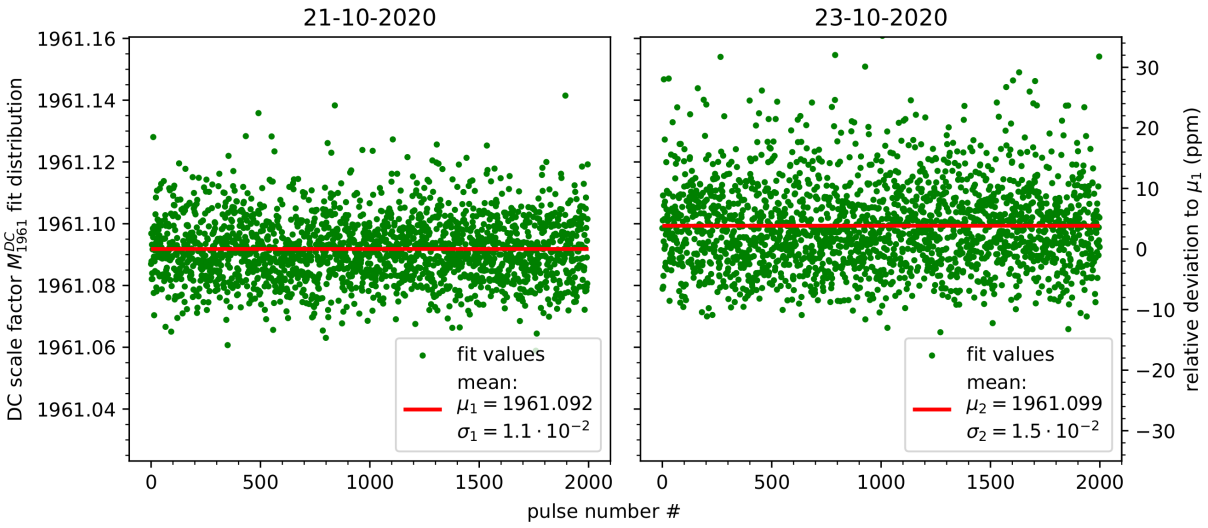

Figure A.5.: M_{1961}^{DC} fit distribution of 2000 analyzed single transient responses along with its mean $\mu_{1,2}$ and standard deviation $\sigma_{1,2}$ based on measurements performed on October 21, 2020 and October 23, 2020 with 48 h delay to investigate the long-term stability of the M_{1961}-scale factor setting.

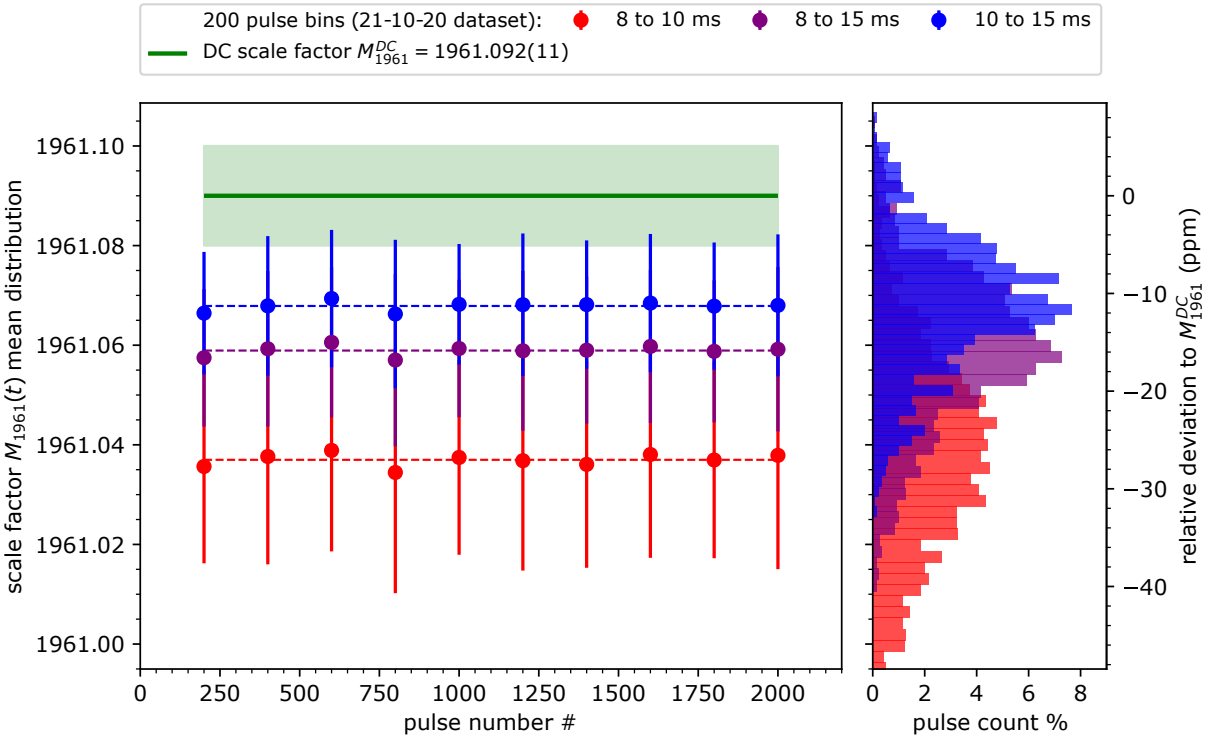

Figure A.6.: 200 pulse binned μ_{1961}-distribution for the 8 to 10 ms (red), 8 to 15 ms (purple) and 10 to 15 ms (blue) response time intervals $\Delta T_{t_1-t_2}$ compared to the DC scale factor M_{1961}^{DC} (green). The latter was determined from the fit distribution illustrated in Figure A.5 (21-10-20).

Appendix B

Additive parts drawings

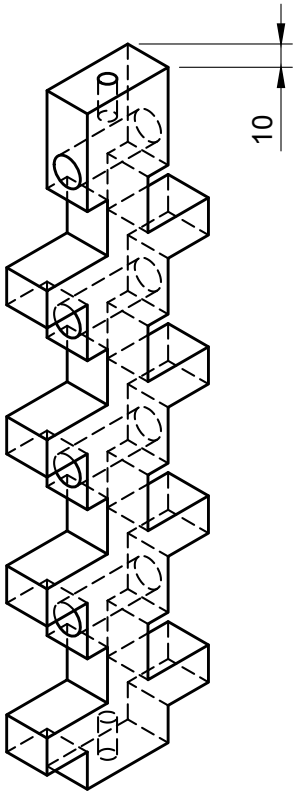

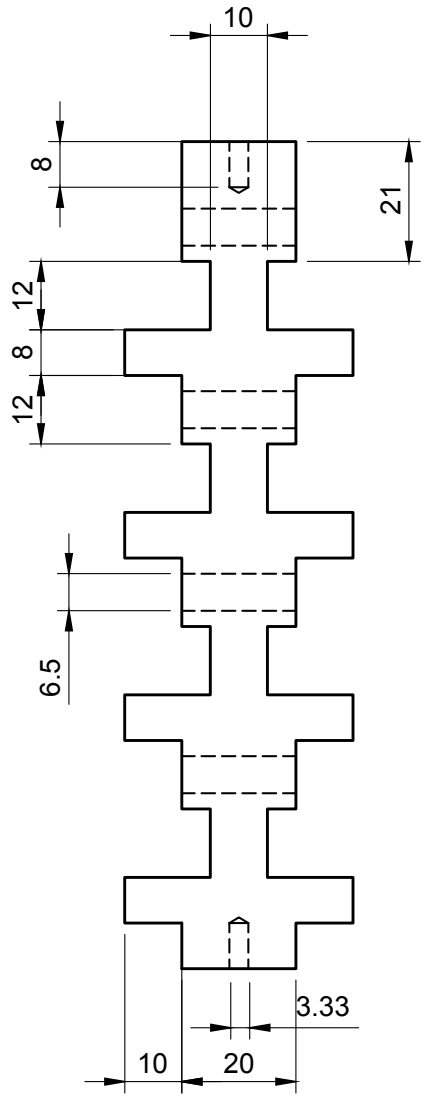

Dept.	Technical reference	Created by Timo Dirkes 04.11.20	Approved by
		Document type	Document status
		Title PLA-Holding 1	DWG No.
			Rev. / Date of issue / Sheet 1/1

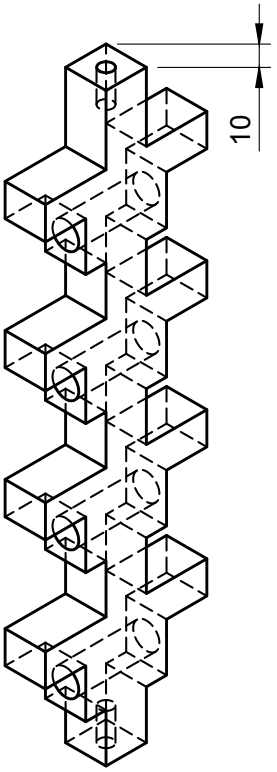

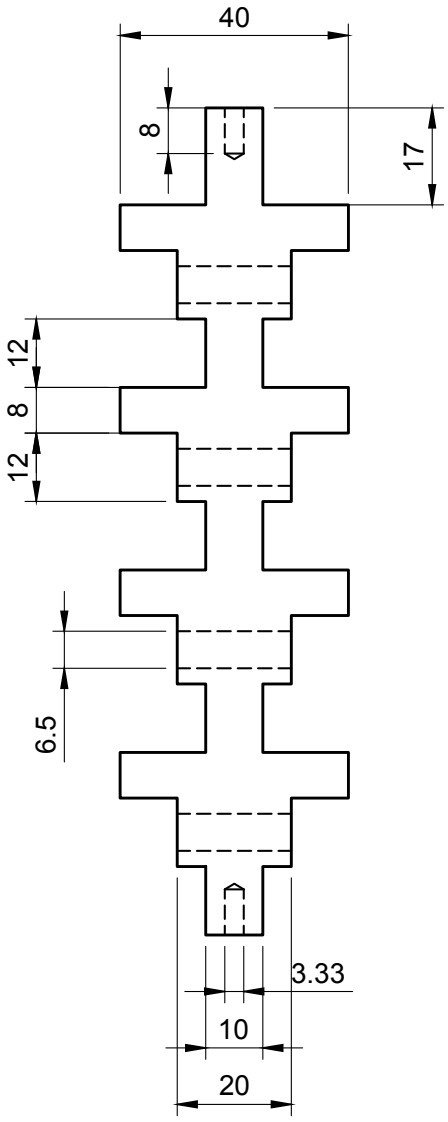

Dept.	Technical reference	Created by Timo Dirkes 04.11.20	Approved by	
		Document type	Document status	
		Title PLA-Holding 2	DWG No.	
			Rev. / Date of issue	Sheet 1/1

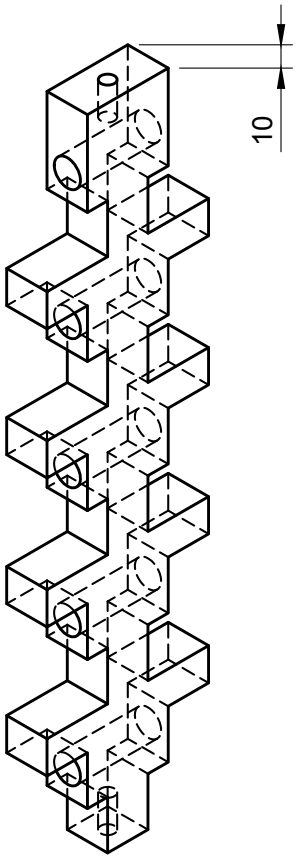

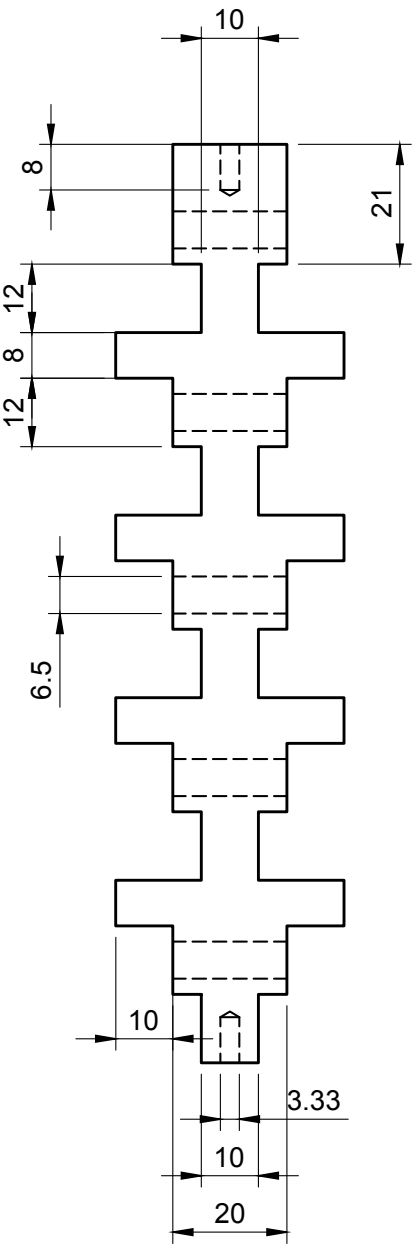

Dept.	Technical reference	Created by Timo Dirkes 04.11.20	Approved by
		Document type	Document status
		Title PLA-Holding 3	DWG No.
			Rev. / Date of issue / Sheet 1/1

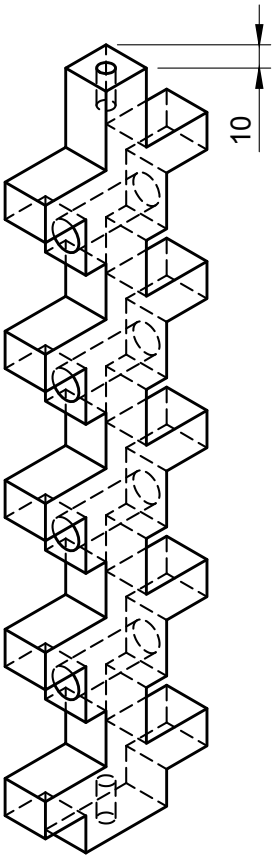

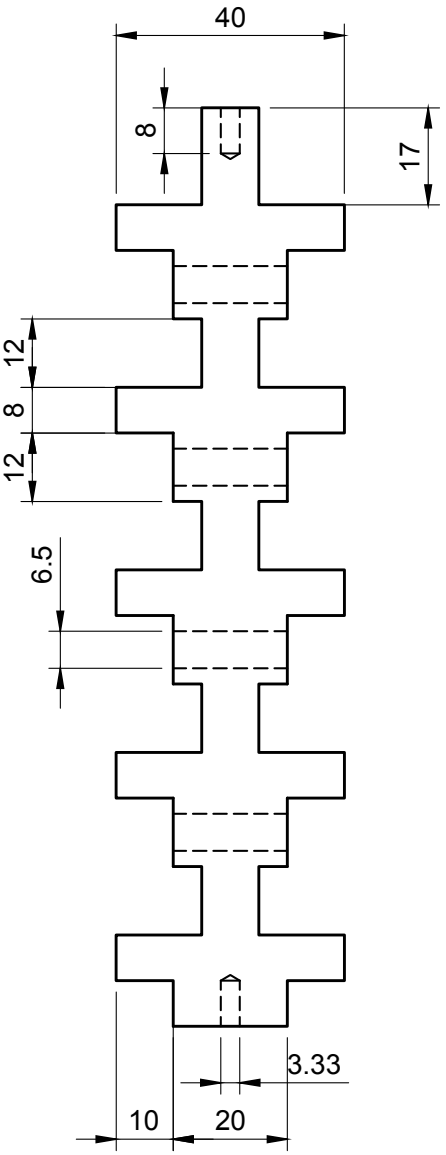

Dept.	Technical reference	Created by Timo Dirkes 04.11.20	Approved by
		Document type	Document status
		Title PLA-Holding 4	DWG No.
			Rev. / Date of issue / Sheet 1/1

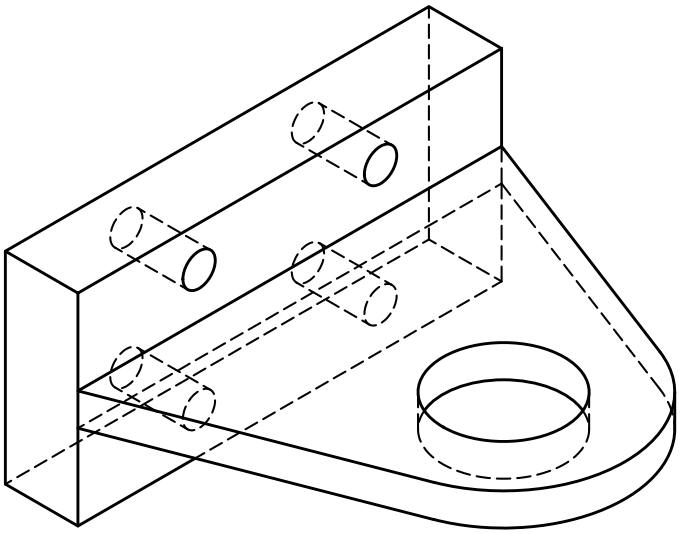

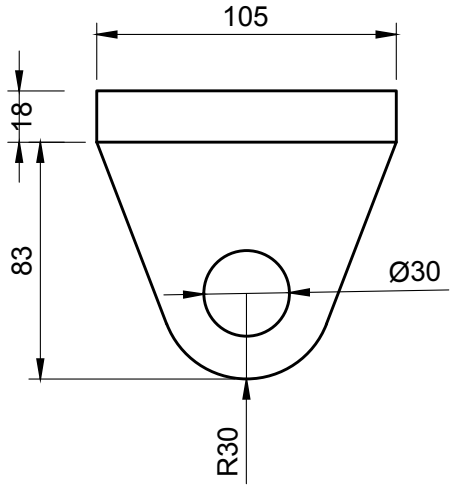

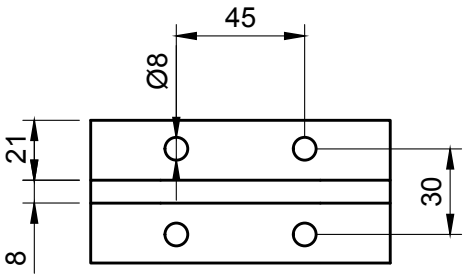

Dept.	Technical reference	Created by Timo Dirkes 04.11.20	Approved by
		Document type	Document status
		Title PLA-Fixation 1	DWG No.
			Rev. / Date of issue / Sheet 1/1

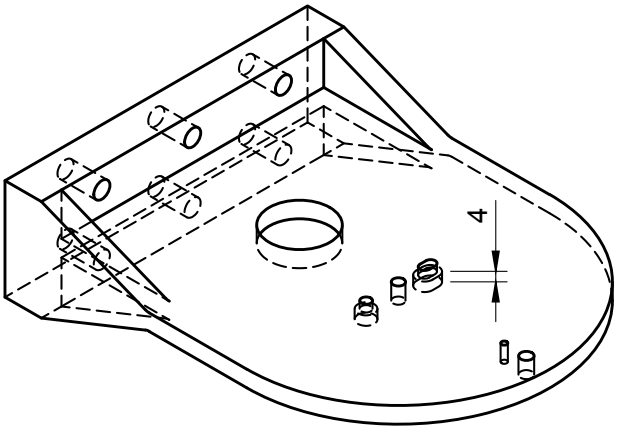

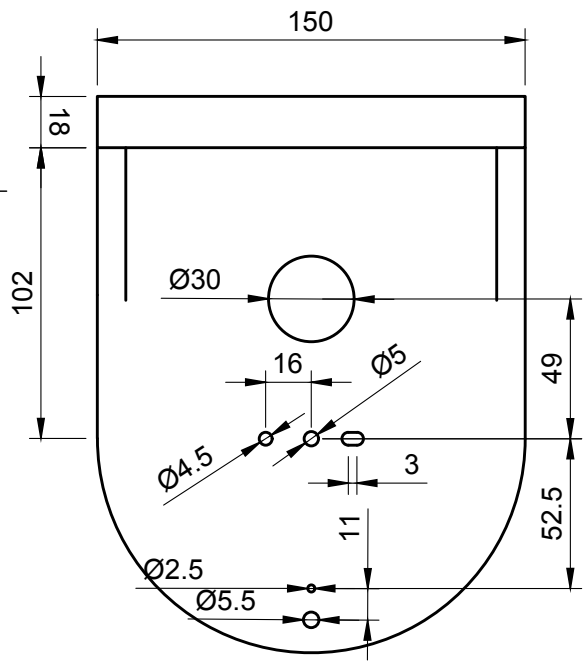

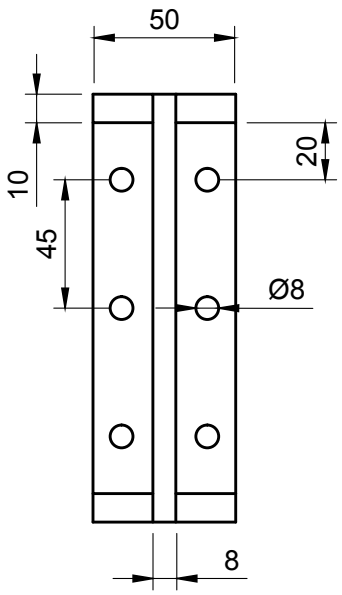

Dept.	Technical reference	Created by Timo Dirkes 04.11.20	Approved by	
		Document type	Document status	
		Title PLA-Fixation 2	DWG No.	
			Rev. / Date of issue	Sheet 1/1

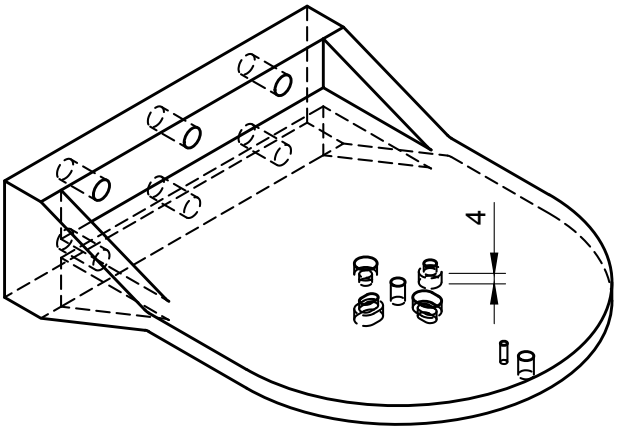

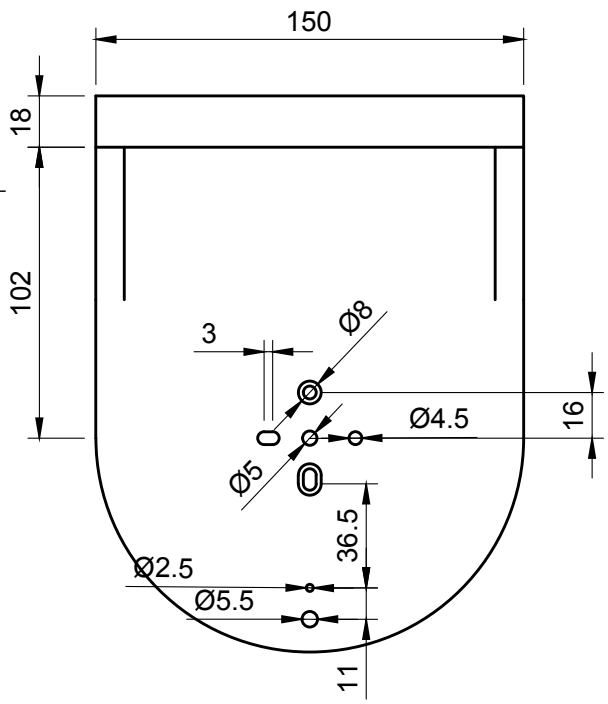

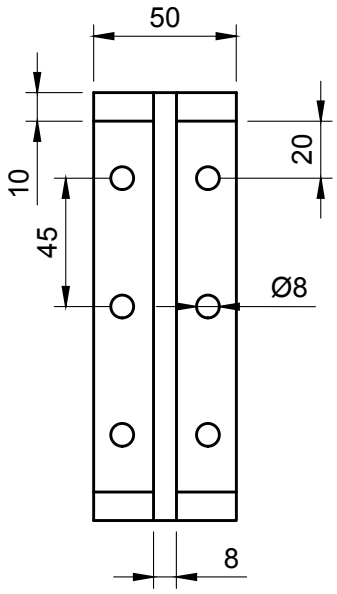

Dept.	Technical reference	Created by Timo Dirkes 04.11.20	Approved by
		Document type	Document status
		Title PLA-Fixation 3	DWG No.
			Rev. / Date of issue / Sheet 1/1

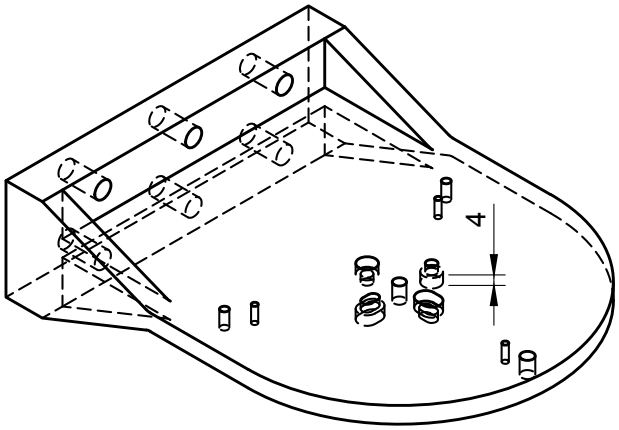

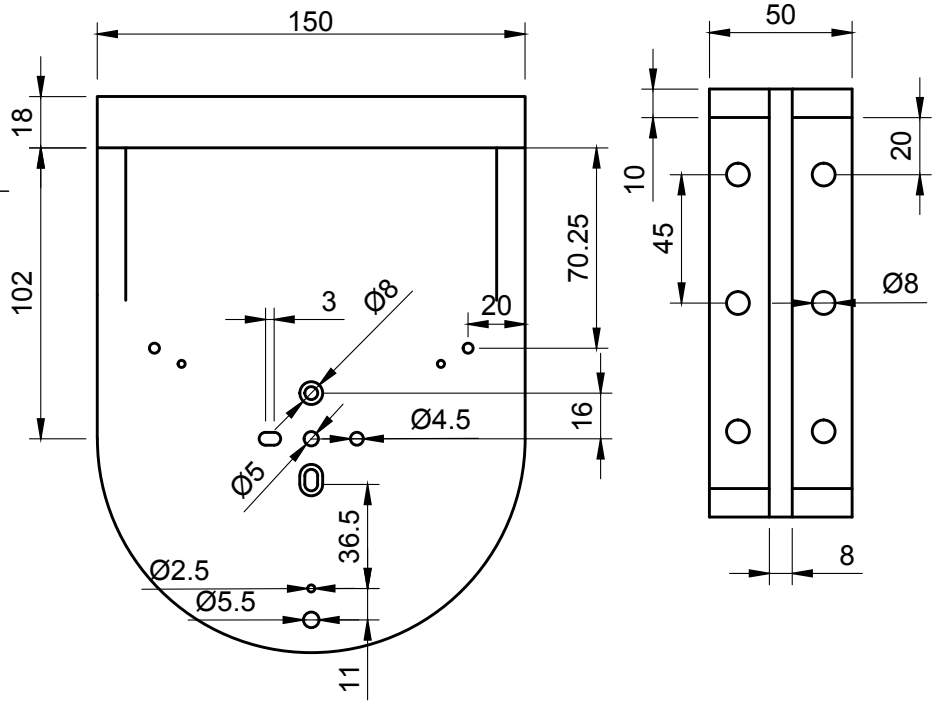

Dept.	Technical reference	Created by	Approved by
		Timo Dirkes 04.11.20	
		Document type	Document status
		Title: PLA-Fixation 4	DWG No.
			Rev. / Date of issue / Sheet: 1/1

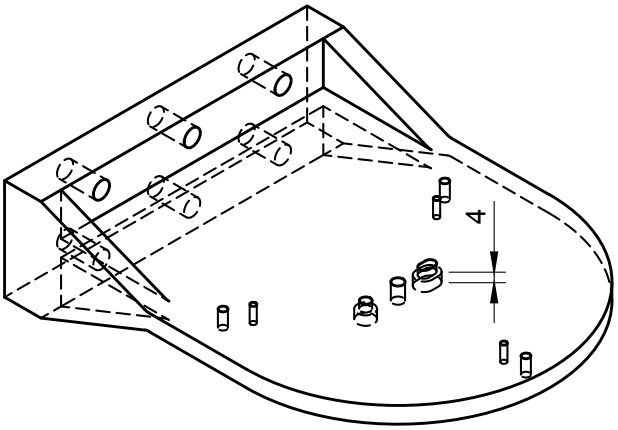

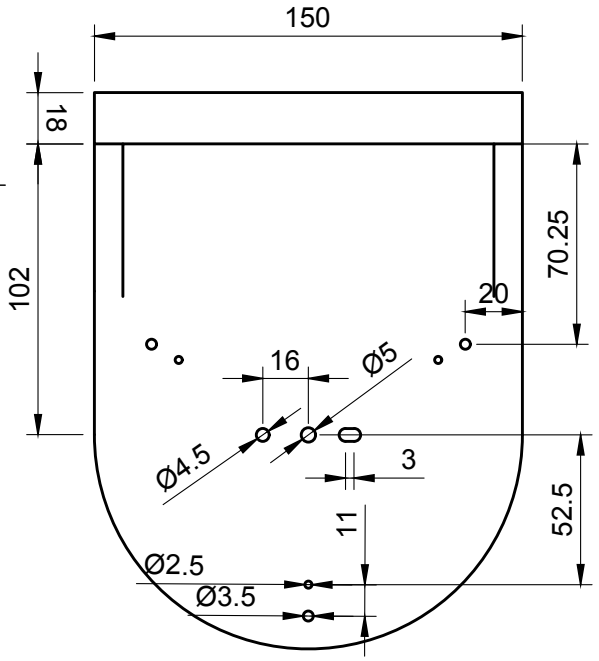

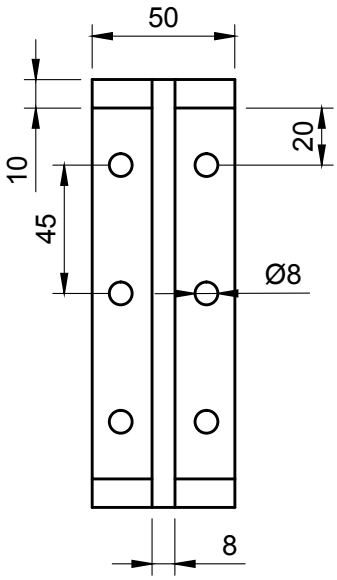

Dept.	Technical reference	Created by Timo Dirkes 04.11.20	Approved by	
		Document type	Document status	
		Title PLA-Fixation 5	DWG No.	
			Rev. / Date of issue	Sheet 1/1